MASTER'S THESIS IN PHYSICAL
OCEANOGRAPHY

Idealized Modeling of the North Icelandic Jet

Thorbjørn Østenby Moe

UNIVERSITY OF BERGEN
GEOPHYSICAL INSTITUTE

June 1, 2023

Abstract

The North Icelandic Jet (NIJ) is a crucial component of the lower limb of the Atlantic Meridional Overturning Circulation, supplying one-third to one-half of the overflow water transport through Denmark Strait, including the densest portion. However, the mechanisms associated with its emergence, evolution, and structure are not fully known. With an idealized model of the north Icelandic slope developed using ROMS, I study the fundamental dynamics of the NIJ, including the mechanisms governing its formation. I designed the model as a channel along the slope north of Iceland, initially with no external forcing. Several specific boundary conditions were then iteratively applied to the western boundary, intended to simulate combinations of Atlantic inflow and dense outflow through Denmark Strait. Additionally, configurations with differing levels of increased realism regarding both hydrography and changes in slope steepness in the along-channel direction were simulated. My simulations are consistent with the cross-sectional structure observed north of Iceland, including a mid-depth intensified NIJ associated with diverging isopycnals away from the slope. I have found that the simulated NIJ is the strongest and most consistent when prescribed to the bottom and adjacent to a strong Atlantic inflow, indicating the importance of the flows through Denmark Strait for the upstream structure. The current's stability and strength are considerably reduced with a steeper north Icelandic slope, indicating that slope steepness heavily influences the NIJ. Along-channel changes in slope steepness show an uncoupling of the strength and structure of the simulated NIJ, as the structure is largely determined by the steepness, while the strength depends more on upstream modifications. Along- and across-channel changes in the stratification are found to have a smaller impact on the general structure and circulation than the slope steepness. Higher EKE associated with the steeper slope in my simulations corroborates that the northeastern Icelandic slope is a crucial region for the emergence of the NIJ.

Acknowledgements

Contents

Chapter 1

Introduction

A key component of the Meridional Overturning Circulation (MOC) is high-latitude buoyancy loss, as the relatively warm ocean loses heat to the colder atmosphere. The buoyancy loss in the polar regions of both hemispheres contributes to separate cells of the MOC, which redistributes vast amounts of heat, freshwater, and carbon throughout the ocean (Kuhlbrodt et al., 2007; Buckley & Marshall, 2016). The southern hemisphere's component is the densest (lower) MOC cell and occupies the bottom of the world's oceans. The upper MOC cell, the Atlantic MOC (AMOC), is mainly confined to the Atlantic Ocean (Buckley & Marshall, 2016), as it primarily receives contributions from the North Atlantic and Nordic Seas (Chafik & Rossby, 2019). Both the upper and lower MOC cells are closed by diapycnal mixing (Munk & Wunsch, 1998; Kuhlbrodt et al., 2007) and upwelling driven by strong westerly winds in the southern ocean, which are considered the driving forces of the circulation (Kuhlbrodt et al., 2007; Marshall & Speer, 2012).

The AMOC consists of a poleward surface transport of warm and saline Atlantic Water (AW) and an equatorward intermediate and deep transport of newly transformed cold and dense water masses. The future state of the AMOC is a greatly contested topic concerning the warming, sea ice retreat, and changes in freshwater fluxes associated with climate change (Cheng et al., 2013; Drange et al., 2013; Fu et al., 2020; Elvidge et al., 2021; Årthun et al., 2023). The AMOC has been projected to undergo a strong decline by the end of the century in several climate models (Gregory et al., 2005; Cheng et al., 2013; Buckley & Marshall, 2016). However, such models often struggle to accurately resolve important small-scale mechanisms in the Arctic and Subarctic (Drange et al., 2013; Rosenblum & Eisenman, 2017), especially those near the marginal ice zone (Elvidge et al., 2021). Conversely, observations generally indicate a relatively stable AMOC, although these time series might not fully resolve multidecadal, or even centennial, variability of the AMOC (Fu et al., 2020). In contrast to the projected decline of the AMOC as a whole (Gregory et al., 2005), the overturning circulation of the Nordic Seas is projected to strengthen, which could stabilize the AMOC (Årthun et al., 2023)

The Nordic Seas (Figure 1.1), separated from the North Atlantic by the Greenland-

Scotland Ridge, is a region of great importance for the production of dense water masses which supply the lower limb of the AMOC (Chafik & Rossby, 2019). Warm and saline AW entering the Nordic Seas from the North Atlantic (Red arrows in Figure 1.1) are transformed through air-sea heat loss during the early part of its circumnavigation of the Nordic Seas and the Arctic Ocean (Atlantic-origin water, Mauritzen, 1996). Additional dense water masses are formed through open-ocean convection in the interior of the Nordic Seas (Arctic-origin water, Swift & Aagaard, 1981; Våge et al., 2022). Both of these relatively dense water masses are then transported equatorward out of the Nordic Seas over the Greenland-Scotland Ridge (light blue arrows in Figure 1.1), primarily through Denmark Strait and the Faroe Bank Channel (Figure 1.1).
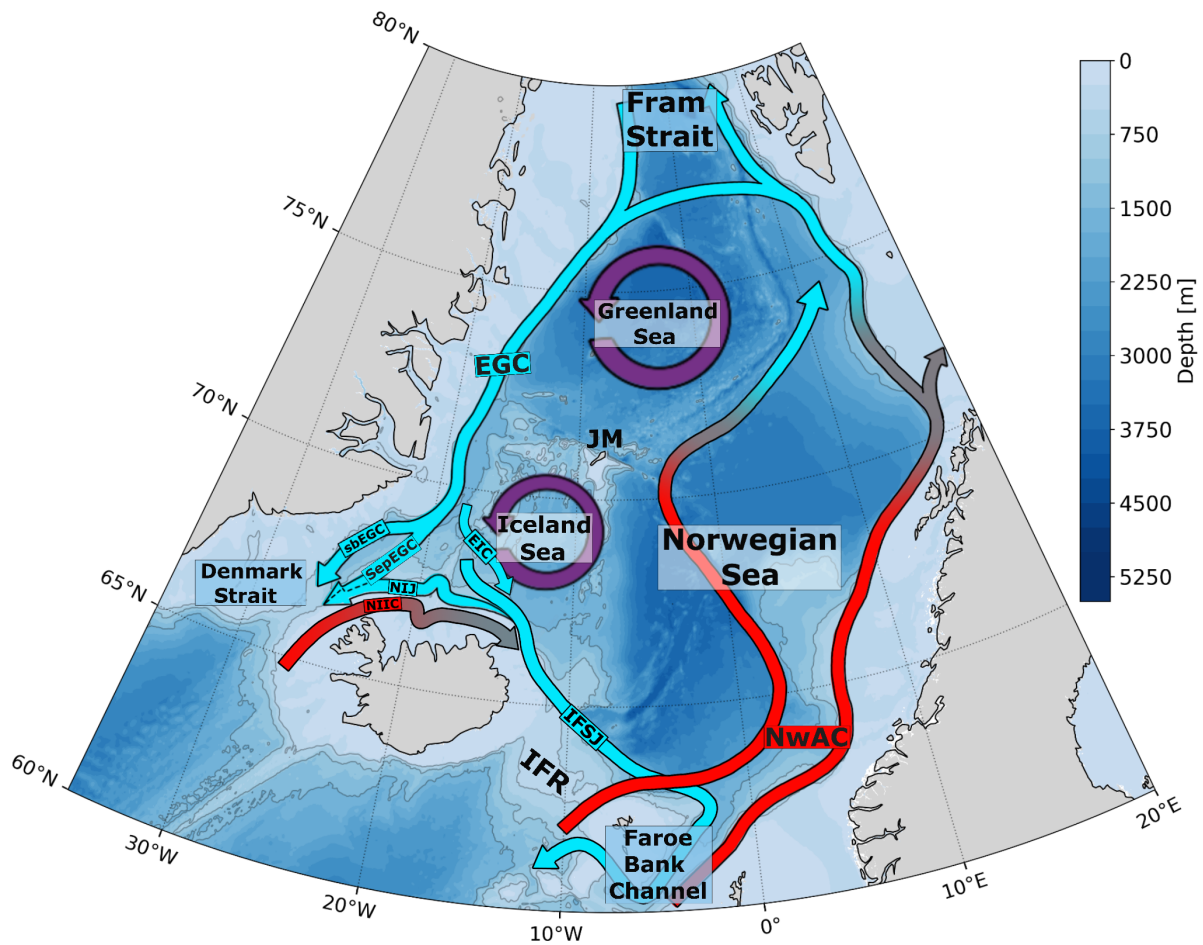
Figure 1.1: Map showing important features and general circulation in the Nordic Seas. Warm currents are colored red and cold currents are colored blue. Water mass transformation is indicated by the red to blue gradients (air-sea heat loss) and purple circles (open-ocean convection). Acronyms are as follows: Jan Mayen (JM), East Greenland Current (EGC), shelfbreak EGC (sbEGC), separated EGC (sepEGC), North Icelandic Jet (NIJ), North Icelandic Irminger Current (NIIC), East Iceland Current (EIC), Iceland Faroe Slope Jet (IFSJ), Iceland-Faroe Ridge (IFR), and Norwegian Atlantic Current (NwAC). The colored shading is bathymetry from ETOPO1 (Amante & Eakins, 2009).

Denmark Strait plays an important role in the poleward and equatorward transport of water masses, as roughly half of the equatorward transport of dense water exists in the Nordic Seas through the strait (Østerhus et al., 2019). AW is transported northward

through Denmark Strait by the North Icelandic Irminger Current (NIIC), Polar Surface Water (PSW) and Atlantic-origin water are transported southward primarily by the East Greenland Current (EGC), while Arctic-origin water is mainly transported southward by the North Icelandic Jet (NIJ, Figure 1.1, Våge et al., 2013). The Arctic-origin water masses transported by the NIJ constitute the densest component of the southward flowing water (Våge et al., 2011). The NIJ is thus an important component of the Nordic Seas' contribution to the lower limb of the AMOC (Semper et al., 2019a).

The NIJ emerges on the northeastern Icelandic slope, before flowing westward along the north Icelandic slope until it reaches Denmark Strait (Våge et al., 2011; Semper et al., 2019a). Along its pathway, isopycnals are tilted up toward the Icelandic slope, which allows the NIJ to transport dense water masses over the Denmark Strait sill of 650 m, as nearly the entire volume transport of the NIJ is situated above this depth (Våge et al., 2011; Semper et al., 2019a). The volume transport of the NIJ increases steadily from its emergence and toward Denmark Strait, reaching a maximum volume transport of roughly 1.8 Sv (1 Sv $\equiv 10^6$ m^{3}s^{-1}) upstream of the strait (Semper et al., 2019a). Although increasing in terms of transport, the properties of the water masses within the NIJ are not considerably modified on its pathway along the north Icelandic slope, as the current is continuously supplied from the north by comparably dense water masses (Semper et al., 2019a).

the NIJ's features, such as the vertical structure, transport, variability, water masses, and interactions with regional circulation, are well documented (Jónsson & Valdimarsson, 2004; Våge et al., 2011; Pickart et al., 2017; Semper et al., 2019a). However, the mechanisms governing its emergence are not fully understood, and the upstream pathways of the water masses in the current remain to be thoroughly characterized. A hypothesized mechanism for the emergence of the NIJ is built on the apparent interconnectedness between the NIJ and NIIC (Pickart et al., 2017) and enhanced eddy kinetic energy (EKE) near the northeastern Icelandic slope (Våge et al., 2011; Semper et al., 2022). The details of the hypothesized mechanism are not completely defined, but, instabilities associated with the NIIC on the northeastern Icelandic Slope are thought to be a part of a complex compensation between the NIIC and the Icelandic Sea which results in the emergence of the NIJ (Våge et al., 2011; Pickart et al., 2017; Semper et al., 2019a, 2022).

In this thesis, I aim to study the NIJ with a simple, idealized model of the slope north of Iceland. The model intentionally has no surface forcing, no tides, no seasonal variability, and a smooth slope, to best study the fundamental aspects of the NIJ. By withdrawing dense water through the western boundary, meant to simulate the overflow through Denmark Strait, I aim to simulate an idealized version of the NIJ. Next, by iteratively adding idealized components, meant to simulate various features associated with the north Icelandic slope, I seek to study the sensitivity of the simulated current and assess the importance of these components for the vertical structure and pathway of the current. The primary aim of the study is to elucidate the mechanisms associated with the NIJ's emergence. The research questions I aim to answer through these methods are:

1. Can an NIJ-like current be convincingly simulated simply by withdrawing dense water at the western boundary?

2. How is the NIJ impacted by changes in the steepness of the north Icelandic slope?

3. How is the NIJ impacted by the stratification near the north Icelandic slope?

4. Is the emergence of the NIJ associated with enhanced EKE attributed to the steeper part of the Icelandic Slope?

The following chapter will in greater detail go through the general circulation of the Nordic Seas and, specifically, the characteristics, dynamics, and mechanisms associated with the NIJ. Then, elementary theory needed for the study and an overview of essential parameters in numerical ocean models will be presented in Chapter 2. Chapter 3 will detail the components of the idealized model setup used in the study and describe the methods used in the analysis. Chapters 4 and 5 will present and discuss the study results, respectively. Lastly, a summary and outlook will be given in Chapter 5, Section 5.3.

1.1 Background

The circulation and water masses of the Nordic Seas

A large part of the circulation in the Nordic Seas is influenced by geography, especially regarding the pathways in and out of the sea. The Nordic Seas consist of the Norwegian, Greenland, and Iceland Seas (Figure 1.1). The Norwegian Sea contains two basins, the Norwegian Basin in the south and the Lofoten Basin in the north. The Jan Mayen Ridge and the Mohn Ridge separate the Norwegian Sea from the Iceland and Greenland Seas, respectively. The West Jan Mayen Ridge separates the Greenland and Iceland Seas. The Nordic Seas are connected to the North Atlantic through various gaps in the Greenland-Scotland Ridge. The deeper passages include Denmark Strait (with a sill depth of approximately 650 m) in the west, between Greenland and Iceland, and The Faroe-Shetland Channel in the east, between the Faroe Islands and Shetland. The Faroe-Shetland Channel is connected to the North Atlantic through the Faroe Bank Channel (FBC, ~850 m). Additionally, the Iceland-Faroe Ridge (IFR) between Iceland and Faroe Island is an extensive, yet, relatively shallow, pathway between the North Atlantic and the Nordic Seas. In the north, the Nordic Seas border the Barents Sea, through a wide and shallow gap between mainland Norway and Svalbard, and the Arctic Ocean through Fram Strait (Figure 1.1).

The North Atlantic Current enters the Nordic Seas in the east through the FSC and IFR as the Norwegian Atlantic Current (NwAC), while a smaller branch, the NIIC, enters through Denmark Strait in the west (Figure 1.1). The two NwAC inflows contribute approximately 6.5 Sv of warm and saline AW water, roughly 3.8 ± 0.5 Sv through IFR and 2.7 ± 0.5 through FSC, to the Nordic Seas, while the NIIC supplies about 0.9 ± 0.1 Sv of AW (Østerhus et al., 2019). The NwAC experiences considerable cooling as it flows northward adjacent to the Norwegian Coast and in the interior of the Norwegian Sea (Figure 1.1). A branch of the NwAC flows into the Barents Sea (~2 Sv, Ingvaldsen et al., 2002), while the bulk of the current flows northward along western Svalbard, as the West Spitsbergen Current, before either exiting through Fram Strait (~3.2 ± 0.2 Sv, Beszczynska-Möller et al., 2012) or recirculating southward to join the EGC (Kawasaki & Hasumi, 2016). The transport estimates are given as an indication of the relative scale of the transports, however, different methods and measurement periods can result in large discrepancies between estimates (Fahrbach et al., 2001).

The smaller inflow branch, the NIIC, is gradually cooled through interactions with the atmosphere and other water masses as it flows along the shelf break of the North Icelandic Shelf (Semper et al., 2022). The volume transport of AW within the NIIC steadily decreases eastward on the shelf, despite, arguably, at some point receiving a contribution from the East Icelandic Current (EIC, Macrander et al., 2014; Semper et al., 2022). Toward the eastern limit of the North Icelandic Shelf, the NIIC is almost absent, before the current likely merges with the Atlantic Inflow across the IFR (Semper et al., 2022).

In addition to the warm and high salinity Atlantic-origin contribution from the recirculation at Fram Strait, the EGC also transports cold and fresh Polar Surface Water (PSW) and another branch of Atlantic-origin water which has circumnavigated the Arc-

tic Ocean (Mauritzen, 1996; Håvik et al., 2019). The EGC carries this combination of water masses southward, along the eastern continental slope of Greenland, with the PWS mainly transported near the surface above the shelf. In contrast, the Atlantic-origin waters are mainly located off the shelf, at mid-depth. The water masses of the EGC are modified by mixing with water masses of the Greenland and Iceland Seas and occasionally the atmosphere, as the current may be ventilated during winter when the sea-ice edge retreats toward Greenland, as it flows toward Denmark Strait (Våge et al., 2018; Håvik et al., 2019).

Upstream of Denmark Strait, north of the Blosseville Basin, the EGC bifurcates into the shelfbreak EGC (sbEGC) and the separated EGC (sepEGC, Våge et al., 2013). The two EGC branches flow southward on opposite sides of the Blosseville Basin, leading the sepEGC to approach Denmark Strait on the Icelandic side, before flowing out of the Nordic Seas through Denmark Strait (Våge et al., 2018; Håvik et al., 2019). Another current separates from the EGC farther upstream, the EIC, although the processes which act to detach the EIC are uncertain. The EIC flows southeastward into the southern Iceland Sea, either through the Spar Fracture Zone (de Jong et al., 2018) or on the North Icelandic Shelf (Casanova-Masjoan et al., 2020). The EIC is then thought to partly merge with the NIIC (Casanova-Masjoan et al., 2020; Semper et al., 2022) or flow eastward farther north, before entering the Norwegian Sea (Macrander et al., 2014; de Jong et al., 2018).

The southward transport from the Nordic Seas and the Arctic Ocean to the North Atlantic is classified into outflows and overflows. The outflows, such as those transported through Denmark Strait and southward west of Greenland (through the Canadian Arctic Archipelago), consist of relatively light, cold, and fresh PSW from the Arctic Ocean (Østerhus et al., 2019). The overflows consist of plumes of dense water masses, of Atlantic- and Arctic-origin, which spill over relatively deep passages in the Greenland-Scotland Ridge. The overflow waters are characterized by a density higher than $\sigma_\theta = 27.8 \, \text{kg m}^{-3}$ (Dickson & Brown, 1994; Harden et al., 2016).

The two most considerable contributions to the overflows are those through Denmark Strait, the Denmark Strait Overflow (DSO, $\sim 3.2 \pm 0.5$ Sv), and the FBC, the Faroe-Bank Channel Overflow (FBCO, $\sim 2.0 \pm 0.3$ Sv, Østerhus et al., 2019; Semper et al., 2019a, 2020). Two smaller overflows also exit the Nordic Seas across the IFR (0.4 ± 0.3 Sv) and the Wyville Thomson Ridge (0.2 ± 0.1 Sv). The sbEGC (0.8 ± 0.3 Sv) and sepEGC (1.3 ± 0.4 Sv) are the main pathways of the Atlantic-origin water to the DSO (Våge et al., 2013; Harden et al., 2016). The Arctic-origin water is brought to Denmark Strait and the FBC primarily by the NIJ (1.8 ± 0.3 Sv, Jónsson, 1999; Semper et al., 2019a) and the IFSJ (1.4 ± 0.2 Sv, Chafik et al., 2020; Semper et al., 2020). However, the upstream pathways of the flow through FBC are less certain, as a possibly intermittent, southward flowing current from the Norwegian Sea, might also be important for the FBC overflow (Chafik et al., 2020). The Arctic-origin water masses constitute the densest component of the DSO and FBCO and are thus integral to the ventilation of the deep and intermediate North Atlantic (Buckley & Marshall, 2016).

The source of Arctic-origin water is thought to have changed during the last cou-

ple of decades, given that the water masses contained in the NIJ and IFSJ have been more or less constant historically (Huang et al., 2020; Våge et al., 2022). The interior Iceland Sea was a promising candidate for producing sufficiently dense, intermediate water masses, as it had historically been known to produce such water masses (Swift & Aagaard, 1981). Presently, however, the water masses formed in the Iceland Sea are of insufficient density to supply the densest constituents of the DSO and FBCO ($\sigma_\theta =$ 28.05 kg m^{-3}, Moore et al., 2015; Våge et al., 2022). The source of this densest constituent of the DSO and FBCO is thus limited, within the Nordic Seas, to the Greenland Sea, where the new class of Greenland Sea Arctic Intermediate Water (GSAIW, Brakstad et al., 2019) is produced at a sufficient rate and density (Moore et al., 2015; Brakstad et al., 2019; Våge et al., 2022). The pathways of the GSAIW from the Greenland Sea to the Iceland Sea are uncertain. However, there are indications of a direct pathway in the western Iceland Sea, along the Kolbeinsey Ridge (Huang et al., 2019), and another, less specific, indication of pathways along ridges and through smaller gaps in the complex bathymetry, which converge in the Iceland Sea (Huang et al., 2020; Brakstad et al., 2023a).

One of the recently discovered pathways of overflow water out of the Nordic Seas is the IFSJ (Semper et al., 2020). The IFSJ is a relatively cold and saline bottom-intensified jet, which is first observed north of the north Icelandic slope, in proximity to the NIJ (Semper et al., 2020). The IFSJ consists of two bottom-intensified cores, one located deeper and farther offshore (~1100 m isobath) than the other (~750 m isobath). Both bottom-intensified cores are associated with up-titled isopycnals at depth (Semper et al., 2020). The IFSJ follows the bathymetry as it flows along the IFR toward the Faroe Islands (Semper et al., 2019a; Chafik et al., 2020). East of the Faroe Islands, the pathway of the current is less certain. However, the IFSJ is assumed to somehow navigate the complex bathymetry of the FSC and FBC before entering the North Atlantic (Chafik et al., 2020; Semper et al., 2020). Although the equatorward transport of dense water masses through the FSC and FBC has been observed for decades (Turrell et al., 1999), the upstream pathways were only recently mapped (Chafik et al., 2020; Semper et al., 2020; Chafik et al., 2023), and much remains to be ascertained.

The North Icelandic Jet

Many historical contributions have culminated in our understanding of the NIJ and the surrounding circulation. The significance of the DSO was first recognized by Cooper (1955), who identified overflows as a major source of dense water to the North Atlantic. The importance of the DSO as the source of North Atlantic Deep Water was later reemphasized and the notion that the densest components could originate from the Iceland Sea was introduced (Swift et al., 1980; Swift & Aagaard, 1981; Livingston et al., 1985; Swift & Smethie, 1989). This was supported by tracers and water mass analysis, which pointed to the densest portion of the DSO originating from winter-time, open-ocean convection in the Iceland Sea (Livingston et al., 1985; Swift & Smethie, 1989). It was later argued that water masses from the Arctic Ocean and modified AW were more probable contributors to the DSO. This was supported by the preexisting notion of a dynamical separation of the Iceland Sea from the pathways upstream of Denmark Strait, and new measurements showing congruence between the water masses of the EGC and the DSO (Mauritzen, 1996).

Upstream of Denmark Strait, observations of isopycnals tilted upward toward the Icelandic Slope were interpreted as recirculating EGC water, too dense to overflow the Denmark Strait sill (Rudels et al., 2002). However, with the use of direct velocity measurements, this isopycnal tilt was instead found to be associated with a southward flowing, mid-depth intensified current – the NIJ (Jónsson, 1999; Jónsson & Valdimarsson, 2004; Våge et al., 2011). The upstream pathways of the current were still questioned, especially east of the Kolbeinsey Ridge, as upstream observations were sparse (Våge et al., 2011; Jónsson & Valdimarsson, 2012).

Since the NIJ's discovery, the current's water mass properties, vertical structure, and pathway have been thoroughly studied. The properties of the NIJ are relatively uniform from its emergence northeast of Iceland to shortly upstream of Denmark Strait (Semper et al., 2019a). The NIJ's transport mode, the mode of the transport distribution when partitioning the volume transport by temperature and salinity, corresponds to a density of $\sigma_\theta = 28.05$ kg m^{-3} and is confined to a Conservative Temperature range of $-0.29° \pm 0.16°$C and an Absolute Salinity range of 35.075 ± 0.006 g kg^{-1} (Semper et al., 2019a). This is consistent with the current consisting primarily of Arctic-origin water masses from the Greenland Sea (Huang et al., 2019), with little entrainment of, or mixing with other water masses. However, shortly upstream of Denmark Strait, the current intermittently merges with the sepEGC (Figure 1.1), which does modify its water mass properties approaching Denmark Strait (Harden et al., 2016).

The structure of the NIJ is generally quite persistent as it follows the 600 m isobath along the north Icelandic slope. The mid-depth intensified current is associated with diverging isopycnals away from the slope, consisting of up-tilted isopycnals toward the slope at depth and down-tilted isopycnals toward the slope aloft (Pickart et al., 2017). This structure is partly what allows the NIJ to overflow Denmark Strait, despite containing water masses typically located beneath the Denmark Strait sill depth ($\sim$650 m). The isopycnal divergence and a mid-depth intensified westward current is consistent with the thermal wind balance (Section 2.1).

The up-tilted isopycnals at depth have previously been attributed to frictional effects between the NIJ and the bottom, as the bottom Ekman layer would produce an Ekman transport up the slope ($90°$ left of current direction on the northern hemisphere, Jónsson & Valdimarsson, 2004). However, the isopycnal up-tilt is a relatively constant feature along the northeast Icelandic slope and the IFR where the NIJ is weaker and absent, respectively (Semper et al., 2019a, 2020). Nevertheless, indications of relatively strong up-slope velocities associated with the NIJ have been observed, which indicate that the effect of the bottom Ekman layer is present when the current is strong and in contact with the slope (de Jong et al., 2018), implying that the bottom Ekman layer does indeed play a part (de Jong et al., 2018; Semper et al., 2019a). A similar up-tilt is also associated with the IFSJ, where the bottom-intensified, eastward current is consistent with the isopycnal structure through the thermal wind balance, but not consistent with an onshore bottom Ekman flow (Section 2.1, Semper et al., 2020).

The NIJ intermittently exhibits a second, outer core (Pickart et al., 2017), located slightly above and farther offshore than the inner, persistent core. Although this outer

core has been observed numerous times, with up to half of all observations of the NIJ featuring a second core, the nature of the core is still not known (Pickart et al., 2017; Semper et al., 2019a). The core has been proposed to be a separate branch of the current (Semper et al., 2019a), which intermittently branches off and merges with the main core, to be related to the downstream creation of waves or eddies which might propagate upstream (Pickart et al., 2017), or to be associated with an occasional meandering of the main core, which might manifest as two separate cores in observations.

The NIJ has been observed to emerge northeast of Iceland (Semper et al., 2019a). There, the current speed and volume transport are weak. As it flows westward, the current is supplied by dense water masses from the north (Våge et al., 2011). It grows by approximately 0.4 Sv per 100 km as it flows along the north Icelandic slope to about 1.8 Sv northwest of Iceland (Semper et al., 2019a). Downstream of this maximum volume transport the current intermittently merges with the sepEGC, and the NIJ's contribution to the DSO is more difficult to estimate (Harden et al., 2016). At Denmark Strait, the water masses associated with the NIJ are observed to on average comprise about half of the DSO ($\sigma_\theta > 27.8$ kg m^{-3}). Furthermore, the densest portion of the DSO ($\sigma_\theta > 28.03$ kg m^{-3}) is thought to be mainly supplied by the NIJ upstream of Denmark Strait (Våge et al., 2011; Harden et al., 2016), while at Denmark Strait the relative contribution of the NIJ and sepEGC is harder to distinguish (Mastropole et al., 2016; Lin et al., 2020).

The intermittent merging of the NIJ and sepEGC occurs due to the bifurcation of the EGC north of the Blosseville Basin (Figure 1.1), which leads to the sepEGC eventually flowing on the Icelandic side upstream of Denmark Strait. On seasonal time scales, the degree to which the two currents dominate each other or merge is dependent on upstream wind forcing, while higher frequency variability has been attributed to smaller scale features, such as baroclinic instabilities in both the NIJ and sepEGC (Harden & Pickart, 2018; Huang et al., 2019).

The interactions between the NIJ and the inshore, shelf break NIIC are primarily determined by the changing steepness of the north Icelandic slope (Pickart et al., 2017). In steeper regions, the two currents are brought together, as they both follow specific isobaths, and they become dynamically linked. When immediately adjacent, the density front between the currents is enhanced, destabilizing both currents (Pickart et al., 2017). Additionally, in regions where moderation of the bathymetry separates the NIIC and NIJ, a weaker, yet comparable, eastward flow takes the NIIC's place just inshore of the NIJ. This might indicate that the NIJ is to some degree dependent on, or responsible for, an adjacent eastward flow (Pickart et al., 2017).

In the steeper region where the NIJ is observed to emerge, the NIIC becomes increasingly baroclinically unstable, associated with enhanced levels of eddy kinetic energy (EKE, Semper et al., 2022). Although not directly observed in the NIIC (Semper et al., 2022), similar situations unfold in the Lofoten Basin (Northern Norwegian Sea, Figure 1.1) and the Labrador Basin, where unstable boundary currents are associated with high levels of eddy fluxes of salt and heat (Spall, 2004, 2011; Isachsen et al., 2012; Bracco et al., 2008). In these instances, the steeper part of the slope is favorable for

enhanced EKE and later fluxes into the adjacent basin (Isachsen et al., 2012), which is congruent with the heightened levels of EKE on the northeastern Icelandic slope.

Consequently, the interactions between the NIJ and NIIC, the congruence in the variability of the currents' hydrographic properties (Pickart et al., 2017), and several model studies (Våge et al., 2011; Behrens et al., 2017), led to the hypothesis of the NIIC supplying the NIJ through a local overturning loop. In this overturning loop, the meridional fluxes from the NIIC would rapidly be ventilated in the Iceland Sea (or the Nordic Seas in general, Pickart et al., 2017; Semper et al., 2019a), before flowing southward, sinking, and feeding the emerging NIJ. However, indications of a different circulation scheme (Ypma et al., 2019) weakened this hypothesis. Moreover, this overturning exchange would require a rapid and substantial water mass transformation, producing water masses of densities up to $\sigma_\theta = 28.05$ kg m^{-3}, which currently does not occur in the Iceland Sea (Våge et al., 2022). Nevertheless, the notion that instabilities in the NIIC trigger a meridional flux compensated by dense water moving southward persists, although the nature of the compensation is not understood. This exchange relies on the compensating water masses originate from other sources (Våge et al., 2011; Semper et al., 2022).

In a previously idealized modeling study, the NIJ was found to be a robust, fundamental feature of the Nordic Seas, given integral constraints which might illustrate larger-scale mechanisms behind the existence of the NIJ (Yang & Pratt, 2014). The NIJ was found to be resilient to various configurations of inflow, dense water formation, and high atmospheric forcing, which enforces the notion that the NIJ is an integral component of the circulation in the Nordic Seas (Yang & Pratt, 2014). Additionally, the sources of the NIJ have historically migrated (Våge et al., 2022), reinforcing the NIJ's resilience and fundamental importance to the circulation of the Nordic Seas. Furthermore, as the resilience of the AMOC as a whole is questioned in relation to the impacts of climate change (Chapter 1, Gregory et al., 2005; Cheng et al., 2013), the NIJ's resilience as a key pathway of dense water is all the more central.

Understanding the general attributes and pathways of the NIJ (Jónsson, 1999; Jónsson & Valdimarsson, 2004; Våge et al., 2011; Harden et al., 2016; Behrens et al., 2017; Pickart et al., 2017; de Jong et al., 2018; Semper et al., 2019a) and the central mechanisms of the NIJ's resilience, such as the integral constraints of Yang & Pratt (2014) as well as its emergence (Våge et al., 2011; Pickart et al., 2017; Semper et al., 2019a, 2022) is, therefore, an important component of assessing the future resilience of the DSO and the AMOC as a whole. Making a contribution to this understanding is thus the primary aim of this thesis.

Chapter 2

Theory

2.1 Thermal wind balance

The thermal wind balance (Equations 2.1 and 2.2) is a highly simplified set of equations, derived from the geostrophic and hydrostatic balance (Appendix A, Cushman-Roisin & Beckers, 2011), which relates the horizontal density structure to the vertical shear in geostrophic flow,

$$\frac{\partial v_g}{\partial z} = -\frac{g}{\rho_0 f}\frac{\partial \rho}{\partial x} \tag{2.1}$$

$$\frac{\partial u_g}{\partial z} = \frac{g}{\rho_0 f}\frac{\partial \rho}{\partial y} \tag{2.2}$$

where u_g and v_g are the zonal and meridional geostrophic velocity components, respectively, g is the gravitational acceleration, f is the Coriolis frequency, and ρ_0 and ρ are the reference density and density, respectively. In the specific case near the north Icelandic slope, the meridional isopycnals diverge vertically away from the slope, with southward down-tilted isopycnals near the surface and up-tilted isopycnals depth (Figure 2.1). Comparatively, the zonal density gradients are negligible. Thus, I consider Equation 2.2, representing the appropriate meridional density gradient and zonal geostrophic velocities.

The isopycnal divergence on the north Icelandic slope is associated with a non-linear vertical current shear (Figure 2.1). This can be seen through the thermal wind balance applied separately for the down-tilt near the surface, where the isopycnal tilt yields a vertically positive shear, and the up-tilt below, where the isopycnal tilt yields a vertically negative shear (Figure 2.1b,c). The actual vertical current structure depends on the barotropic component, given by the sea surface elevation tilt (Cushman-Roisin & Beckers, 2011).

Thermal Wind Balance

$$\frac{\partial u}{\partial z} = \frac{g}{\rho_0 f} \frac{\partial \rho}{\partial y} \quad \rightarrow \quad \frac{\Delta u}{\Delta z} \propto \frac{\Delta \rho}{\Delta y}$$

Meridional density transect:
Northward Divergence

Resulting zonal relative
geostrophic velocity profile

(a) ρ

$\frac{\Delta \rho}{\Delta y}$ $\frac{\Delta u}{\Delta z}$

$\frac{\Delta \rho}{\Delta y}$ $\frac{\Delta u}{\Delta z}$

z y

(b)

$\frac{\Delta \rho}{\Delta y} > 0$

$\frac{\Delta u}{\Delta z} > 0$

$\frac{\Delta \rho}{\Delta y} < 0$

$\frac{\Delta u}{\Delta z} < 0$
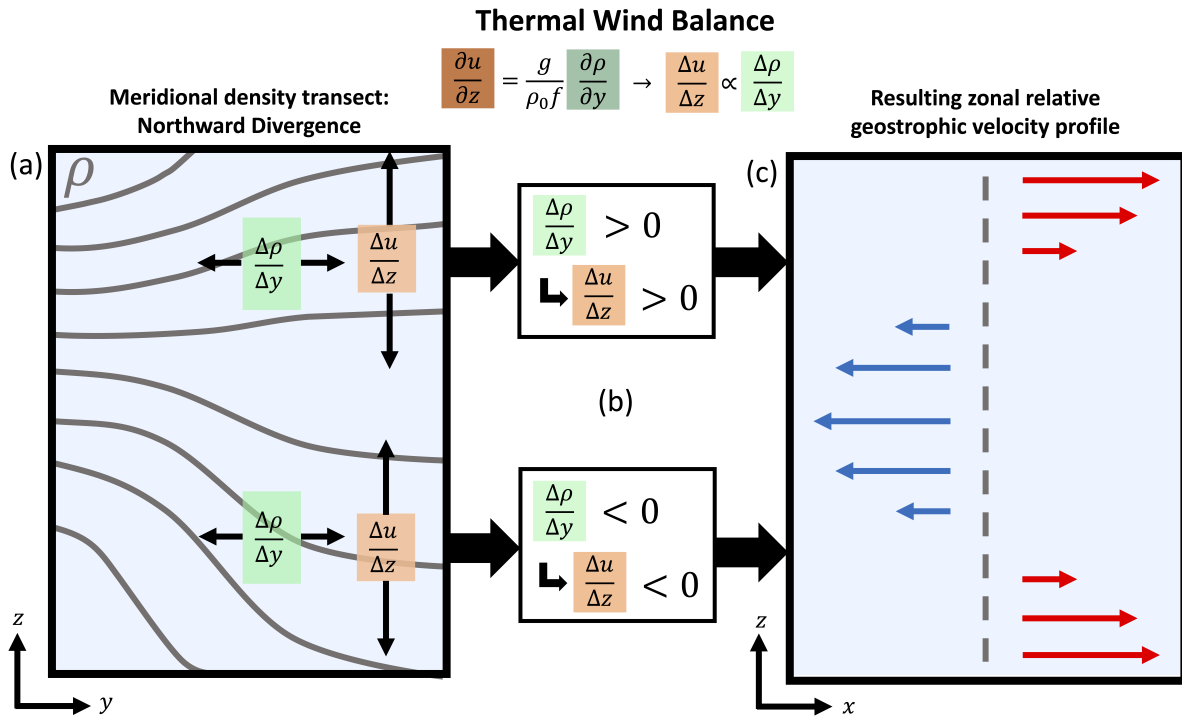
(c)

z x

Figure 2.1: Schematic of (a) meridional isopycnal structure near the North Icelandic Slope (positive y is north and positive x is east), and (b) a sign argument using the discrete thermal wind equation (Equation 2.2) for (c) the resulting zonal relative geostrophic velocity shear.

2.2 Numerical Ocean Models

Numerical ocean models are used to simulate temporal and geographical changes in the ocean through numerical approximations of the primitive equations, the most central being the equations for conservation of momentum, mass, and energy (Haidvogel & Beckmann, 1999, hereafter HB99). However, the governing equations for geophysical fluids on a rotating sphere are not feasible to solve numerically in their complete form and must be simplified considerably before being used for atmospheric or ocean modeling (HB99, Shchepetkin & McWilliams 2009). Ocean models are thus relatively similar to climate and atmospheric models in broad terms, as they apply similar numerical methods to solve comparatively simplified equations of relatively similar problems involving stratified geophysical fluids in rotating large-scale situations (HB99, Chung 2010, hereafter CH10). Numerical ocean models aim to apply these discretized equations to describe the state and development of elementary ocean variables such as temperature, salinity, and velocity. Ocean models today are used in an extensive range of applications, such as the global ocean, individual oceans, marginal seas, and smaller regions such as specific coastal regions, estuaries, or fjords, with couplings to necessary external components, such as the atmosphere, river runoff, or sea floor sediments (Shchepetkin & McWilliams, 2009).

The progress in diversity and complexity within ocean models, particularly general circulation ocean models (GCOMs), was stagnant for several decades following the initial advancements in the 1960s, especially relative to other fields within computational

fluid dynamics (e.g. numerical weather prediction). This stagnation lasted from the late 1960s to the early 1980s, when a small number of largely similar, and rather primitive, approaches of low-order GCOMs remained prominent, as a result of insufficient innovation in the application of GCOMs and fierce competition for sufficient computing power (HB99).

Throughout the past four decades, however, increased interest, effort, and the availability of greater computational capabilities in the field resulted in a surge in the diversity of both sophisticated and simple ocean models. During the early part of this development, a wide variety of new or repurposed approaches to several aspects of ocean modeling sprang forth, such as vertical, horizontal, and temporal discretization (HB99). The following section will primarily feature a general summary of the characterization, fundamental function, and diversity of elements in ocean models, their impact on model performance, and important fundamental considerations when designing an ocean model (Figure 2.2). Specific methods or concepts, such as parameterizations of subgrid-scale processes, parallelization, or treatment of river runoff are outside the scope of this section.
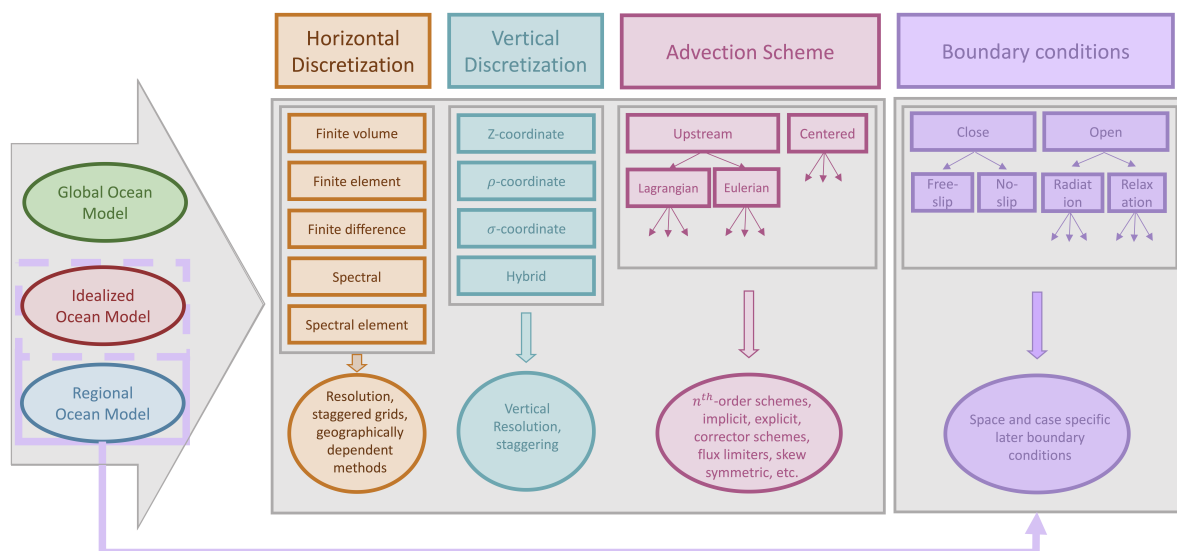

Figure 2.2: Schematic of some general ocean model categories (top boxes) and choices within each category (lower boxes), including the main types of horizontal and vertical discretizations, and advective schemes. The boundary conditions box is separate to indicate that global ocean models and some idealized models do not consider these. Some additional considerations within each choice are listed in the circles below, which to varying extents are relevant for every choice listed. The arrows in the advection scheme and boundary conditions categories indicate sub-choices and three downward arrows indicate the existence of further sub-choices. Some aspects of the figure are adapted from (HB99)

Vertical discretization

We commonly characterize ocean models by their approach to spatial discretization (Figure 2.2). Vertical discretization in ocean models is mainly grouped into geopoten-

tial (z), terrain following (σ), and isopycnal (layered or s) coordinates, although combinations of these (hybrid) also exist. Each convention has advantages and disadvantages, which must be considered in light of the application. For z-coordinates, where the vertical coordinate is defined by the distance from the resting ocean surface (Fig. 2.3a), advantages include simplicity in application and good treatment of weakly stratified situations, whereas it performs poorly in the interior basins and near sloping bathymetry. The poor performance in the interior basins is due to there commonly being lower resolution, and near sloping bathymetry due to the bottom layer's staircase-like structure (Winton et al., 1998). Conversely, σ-coordinates, where the vertical coordinate follows the bathymetry (Figure 2.3b), generally perform better near sloping bathymetry and with the resolution of model variables close to the bottom, despite problems with pressure gradient forces in regions with large density gradients or steep bathymetry (Berntsen & Thiem, 2007). Lastly, isopycnal coordinates, using isopycnal surfaces as the vertical coordinate (Figure 2.3c), perform well under most highly stratified conditions while being heavily disadvantaged in weakly stratified situations and regions of high cross-isopycnal mixing (Chassignet et al., 2003).
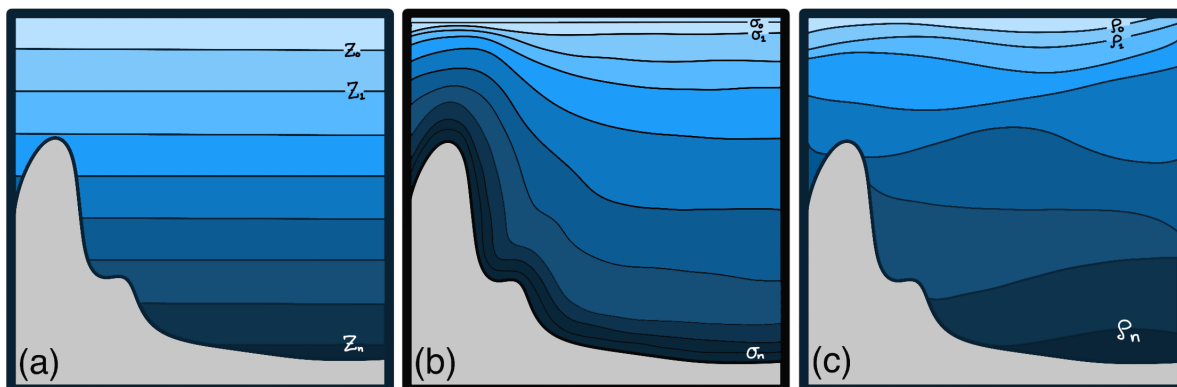

Figure 2.3: Schematic of approaches to vertical discretization in ocean models, including z-coordinate (a), σ-coordinate (b), and s-coordinates (c). Modified from a number of books and lecture notes.

Naturally, within the respective vertical coordinates, additional considerations of vertical layering, layer distribution, and vertical staggering must be made. In the three configurations, the number of vertical layers can be arbitrarily chosen depending on computational demands and the distribution of said layers can be distributed unevenly where needed. This primarily involves models using a computationally feasible number of vertical layers with an increased resolution near the surface and bottom. Additionally, vertical staggering, where variables acting in the vertical (e.g. vertical velocity) are displaced to the upper and lower limits of the respective grid cells is common (Winton et al., 1998; Chassignet et al., 2003; Berntsen & Thiem, 2007).

Horizontal discretization

The three most widely used approaches to horizontal discretization are finite difference, finite element, and finite volume grids (Figure 2.4, CH10), while spectral grids are more frequently applied in other applications (e.g., atmospheric models) or combined with the finite element method (Figure 2.2, HB99; CH10). The conventions are

associated with inherent advantages and disadvantages, similar to vertical discretiza-tion, which must be considered according to the application.

Finite difference grids (Figure 2.4a), being structured orthogonal coordinates (often thought of as grid "boxes"), are the most widely used, especially in open ocean and general circulation models, due to relatively simple application and generally good results (CH10). A disadvantage of finite difference grids is the generally poor coastal resolution, particularly in estuary and coastal studies. However, this problem can be mitigated by downsizing the grid size close to complex coastal features (nested grid HB99).
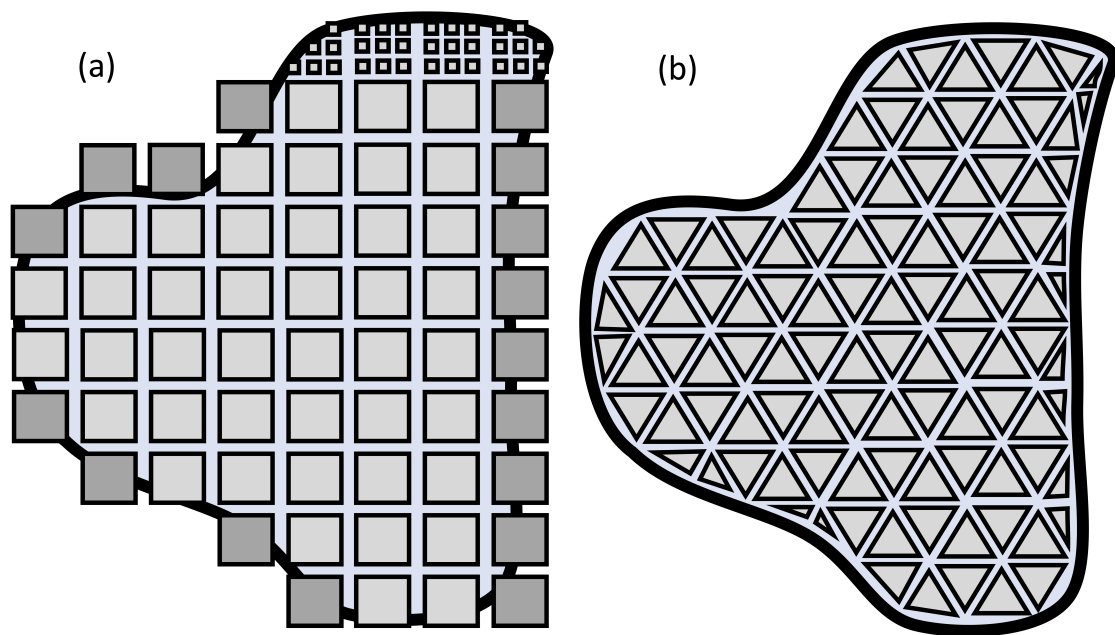

Figure 2.4: Schematic of approaches to horizontal discretization in ocean models, namely finite difference (a) and finite element or finite volume (b). The light gray boxes in a and b indicate the grid cells which fall within the domain, the dark gray boxes in a indicate those that would fall outside the domain, and the smaller boxes in a indicate the use of downsized nested grids.

Finite element grids are also a commonly applied horizontal grid discretization in ocean models, previously used mostly in intermediate or small-scale estuary and coastal studies, but more commonly applied in larger-scale models recently, consisting of an unstructured mesh of a finite number of unevenly sized polygons, often triangles (Fig-ure 2.4c, HB99; CH10). Finite element grids are advantageous for resolving com-plex coastlines, as the unevenly sized triangles can be adjusted to the contour of said coastline. The disadvantage of such grids is mainly the complexity of their applica-tion (CH10). The last class of horizontal grid discretizations, the finite volume grid, is similar to finite element grids, consisting of an unstructured mesh of unevenly sized polygons. However, it differs in solving the primitive equations on the grid. Instead of solving the partial form of the primitive conservation equations, it solves the integral form of the conservation equations (Neill & Hashemi, 2018). Thus, the finite volume grid retains the same advantages as the finite element grid, in addition to enhanced ac-curacy and stability of the solutions, while being further disadvantaged by enhanced

complexity of application (HB99; CH10, Neill & Hashemi 2018).

After a horizontal discretization method is chosen, sub-groups of these must also be considered. Each sub-group depends on the method and can include different staggering configurations, regions of higher resolution, and the resolution both in the whole domain or specific nested regions (HB99; CH10).

Advection schemes

Another important, and equally fundamental, aspect of general circulation ocean models is the numerical discretization of the governing equations. The two main categories are the upstream and centered difference schemes (Figure 2.2), named according to which positional discretization is used to obtain the next discrete timestep. For instance, for the one-dimensional linear advection equation

$$\frac{\partial u}{\partial t} + a\frac{\partial u}{\partial x} = 0 \tag{2.3}$$

where a is the propagation speed of a wave. The first-order forward-in-time upwind (Equation 2.4) and centered (Equation 2.5) schemes take the form

$$\frac{u_i^{n+1} - u_i^n}{\Delta t} + a\frac{u_i^n - u_{i-1}^n}{\Delta x} = 0 \, , \, a > 0 \tag{2.4}$$

$$\frac{u_i^{n+1} - u_i^n}{\Delta t} + a\frac{u_{i+1}^n - u_{i-1}^n}{\Delta x} = 0 \tag{2.5}$$

where i is the spatial index, corresponding to the ∂x derivative and x dimension, and n is the temporal index, corresponding to the ∂t derivative and t dimension (CH10). The upstream and centered schemes have inherent advantages and disadvantages, which cascade down as more complex configurations retain the most fundamental characteristics. The application of the upstream and centered difference schemes differs considerably depending on the choice of finite difference, element, or volume methods (HB99; CH10).

The most fundamental considerations for such schemes are convergence, consistency, stability, and order of accuracy. Such properties are generally well documented (HB99). Moreover, each available scheme contains an nth order configuration, where the order is given by the number of terms retained when discretizing the advection equation, and dictates the accuracy of the scheme. High-order accuracy schemes yield a higher computational cost, due to the higher number of terms in the calculation (HB99; CH10).

Additionally, to improve the convergence, consistency, or accuracy, advection schemes can be reinforced with correction schemes, flux limiters, and, if the given scheme is of a lower order, can be reinforced by higher order schemes at given time intervals (Shchepetkin & McWilliams, 2009). As such, the primary considerations are reduced to weighting between scheme accuracy and computational cost, as well as differences in the way errors manifest between schemes and which schemes perform better in concert with other elements of the model. Additionally, as separate schemes can be

applied to different components of the dynamical model, such as depth-integrated horizontal, horizontal, vertical, and tracer advection, weighting between the accuracy of these components also needs consideration (HB99, Shchepetkin & McWilliams 2009).

An inherent property that arises from discretizing the advection equation is the stability of the given solution (Haidvogel & Beckmann, 1999). Although the stability condition for different schemes manifests differently depending on their properties, the condition generally takes the form of the Courant Friedrichs Lewy (CFL) criterion. The one-dimensional form of the CFL criterion is shown below (Equation 2.6),

$$C = \left(\frac{c\,\Delta t}{\Delta x}\right) \leq 1 \qquad (2.6)$$

where C is the Courant number, c is the phase speed, Δt is the timestep, and Δx is the horizontal resolution. The CFL criterion acts as a restriction between the timestep and horizontal resolution, as increasing the horizontal resolution requires a corresponding increase in temporal resolution (HB99). A violation of this condition ($C > 1$) can conceptually be interpreted as calculating the next time step using an unknown value, located farther upstream than the scheme intends. Another conceptual interpretation is that the Courant number gives the speed at which information travels across a grid cell, thus, propagating information is not retained within the cell if $C > 1$ and is thus not represented in the next cell at the next timestep. The treatment and restrictiveness of the CFL criterion vary between schemes, which also comes into account when electing a scheme (HB99).

Boundary conditions

Boundary conditions are fundamental components when solving partial differential equations (CH10), whether it pertains to the surface, bottom, or lateral boundaries (HB99). However, in ocean models, the surface and bottom boundary conditions are individually treated as atmospheric forcing and bottom friction (unless sediment and seafloor are explicitly characterized), respectively (HB99). In contrast to GCOMs and some global idealized models, regional and idealized ocean models inherently need to implement lateral boundary conditions (LBCs) when limiting their domain to certain oceanic areas. These LBCs, especially if applied poorly, can significantly impact the circulation within the model. The configuration of LBCs must be considered for each unique application, as all LBCs contain certain advantages and disadvantages. The two main categories of LBCs are open and closed (Marchesiello et al., 2001)

Closed LBCs are often thought of as a vertical wall at the boundary of the domain where no perpendicular advection or exchange of information takes place. In contrast, tangential advection is subject to a predetermined level of friction, ranging from a perfectly slippery surface to high levels of drag (Marchesiello et al., 2001, Figure 2.2). The closed LBC is often used for boundaries that are meant to represent land or ocean areas thought to be inconsequential or uninteresting in terms of advective exchanges.

Open LBCs are meant to simulate adjacent ocean areas important for advective exchanges or hydrographic influence but are not included in the model domain. This exclusion can either be because the external ocean area is adjacent to a marginal sea,

coastal area, or estuary, simulated with a separate, coarser model setup, or simply outside the scope of the given study. Open LBCs must therefore account for incoming and outgoing advection of tracers and momentum, and conserve volume while not impeding outgoing signals or creating erroneously large incoming signals.

The three main categories of open LBCs are the radiation, relaxation, and periodic schemes, the two former with multiple sub-configurations. The radiation LBC's central principle is to let deviations from the predetermined exterior value (outgoing signals) radiate out of the model domain. The relaxation LBC instead simply smooths outgoing signals in a designated region close to the boundary, a so-called restoring or sponge zone (Marchesiello et al., 2001). The periodic LBC is distinct from the other two open LBCs, as it simply sets all values of parallel boundaries equal ($\phi(x = N) \equiv \phi(x = 0)$, where ϕ is an arbitrary variable and $x = 0$ and $x = N$ are parallel boundary indexes, respectively).

Idealized oceanic general circulation models

In this study, I conduct simulations with a regional, idealized model setup, to study physical processes. Idealized models are convenient tools when studying complicated physical mechanisms in large- or intermediate-sized geographical regions, as the region can be reduced to the most fundamental features and physical processes can be isolated. Hypotheses can be more readily tested by systematically applying changes to model aspects, such as bathymetry, external forcings, and hydrography. Idealized simulations are less costly than complex regional models and far more manageable to design. When combined with observations, regional ocean models, or global ocean models, idealized models offer a fundamental, knowledge bridging, opportunity. In this capacity, idealized models can aid the design of observational surveys, contributing to the understanding of the temporal and spatial resolutions sufficient to capture the governing processes.

There are also some key advantages of using idealized models in contrast to other ocean models. Comprehensive global and regional ocean models are rapidly improving in terms of simulating ocean processes, while correspondingly increasing in complexity and computational cost. While these improvements are groundbreaking and pioneering in bringing the field forward, studies on fundamental ocean mechanisms are not plausible due to the sheer complexity of the models, in addition to being computationally impractical. The use of idealized oceanic models is therefore distinct from other ocean modeling practices, as the ultimate goal is not to simulate reality perfectly. Instead, idealized ocean models aim to design small, application-specific, and less complex configurations, to study specific ocean processes. Consequently, iteratively withholding and including components, as well as applying precise changes to said components can be more easily achieved without high computational cost.

2.3   The Regional Ocean Modelling System

In this study, I have designed an idealized ocean model in the Regional Ocean Modelling System (ROMS). I will now expand upon some of the more specific considerations and errors associated with the configurations of horizontal and vertical discretization, advective schemes, and boundary conditions in ROMS.

Vertical discretization in ROMS

ROMS apply free-surface σ-coordinates (terrain-following Song & Haidvogel, 1994), with customizable stretching and an optional number of layers. Thus, errors in calculating the internal pressure gradient (IPG) must be acknowledged (Section 2.2). IPG errors are inherent to σ-coordinate models and arise due to truncation errors in the numerical solution of the internal density gradient, which then directly impact the IPG calculation (Berntsen & Thiem, 2007). The zonal (x) component of the density gradient in σ-coordinates, neglecting the effects of the free surface, are given in Equation 2.7

$$\frac{\partial \rho}{\partial x}\bigg|_z = \frac{\partial \rho}{\partial x} - \frac{\sigma'}{H}\frac{\partial H}{\partial x}\frac{\partial \rho}{\partial \sigma'},\tag{2.7}$$

where ρ is the density, x and z are the Cartesian horizontal and vertical coordinates, H is the depth, and $\sigma' \equiv z/H$. In the analytical solution to Equation 2.7 when $\rho = \rho(z)$, the two terms on the right-hand side are equal and cancel each other out. However, the numerical solutions of both right-hand side terms create truncation errors which when solved leave a net error. The magnitude of this net truncation error depends on the order of the numerical scheme but is non-zero for all computationally feasible schemes (Berntsen & Thiem, 2007). This density gradient error directly influences the pressure gradient of the model through the following relationship (Equation 2.8),

$$\frac{\partial P}{\partial x}\bigg|_z = -gH\int_\sigma^0\left(\frac{\partial \rho}{\partial x} - \frac{\sigma}{H}\frac{\partial H}{\partial x}\frac{\partial \rho}{\partial \sigma}\right),\tag{2.8}$$

where P is the pressure and g is the gravititonal constant. Thus, the relative magnitude of the density gradient is brought into the momentum equations through the pressure gradient term (Berntsen & Thiem, 2007). In ROMS, these errors are reduced by a numerical algorithm (Shchepetkin & McWilliams, 2003).

Horizontal discretization and horizontal and vertical staggering in ROMS

ROMS apply finite difference, orthogonal curvilinear coordinates with multiple nesting options for higher resolution near for instance complex coastlines. Thus, designing the grid, in terms of the general shape, resolution, and nesting near coasts, is relatively simple compared to finite element, finite volume, and spectral-element grids (Section 2.2).

Horizontal staggering offers diverse options and considerations, as several variables benefit from the staggering. The advantages and disadvantages of the different conventions of unstaggered, Arakawa A-grid, and staggered grids, Arakawa B-, C-, D-, and

E-grid (rotated B-grid), are complex, as it largely pertains to how signals (e.g. inertia-gravity and planetary waves) propagate in the domain (Figure 2.5a, HB99). Generally, however, the Arakawa B-grid and C-grid perform best in coarse and fine resolution simulations, respectively (HB99). Thus, since ROMS is designed to facilitate high-resolution regional studies, the Arakawa C-grid is used (Figure 2.5b, Shchepetkin & McWilliams, 2005). The temperature, salinity, and sea surface elevation are located on the ρ coordinate, while the zonal and meridional velocities are located on the u and v coordinates, respectively (Figure 2.5).
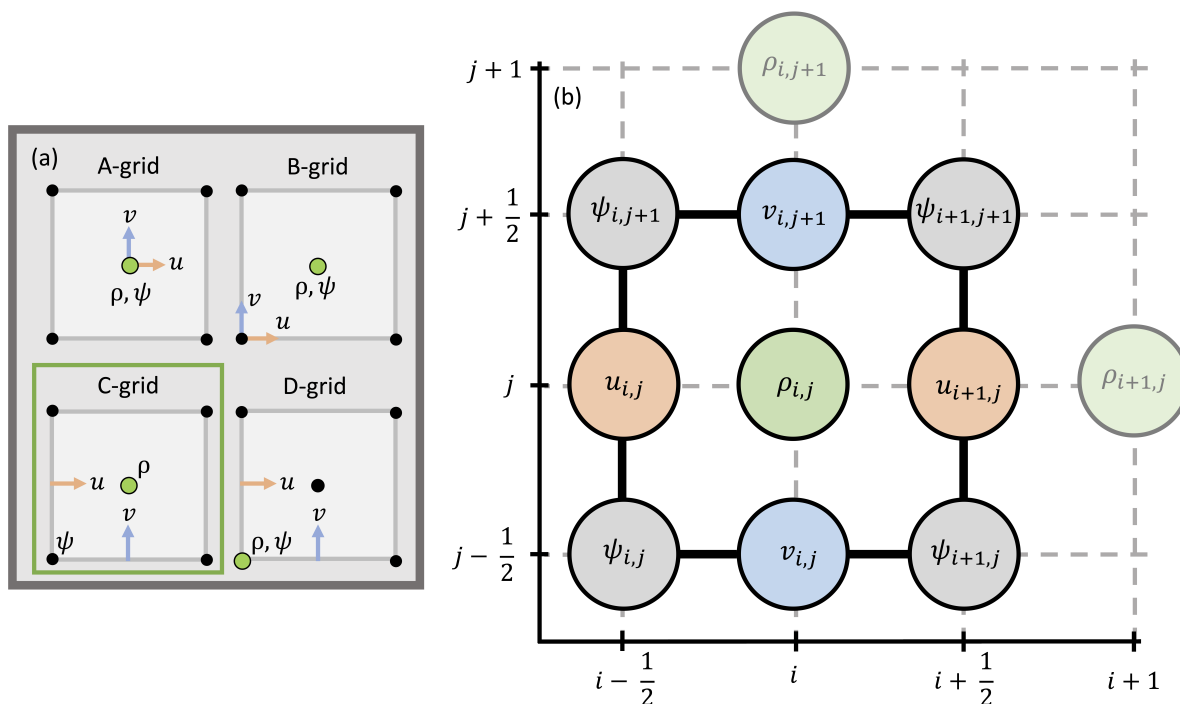

Figure 2.5: Schematic of (a) the different horizontally staggered grids adapted from HB99 and (b) the specific configuration of the Arakawa C-grid used in ROMS adapted from wiki ROMS (2016). The arrows in (a) indicate the location of the u and v coordinates while the green circle indicates the location of the ρ coordinate, with a color scheme consistent with the more detailed schematic in (b). The solid black square in (b) illustrates the horizontal grid cell centered around the horizontal coordinate index i (zonal) and j (meridional) of the ρ coordinate (green), the colored circles show the location of the other coordinates, u (orange), v (blue), and ψ (gray), using their own respective indices (displaced half a grid cell in both or one direction from ρ). The axes show the corresponding horizontal coordinate index of the ρ coordinate. The slightly transparent green circles show the adjacent grid cell centers.

Advection Scheme in ROMS

ROMS contains several options for advection schemes, where different schemes can be specified for particular tracers, vertical and horizontal advection, and the baroclinic and barotropic modes. The available advection schemes include several upstream and centered schemes of varying order and options for additional components that limit the erroneous components in each scheme (Shchepetkin & McWilliams, 2005).

Numerical stability in ROMS

In ROMS, like most other ocean model systems, an advanced computational algorithm is used to optimize the computational efficiency, while retaining stability according to the CFL criterion (Section 2.2, Shchepetkin & McWilliams, 2009). The most fundamental aspect of this computational algorithm is the partitioning of a fast mode (barotropic, two-dimensional) and a slow mode (baroclinic, three-dimensional), where the timestep of each mode is optimized to reduce the computational cost while retaining stability. In practice, this involves solving the equations separately, with different temporal resolutions for the two modes. The two modes communicate at different times throughout the computation of a single, baroclinic timestep (Figure 2.6. This partitioning is possible and economical since the fastest propagating signal in the ocean is two-dimensional, horizontally propagating internal waves (Shchepetkin & McWilliams, 2009). By doing this, the less computationally costly, barotropic, two-dimensional component has a high phase speed being the fast internal waves, and thus requiring higher temporal resolution. Consequently, the phase speed of the baroclinic signal is considerably lower, and a coarser temporal resolution can be used for the more computationally costly mode. Due to this partitioning, multiple specific configurations
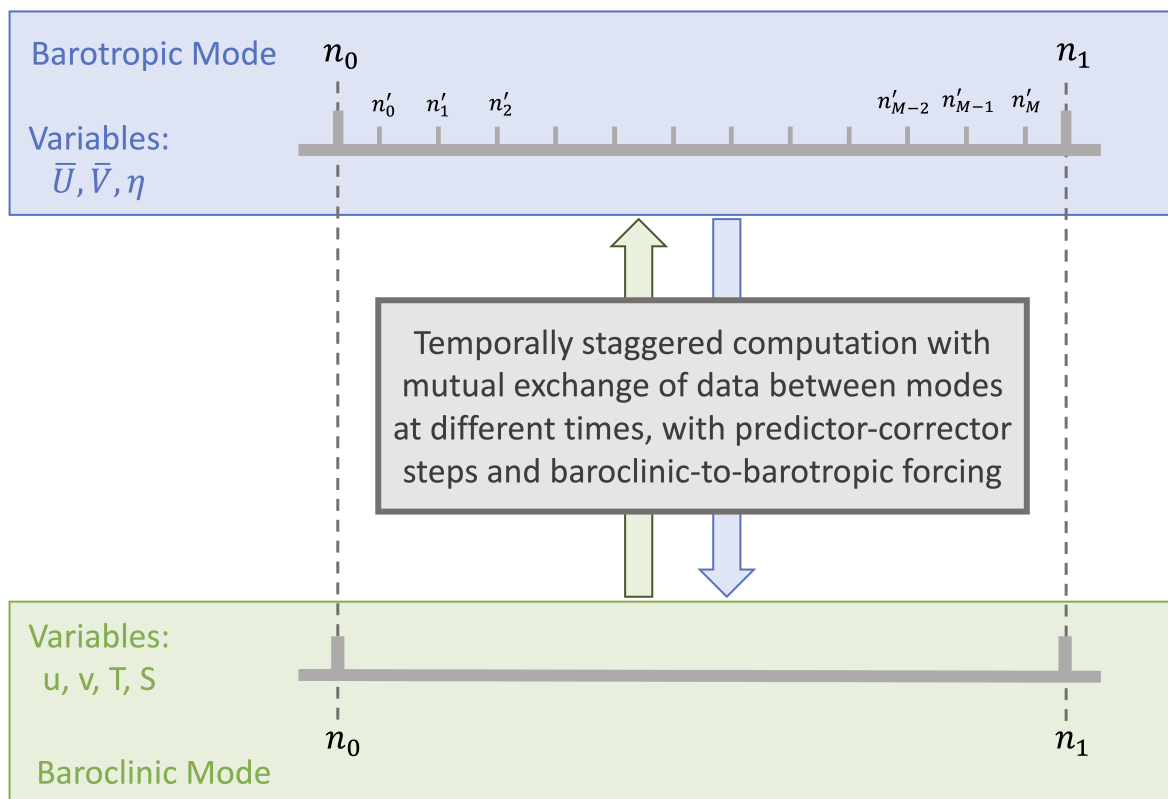

Figure 2.6: Schematic of the general aspects of timestepping procedures used in ocean models. The index n indicates the baroclinic timesteps and the index n' indicates the barotropic timesteps. Modified from Shchepetkin & McWilliams (2009).

of the CFL criterion arise, as different processes contain different scales of speed and are computed with either mode or coupling of the two. The most important are the CFL condition for the baroclinic mode (Equation 2.9a), which is analogous to the standard

CFL criterion (Equation 2.6), the barotropic mode (Equation 2.9b), which relates to the external wave propagation, and the internal wave speed (Equation2.9c) as follows

$$C = \Delta t_S \left(\frac{c_S}{\sqrt{\Delta x^2 + \Delta y^2}} \right) \leq C_{max} \tag{2.9a}$$

$$C_F = \Delta t_F \left(\frac{c_g}{\sqrt{\Delta x^2 + \Delta y^2}} \right) \leq C_{F,max} \quad , \quad c_g = \sqrt{gh} \tag{2.9b}$$

$$C_{IW} = \Delta t_S \left(\frac{c_{IW}}{\sqrt{\Delta x^2 + \Delta y^2}} \right) \leq C_{IW,max} \tag{2.9c}$$

where the subscript F indicates variables associated with the fast, barotropic mode, the subscript S indicates variables associated with the slow, baroclinic mode, c_g is the external phase speed, and c_{IWS} is the internal wave phase speed. The conditions, C_{max}, $C_{F,max}$, and $C_{IW,max}$, indicate that each criterion is subject to differing restrictions.

Lateral Boundary Conditions in ROMS

ROMS is specifically designed for regional ocean modeling, which prompts the careful consideration inherent when choosing open and closed LBCs (Section 2.2). Thus, a wide range of options for LBCs is available (Table 2.1).

Table 2.1: Lateral Boundary Conditions (LBCs) available in ROMS (wiki ROMS, 2019). The short names are those used in the ROMS input files. The application of the LBCs indicates whether the boundary condition is used for the barotropic mode or the free-surface, while the three-dimensional LBCs are all used for the baroclinic mode. The type of boundary condition is explained in the text.

Short name	Long name	Dimensions	Application	Type
Cha	Chapman Implicit	2	Free-surface	Radiating
Che	Chapman Explicit	2	Free-surface	Radiating
Cla	Clamped	3		Relaxation
Clo	Closed[1]	3		Free- or non-slip
Fla	Flather	2	2D-momentum	Radiating
Gra	Gradient	3		Relaxation
Nes	Nested	3		Refinement
Nud	Nudging	3		Relaxation
Per	Periodic	3		Cyclic
Rad	Radiation	3		Radiating
Red	Reduced Physics	2	2D-momentum	Radiating
Sch	Shchepetkin	2	2D-momentum	Radiating
RadNud	Radiation and Nudging	3		Combined

[1] The specific properties of the closed lateral boundary condition are specified through other parameters in the model code.

ROMS features three LBC configurations of the Relaxation type (Section 2.2), the Clamped, Gradient, and Nudging, which are relatively similar in treating interior values approaching the boundary. The Clamped LBC simply sets the value at the boundary

($x = 0/N$) equal to a predefined value. The Gradient LBC instead forces the gradient in a variable to approach zero at the boundary. The Nudging LBC nudges, or forces, the interior values to approach a predefined value at the boundary within a certain nudging, or sponge, region away from the boundary (wiki ROMS, 2019).

Six radiating LBC configurations are available: the Chapman Implicit and Explicit, the Flather, the Radiation, Reduced Physics, and Shchepetkin. They are all relatively similar in terms of the treatment of outgoing signals. The Chapman Explicit and Implicit, Flather, Reduced Physics, and Shchepetkin are all two-dimensional schemes using the constant external wave phase speed to radiate out signals in slightly different ways. The Radiation LBC is a similar scheme used for three-dimensional calculation, which instead of the external wave phase speed, uses a locally calculated phase speed and considers signals approaching in two dimensions (meridional and zonal). The additional treatment of signals approaching from non-normal directions improves the scheme drastically (wiki ROMS, 2019).

Chapter 3

Methods

3.1 An idealized model of the slope north of Iceland

There are many advantages to utilizing idealized models in process-oriented studies (Section 2.2). The missing pieces in our understanding of the NIJ are excellent candidates for such an idealized model study. In this study, I aim to employ an idealized model to elucidate key mechanisms of the NIJ by idealizing and isolating processes in the region along the north Icelandic slope. The subsequent sections give an overview of the details of the model setup and later the experimental simulations.

3.2 Setting up the model

The Regional Ocean Model System (ROMS, Version 3.8, Shchepetkin & McWilliams (2009)) was employed for the idealized simulations. ROMS has free-surface elevation ($\zeta(x,y,t)$) and terrain-following coordinates ($\sigma(x,y,z)$, Section 2.2). The horizontal grid is staggered using the Arakawa C-grid (Section 2.3) and the vertical grid is staggered for vertical variables (Section 2.2). ROMS uses split-explicit time-stepping (Section 2.3), where the momentum equations are solved by separating the slow (baroclinic) and fast (barotropic) modes, as the two modes are computed separately to reduce computational cost while retaining numerical stability (Section 2.2). I use a baroclinic time-step of three minutes, with 25 barotropic time-steps for each baroclinic time-step. The third-order upstream scheme and fourth-order Akima scheme was applied for horizontal and vertical advection (Section 2.2), respectively.

To initialize and run experiments in ROMS I needed to create five input files: a grid, an initial, a boundary, a forcing, a climatology, and a climatology nudging file. The initial file includes the initial values for the model, which includes full temperature, salinity, and velocity fields for the domain used for the calculation of the second time step. The boundary file contains the temperature, salinity, and velocity fields which at all discrete time steps are used as boundary conditions for the model. The forcing file includes the oceanographic surface properties and atmospheric forcing fields (heat

and momentum). The climatology fields include fields used for the boundary-nudging region (Section 2.2), and the climatology nudging file contains coefficients for the properties of the nudging region. Some of the considerations made in creating these files are discussed in the following sections.

Bathymetry and Grid

The region I primarily want to represent in the idealized model is the north Icelandic shelf, shelf break, slope, and the deeper basin of the Icelandic Sea (dashed orange box in Figure 3.1). I added 100 km to the east and west of the area depicted ($\sim$ 400x400 km, Figure 3.1), which is consistent with the $\sim$600 km long North Icelandic Shelf. The Icelandic Basin is located northeast of the slope, while the Kolbeinsey Ridge, protruding out from about the center of the North Icelandic Shelf, separates the deeper Icelandic Basin from the narrow basin adjacent to the Eastern Greenland Shelf.
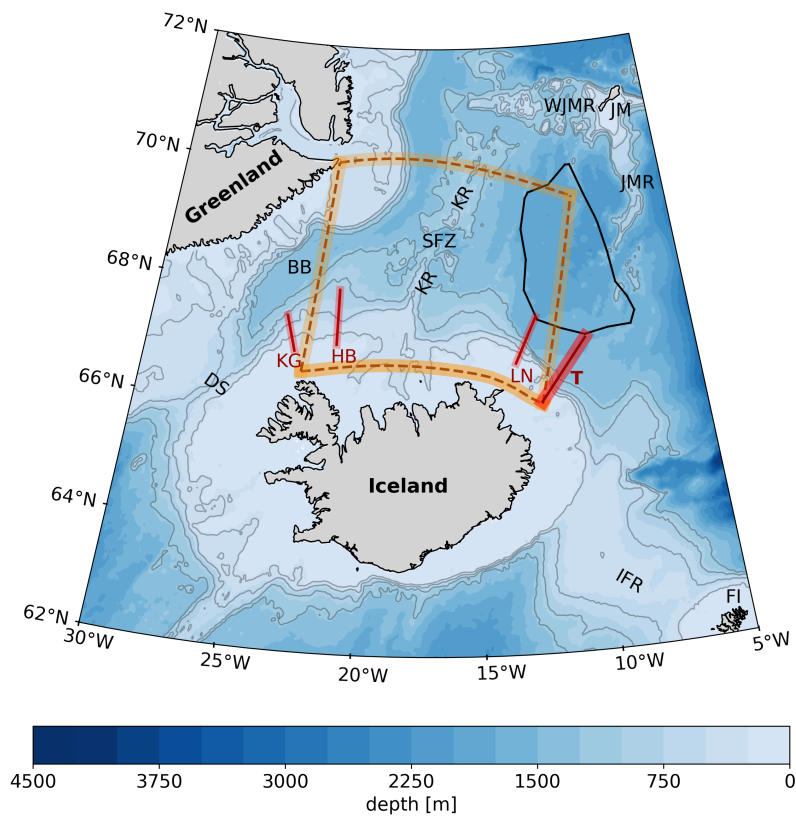

Figure 3.1: Map showing geographical features in the Iceland Sea, the location of the three hydrographic sections used throughout the study (red lines), the location of the transect of bathymetry used for the model slope (T), and the approximate area covered in the model (dashed orange box). The acronyms of the geographical features are DS, Denmark Strait; BB, Bloseville Basin; KR, Kolbeinsey Ridge; SFZ, Spar Fracture Zone; WJMR, West Jan Mayen Ridge; JM, Jan Mayen; JMR, Jan Mayen Ridge; IFR, Iceland Faroe Ridge; and FI, Faroe Islands. The acronyms of the hydrographic sections are KG, Kögur; HB, Hornbanki; and LN, Langanes Northeast. The black polygon in the Iceland Sea indicates the extent of the Iceland Sea Gyre defined by the dynamic height contour (Våge et al., 2013). The colored shading is bathymetry from ETOPO1 (Amante & Eakins, 2009) with the 300, 600, 900, and 1200 m isobaths highlighted in gray.

The idealized model will first ignore all geographical complexity and simply include a zonally constant shelf, the slope region, and the deeper basin. Thus, the model domain does not portray the whole meridional extent of the Iceland Sea Basin, however, the dynamics in proximity of the slope are those of importance in the study. In reality, the north Icelandic slope varies substantially in steepness and even includes the continuation of the Mid-Atlantic Ridge (i.e., the Kolbeinsey Ridge).

Several aspects of the circulation near the northern slope of Iceland are sensitive to the steepness (Pickart et al., 2017; Semper et al., 2022). I, therefore, constructed two constant along-channel slopes (Figures 3.2 and 3.3) of different steepness. The steep slope is meant to simulate the northeastern region of the north Icelandic slope (Transect T, Figure 3.1), while the moderate slope is meant to represent the region west of the Langanes Northeast section (Figure 3.1). Additionally, to simulate the along-slope variation in steepness, I also constructed a configuration with a steep slope in the east and the moderate slope in the west (VarSlo). In practice, this was done by applying the moderate and (meridionally shifted) steep slopes in the western and eastern half of the domain, respectively, with a smooth transition between them.
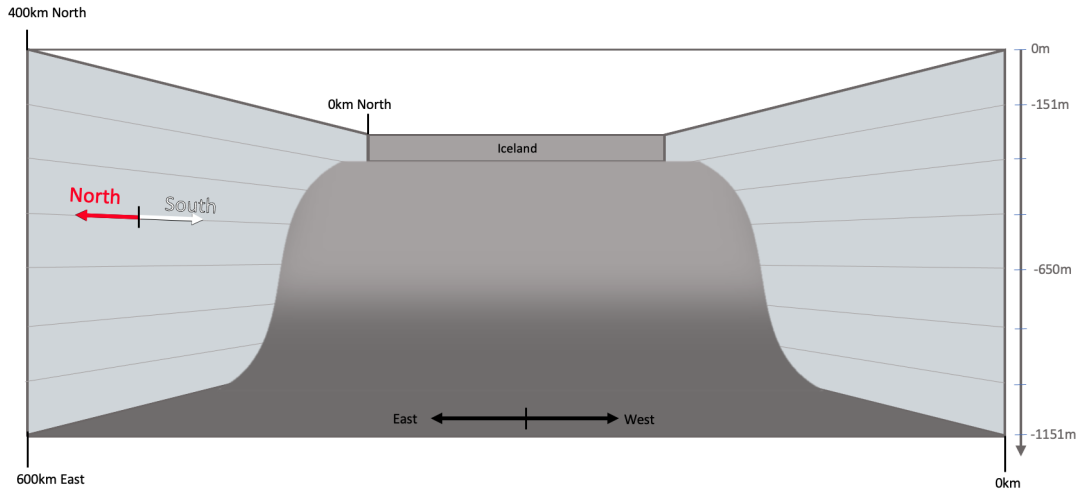
Figure 3.2: Schematic of model-domain and the idealized constant along-channel slope, meant to represent the north Icelandic slope. The orientation of the figure is from the north looking south as indicated by the arrows. The horizontal and vertical dimensions of the domain are
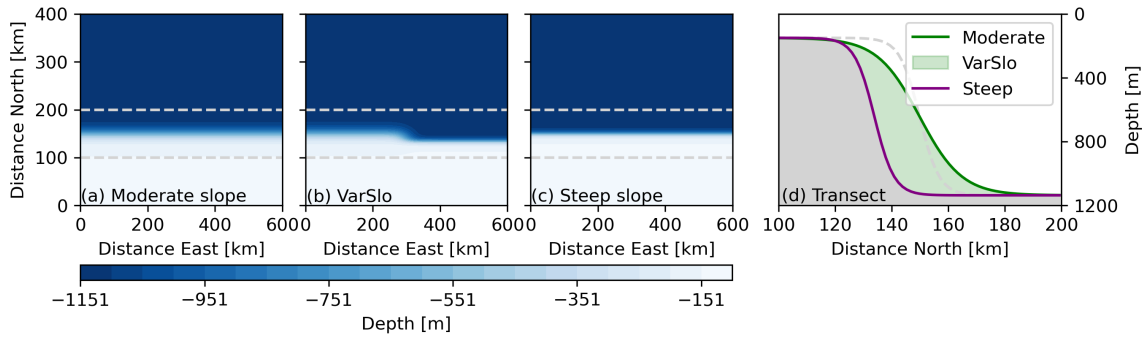

Figure 3.3: Model bathymetry in the Moderate (a), VarSlo (b), and steep slope (c) configurations and transect across the slopes (d) from the region indicated with gray dashed lines in a,b, and c. The gray dashed line in d indicates the actual constant steep-slope configuration location.

The σ-coordinates are discretized into 30 layers. The transformation used for the vertical coordinate is given by a stretching function (Shchepetkin & McWilliams, 2005) which gives higher vertical resolution near the surface and the bottom. The layers vary between 0.2 m and 10.0 m on the shelf, and 1.7 m and 76.4 m in the deep basin (Figure 3.4).

The constant along-channel idealized slopes, based on bathymetry data, were constructed with a trigonometric function (Equation 3.2)

$$h(y) = d_v + A \cdot tanh\left(\frac{R \cdot y + d_h}{S}\right) \tag{3.1}$$

$$= -651 - 500 \cdot tanh\left(\frac{1.5 \cdot y - 150}{S}\right) \tag{3.2}$$

where $h(y)$ is the meridional depth array, d_v is the vertical displacement of the slope, A is the amplitude (or vertical extent) of the slope, R is the horizontal resolution, S is the slope steepness, and d_h is the horizontal displacement of the slope from Iceland
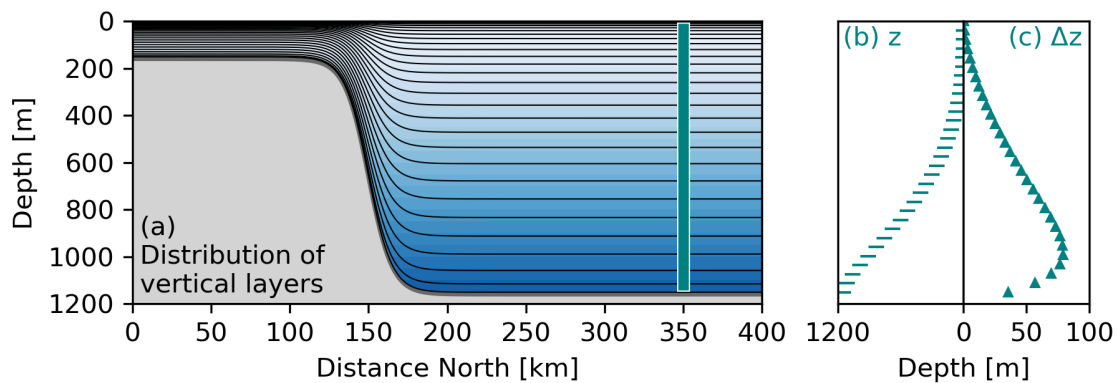
Figure 3.4: Vertical transect showing the distribution of the 30 σ-levels at different depths in the domain (a), profiles of the vertical position of layers (b), and layer height (c) at 350 km north (as indicated by the vertical line).

(Figure 3.5). Note that the slope steepness is the only parameter that changes in the constant slope configuration (S = 7 for the steep slope and S = 15 for the moderate slope), while the horizontal displacement is modified in the varying slope configuration. Additionally, the properties outside of the trigonometric function, vertical displacement and amplitude, have the unit of meter, while those inside the function, resolution, and horizontal displacement, are given in kilometers. The magnitude and sign of the slope steepness is a physically arbitrary value that fits the real bathymetry.

Due to the Icelandic slope being zonally varying and complex, I had to make some simplifications to apply Equation 3.1. I chose a transect from the steepest region of the north Icelandic slope, namely the region east of the Langanes Northeast array (T, Figure 3.1). The depth of the current and the water masses involved are mainly situated between the surface and a depth of 800 m. Thus, I concluded that accurately portraying the upper 1000 m was sufficient.

Initial hydrography

I constructed two main configurations of stratification for the model: (1) a highly idealized, horizontally homogeneous configuration (Horizontally constant) and (2) a more realistic horizontally varying configuration (IdealTransect). The former was based on 1980-2019 winter averages of temperature and salinity from all available data in the Iceland Sea Gyre (Brakstad et al., 2023a,b), defined by the relative dynamic height of the surface (as indicated in Figure 3.1, Våge et al., 2013). I then smoothed and applied the profiles at the appropriate depth, uniformly across the whole domain. These full fields of temperature and salinity (Figure 3.6) were then used as initial conditions for the horizontally homogeneous stratification model runs.

The IdealTransect hydrography is based on mean transects from the northwest (the Kögur section, KG, in Figure 3.1) and the northeast (the Langanes Northeast section, LN, in Figure 3.1) of Iceland (Semper et al., 2019a,b). The averages are compiled from 9 (Langanes Northeast) and 10 (Kögur) summer and winter surveys between 2004 and 2018, as part of the expanded dataset (Semper et al., 2019b) of repeat CTD stations
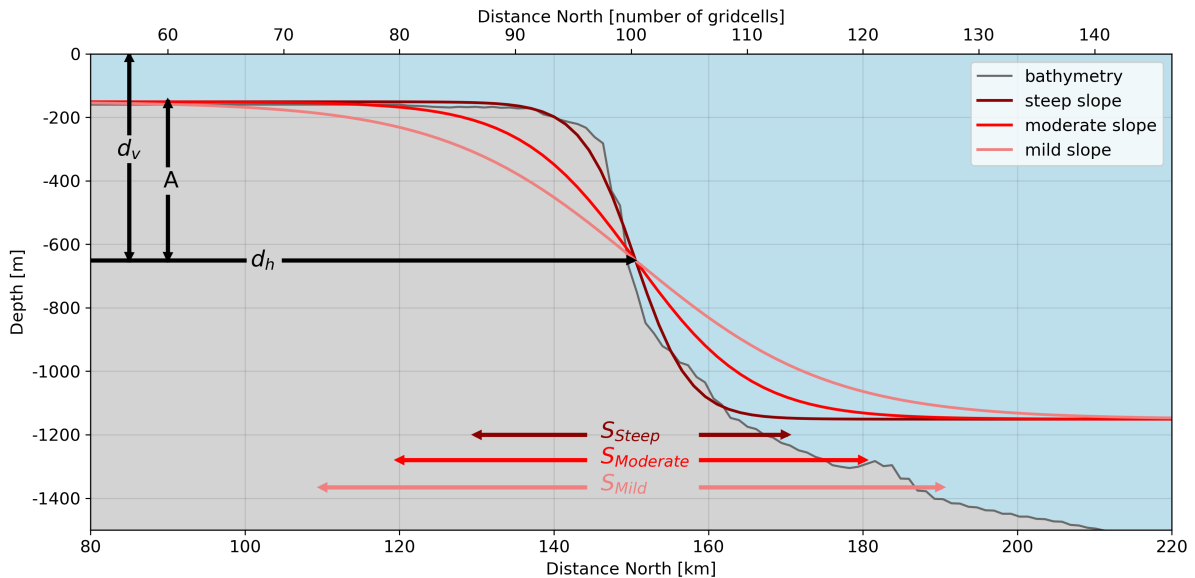
Figure 3.5: Schematic of terms in the slope function (Equation 3.1), bathymetry from the transect T (Figure 3.1, using ETOPO1, Amante & Eakins, 2009), and the two model slopes (the mild-slope configuration was later discarded). Note that the S_{Steep} and $S_{Moderate}$ indicate the meridional extent of the slopes, as this is inversely proportional to the magnitude of the S term (Equation 3.1). The acronyms are: d_v, vertical displacement; A, Amplitude; d_h, horizontal displacement; S_{slope}, slope steepness.

carried out by the Marine and Freshwater Research Institute of Iceland (MFRI, Semper et al., 2019a). Additionally, velocity from the Kögur section and the Hornbanki section (HB in Figure 3.1, Semper et al., 2019b) were used to compare with the model simulations. For consistency, I name the configuration of the hydrography for the whole domain IdealTransect, while the individual transects applied to the east (based on Langanes Northeast) and west (based on Kögur) are referred to as IT-East and IT-Eest, respectively. These two transects were chosen specifically as they exhibit the most central features on the western and eastern limits of the north Icelandic slope. These features include the presence of diverging isopycnals away from the shelf break associated with the NIJ (Sections 1.1 and 2.1), warm and saline water masses on the shelf carried by the NIIC, and cold and dense water masses being pushed upward toward the slope associated with the NIJ (Section 1.1). Additionally, the differences between the two sections depict central features of the zonal evolution of the water masses. Namely, the signal of warm and saline water masses being weaker in the east than in the west, due to the eastward cooling and mixing of the NIIC, and the presence and absence of the NIJ in the west and east, respectively (Section 1.1)

I made idealized adaptations of the observed transects, with IT-East (Figure 3.7e-g) constructed on the steep-slope configuration and IT-West (Figure 3.7a-c) constructed on the moderate-slope configuration. I carefully included the most central aspects of each transect. Other aspects of the observed transects were intentionally omitted to reduce the complexity of the profiles and to represent the larger-scale circulation better. The aspects I chose to neglect when constructing IT-West were the Icelandic Coastal Current and the sepEGC, as both are inconsequential to the aims of this study. Simi-
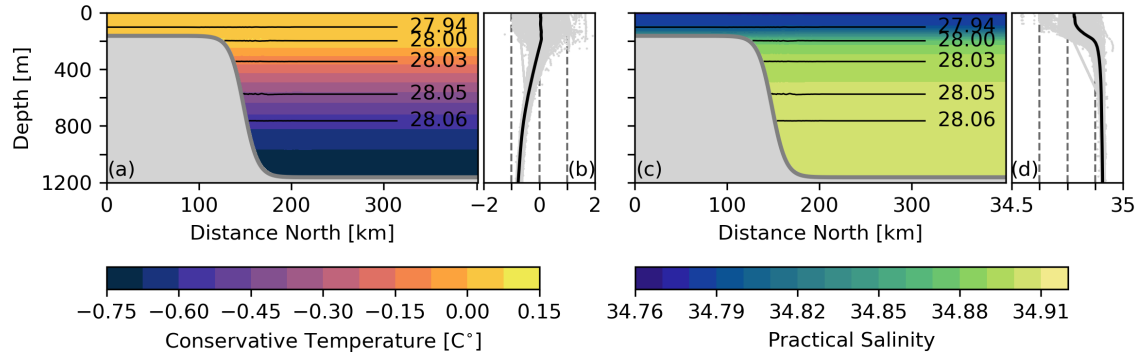
Figure 3.6: *Transect of temperature (a,b) and salinity (c,d) used as initial conditions for the horizontally homogeneous model runs and the profiles (gray) averaged to make a single profile (black) for the transects.*
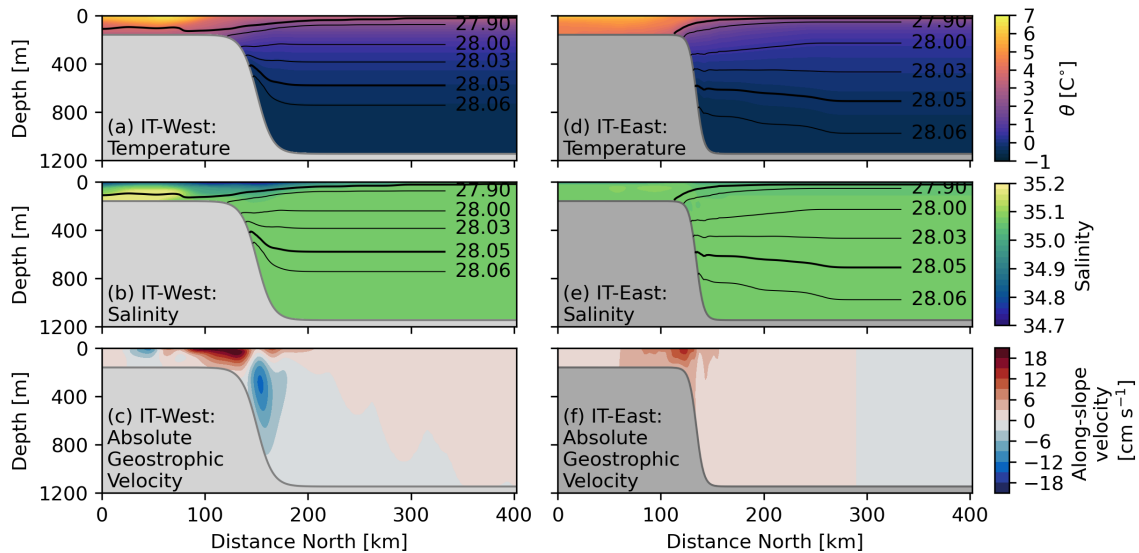

Figure 3.7: *Transects of temperature (a,d), salinity (b,e), and along-slope, absolute geostrophic velocity (c,f) for the IdealTransects configurations in the west (IT-West, a-c) and east (IT-East, d-f).*

larly, in IT-East, I removed the NIJ and the Icelandic Coastal Current. The omission of the NIJ from IT-East is perhaps the most important one, as I do not wish to force the model also to include the NIJ on the eastern boundary.

I then calculated the relative geostrophic velocities associated with the stratification of the IT-East and IT-West transects, before calculating the absolute geostrophic velocities using the appropriate bottom velocities (Figure 3.7d,h). I then converted the stratification and absolute geostrophic velocities to σ-coordinates and applied them to the correct half of the model. The central domain was simply filtered between the IT-East and IT-West fields, as the initial conditions are not periodically forced in the interior (away from the 25.5 km boundary-nudging region), and are not crucial for long spin-up periods. I then used IdealTransects, along with the corresponding absolute geostrophic

velocities, as initial conditions, boundary conditions, climatology, and surface forcing for new reference simulations.

Boundary Conditions

I use closed boundaries in the south and north, and open boundaries in the east and west. I did not implement cyclic boundary conditions, as the main objective of the model configuration is to simulate the emergence of the NIJ within the model domain. The boundary is closed in the south as this boundary is meant to represent Iceland. To simplify the model domain further, the northern boundary was also kept closed, as my primary focus is on the along-slope circulation. The eastern and western boundary conditions were kept open, to prescribe eastward and westward currents on the boundaries, as well as letting currents and signals created within the domain flow or propagate out of the domain. The composition of LBCs (Section 2.2) I used on the eastern and western boundaries were ultimately determined by what schemes best handled these in and outflows (Table 3.1).

Table 3.1: The configuration of boundary conditions used in all model runs. Note that the northern and southern boundaries are closed.

Variable	Dimensions	Cross-slope LBCs: East and West
free-surface	2D	Chapman Explicit
$\overline{U}$ and $\overline{V}$	2D	Shchepetkin
U and V	3D	Radiating-Nudging
TKE	3D	closed
Temperature	3D	Radiating-Nudging
Salinity	3D	Radiating-Nudging

The LBC used for the three-dimensional momentum equation and the advection of temperature and salinity (Table 3.1), named Radiating-Nudging (Section 3.2), allows for the control of what enters the domain through the boundary conditions, as well as allowing outgoing signals to radiate out of the domain, by a locally calculated, two-dimensional phase speed (Section 3.2). The LBC used for the free-surface (Chapman Explicit) and two-dimensional momentum (Shchepetkin) are the slightly less complex, horizontal versions of the three-dimensional Radiating-Nudging LBC.

The nudging-region on all boundaries extends 25.5 km (17 grid cells) into the domain. In this region, inflowing signals are forced to approach the predetermined exterior value (the boundary condition). The nudging in this region becomes weaker approaching the boundary. Additionally, this region has enhanced modeled viscosity and diffusivity (sponge-region) to filter out high-frequency noise associated with open boundary conditions and propagating signals along the closed boundaries.

3.3   Initialization

I ran all configurations of slopes and stratification with a spin-up time of 10 years. This was primarily done to assess if the configuration was stable, exhibited low errors, and generally to study if the configuration was appropriate for the purposes of the experiments. For instance, if the spin-up exhibited erroneous velocities on the order magnitude of the circulation north of Iceland, a more stable configuration would have to be designed, either by smoothing the stratification or bathymetry. I then ran the new experiments with the appropriate spin-up as initial conditions for temperature, salinity, and velocity. In addition to spin-ups, these simulations were also used as references (REF) for the experiments, to determine the relative contribution of numerical error.

3.4   Experiments

The experimental structure was designed to study the mechanisms needed for a NIJ-like current to materialize, and if it did, to study the impact of these and other mechanisms. Thus, I elected to iteratively withhold or add complexity within the model, to isolate and quantify these mechanisms. Consequently, several configurations were simulated (Table 3.2 and Figure 3.8).
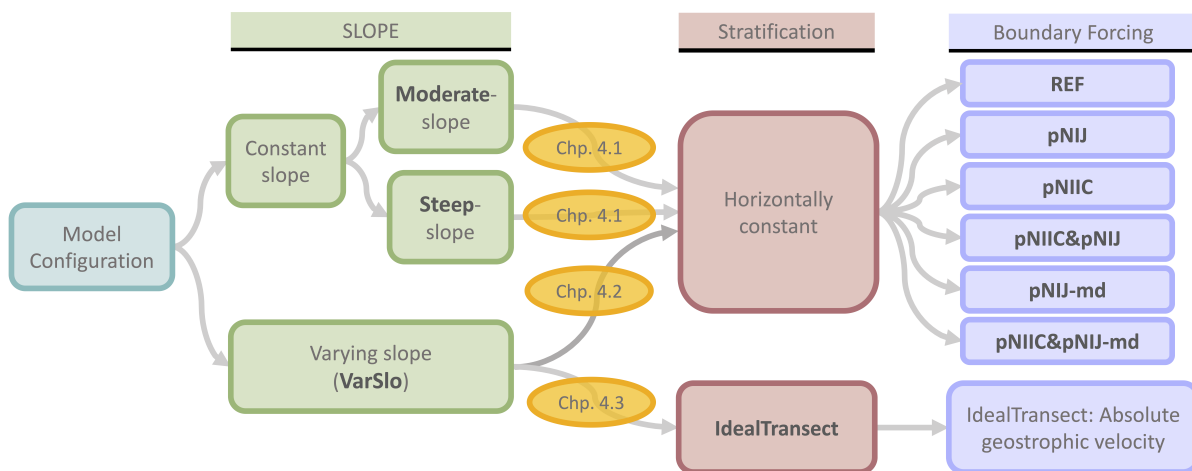

Figure 3.8: Flow-chart of model configurations found in Table 3.2. As the chart indicates, every model configuration comprises a unique combination of slope, stratification, and boundary forcing. The bold entries indicate the names of each configuration (e.g., Moderate-pNIJ and VarSlo-IdealTransect). The yellow ellipses indicate the section of the result chapter where each configuration group is introduced. Note that the VarSlo configuration does not feature the pNIJ-md and pNIIC&pNIJ-md boundary forcings (Table 3.2).

Reference runs

I ran all the spin-ups (REF in Table 3.2) with no external forcing for 10-year periods, using unique combinations of slope and stratification. In total, four spin-ups were simulated, the Moderate-REF, Steep-REF, VarSlo-REF, and IdealTransects. The forcing

Table 3.2: All experiments presented in the study. The entries in bold indicate added complexity at that stage. Abbreviations are REF, reference simulation; pNIJ, prescribed NIJ; pNIIC, prescribed NIIC; pNIIC&pNIJ, prescribed NIIC and prescribed NIJ; pNIJ-md, prescribed NIJ at mid-depth; pNIIC&pNIJ-md, prescribed NIIC and prescribed NIJ at mid-depth; IdealTransects, idealized transects; IT-East, Idealized Transect East; and IT-West, Idealized Transect West.

Short name	Added component	Slope	Stratification	Boundary forcing
Moderate-		Constant Moderate-slope	Horizontally constant	REF, pNIJ, pNIIC, pNIIC&pNIJ, pNIJ-md, and pNIIC&pNIJ-md
Steep-		Constant steep-slope	Horizontally constant	REF, pNIJ, pNIIC, pNIIC&pNIJ, pNIJ-md, and pNIIC&pNIJ-md
VarSlo	Variation in slope steepness	**Varying slope** (moderate-steep)	Horizontally constant	REF, pNIJ, pNIIC, and pNIIC&pNIJ
IdealTransects	more realistic stratification	Varying slope (moderate-steep)	**IdealTransects** (IT-East & IT-West)	Calculated absolute geostrophic velocity

fields, containing wind forcing, oceanographic surface fields, and heat fluxes, were set to constant values of either zero or those from the initial field. The climatology and boundary fields were set to re-enforce the initial fields periodically, that is, the hydrographic properties of the initial file and blank velocity fields. I set the surface restoring frequency to a year, to let the model stray from the initial fields. These reference simulations were used as initial conditions for all subsequent experiments in the same category. The IdealTransects configuration was only run as a spin-up (Table 3.2).

Prescribed in- and outflow experiments

The main class of experiments I ran throughout this project are those with prescribed in- and outflows on the western boundary, named Moderate-, Steep-, and VarSlo-pNIJ, -pNIIC, -pNIIC&pNIJ, -pNIJ-md, and -pNIIC&pNIJ-md (Table 3.2). The pNIJ-md and pNIIC&pNIJ-md boundary forcings were not applied to the VarSlo configuration. The prescribed in- and outflow experiments subject the model to the exact same forcings as in the spin-up (i.e., none), save for the along-slope velocities on the western boundary. The first configuration of these boundary-forced in- and outflows is the *prescribed NIJ*

(pNIJ, Figure 3.9b). This configuration features a rectangle (distorted in σ-coordinates) of constant, negative, along-slope velocities (u(pNIJ) = -10 cm s^{-1}). The area of this box was adjusted so that the volume transport of the prescribed outflow is 1.8 Sv, corresponding to the maximum volume transport of the observed NIJ (Semper et al., 2019a). Vertically, the pNIJ extends from the bottom of the slope and basin to a depth of roughly 300 m. This prescribed outflow is meant to simulate the downstream southward outflow of the NIJ through the Denmark Strait.
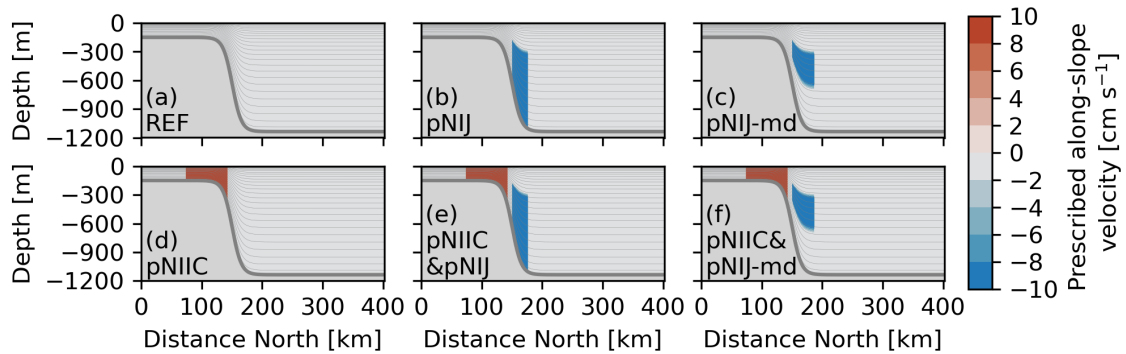

Figure 3.9: The six configurations of outflow forced on the western boundary in the REF (a), pNIJ (b), pNIJ-md (c), pNIIC (d), pNIIC&pNIJ (e), and pNIIC&pNIJ-md (f) simulations. The moderate slope is used in the illustration, but the same boundary condition was used for the steep slope simulations. All the forced outflows have speeds of ±10 cm s^{-1}. The thin gray lines indicate the vertical layers. Positive velocities are eastward.

The second configuration of prescribed current experiments, *prescribed NIIC* (pNIIC, Figure 3.9d), has a prescribed eastward inflow on the shelf of the western boundary. This inflow was also designed as a (distorted) rectangle of uniform, positive, along-slope velocities (u(pNIIC) = 10 cm s^{-1}). The pNIIC outflow covers the full depth of the shelf and the volume transport is 1.2 Sv. This current is supposed to simulate the inflow of the NIIC through the Denmark Strait.

The third configuration, *prescribed NIIC & prescribed NIJ* (pNIIC&pNIJ, 3.9e), combines the individual pNIJ and pNIIC experiments in the same boundary forcing configuration. The properties of the inflow (pNIIC) and outflow (pNIJ) are identical to the individual configurations.

The fourth configuration, *prescribed NIJ at mid-depth* (pNIJ-md, 3.9c), is a modification of the pNIJ configuration, where the outflow is restricted vertically to only account for the outflow which occurs at mid-depth (300-650 m). The speed (u(pNIJ-md) = -10 cm s^{-1}) and volume transport (1.8 Sv) are kept identical to the pNIJ experiment by extending the prescribed current horizontally. This is meant to more realistically simulate Denmark Strait, as the sill depth is about 650 m (Våge et al., 2011).

The last configuration, *prescribed NIIC & prescribed NIJ at mid-depth* (pNIIC&-pNIJ-md, Figure 3.9f), combines the outflow of the pNIJ-md and inflow of the pNIIC configurations, similarly to the pNIIC&pNIJ configuration. The properties of the individual configurations are again identical in this configuration.

To prescribe these in- and outflows, I needed to make small changes to the boundary, climatology, and climate nudging files. In the boundary file, previously zero for all velocities on all boundaries (Figure 3.9a), I added a rectangle of uniform positive or negative along-slope velocities as detailed previously. In the climatology file, responsible for how the Nudging component of the Radiation-Nudging LBC behaves (Section 3.2), I extended the vertical and across-slope rectangle of each boundary forcing eastward into the domain. The along-slope dimension of the box (out- or inflow box × along-slope distance) is 25.5 km (i.e. the boundary-nudging zone). Lastly, in the climatology nudging file, the nudging coefficients (responsible for the strength of nudging in the nudging zone) in the region associated with the box in the climatology field were magnified, to make sure the model was forced to create and maintain the current within this nudging zone.

IdealTransect

In the IdealTransects configuration, the spin-up run was the only experiment. This spin-up featured all of the previously detailed fields, including the eastern and western transects split between the two domains and applied as boundary forcings and climatology, and the calculated absolute geostrophic velocity fields being used as boundary conditions for velocity on their respective boundary (Figure 3.7).

3.5   Kinetic energy calculation

Mean kinetic energy (MKE) and eddy kinetic energy (EKE) *per unit mass* can be expressed by

$$MKE = \frac{1}{2}(\bar{u}^2 + \bar{v}^2) \tag{3.3a}$$

$$EKE = \frac{1}{2}(u'^2 + v'^2) \tag{3.3b}$$

where $u = \bar{u} + u'$ and $v = \bar{v} + v'$ is the partitioning of the mean ($\bar{u}$ and $\bar{v}$) and eddy (u' and v') components of a velocity field. I calculated MKE and EKE using model data to study the stability and EKE growth in a smaller set of configurations. In my calculations of EKE (Equation 3.3b) I used three months of daily velocity output from the model to compute $\bar{u}$, $\bar{v}$, u', and v'. The daily EKE field was then averaged over the whole period to get a mean EKE estimate:

$$\overline{EKE}_{i,j} = \frac{1}{2N} \sum_{n=0}^{N} (u'^2_{n,i,j} + v'^2_{n,i,j}) \tag{3.4a}$$

where i and j are the horizontal indices, n is the temporal index, and N is 90 days.

Chapter 4

Results

I have simulated several numerical experiments with increasing complexity regarding model slope, boundary forcing, and stratification. The results are divided into three sections, reflecting these different configurations: (1) experiments with horizontally homogeneous stratification and constant along-channel slope (Section 4.1), (2) experiments with horizontally homogeneous stratification and varying along-channel slope (VarSlo, Section 4.2), and (3) experiments with horizontally heterogeneous stratification and varying along-channel slope (IdealTransects, Section 4.3). The configurations are made with a combination of the two variants of stratification (Section 3.2), the horizontally homogeneous and heterogeneous, and three variants of the along-channel slope (Section 3.2), the constant moderate and steep, and the varying slope. This structure is designed to iteratively study the model's response to the boundary conditions, changes to the slope, and stratification, starting with only the presence of a simple slope, and working toward more complex configurations.

4.1 Horizontally homogeneous stratification and constant along-channel slope

The approach in the first set of experiments involves applying different boundary conditions to the western boundary, replicating an idealized Denmark Strait while keeping the along-channel slope and stratification as simple as possible. The main focus will be on how the horizontal and vertical current structure responds to modifications to slope-steepness and western boundary conditions, and what experiments produce more realistic simulations. This section also gives further insight into the degree of complexity needed to reproduce different observed features near the slope north of Iceland.

Reference run

Two reference simulations, the Moderate-REF and Steep-REF, were simulated with no changes to the western boundary condition (Section 3.4). These simulations are therefore used to indicate how stable the model configuration is, and whether the set-up is suitable for the purposes of the study. Furthermore, the simulations are also used

as references and spin-ups for experiments with the same configuration of stratification and slopes, respectively. Due to no external or internal forcing, I would expect quiescent simulations with no changes to the hydrography. However, all numerical models exhibit some degree of discretization and numerical errors resulting in changes to the hydrography and circulation, which with terrain-following coordinates manifest near sloping bathymetry (Section 2.3). Quantifying these errors is vital to evaluate the model's performance and errors properly, and later compare when studying simulations with forcing. In these first simulations, I find the model set-up to be appropriate for the purposes of this study and adequately, even excessively, stable.

Vertical structure

The impact of errors associated with the discretization and terrain-following coordinates are apparent in the REF simulations' hydrography and along-slope currents (Figure 4.1). As expected, these errors are largely concentrated near the sloping terrain in the two REF simulations (Figure 4.1). Both the hydrographic modifications and associated along-slope currents are weak. In the temperature, salinity, and density fields of both simulations, the most apparent feature is the weak down-tilt toward the slope in the shallower region and slight offshore migration of the coldest water masses at depth (Figure 4.1). This down-tilt is especially pronounced at, and directly inshore of, the shelf break.
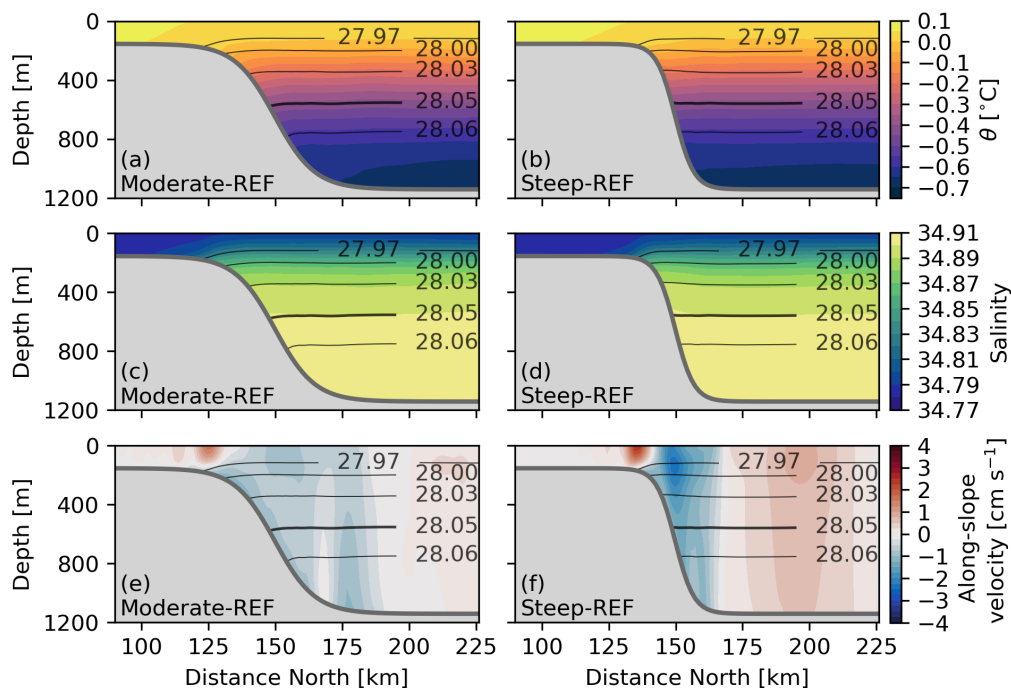

Figure 4.1: Transects of the region near the slope showing the temperature (a-b), salinity (c-d), and along-slope velocity (e-f) in shading and density in contours, from the two Moderate-REF (left) and Steep-REF (right) simulations. Positive velocities are eastward. Each panel shows a zonal mean transect of 50 km (300 km east ±25 km), as indicated in Figure 4.2, from the average of the last six months of the simulations.

The hydrographic down-tilt is associated with the along-slope currents, westward

offshore of the shelf break, and eastward inshore of the shelf break, which differs substantially between the two simulations. The along-slope velocities are weak (< 2 cm s^{-1}) near the slope in the moderate-REF simulation (Figure 4.1e), and no distinct westward current emerges. By contrast, two slightly stronger along-slope currents, with more pronounced cores, emerge in the Steep-REF simulation (Figure 4.1f). The westward current is surface-intensified and occupies the entire meridional extent of the slope. The eastward current is of comparable strength, but, confined to a small region on the shelf.

Horizontal circulation

The depth-integrated horizontal circulation illustrates the relatively low velocities in the basin and near the slope in both REF simulations (Figure 4.2). A distinct circulation pattern occurs near the boundaries in both simulations (Figure 4.2), as the volume-conserving eastern and western boundaries produce compensating currents for the in- and out-flowing along-slope currents. The compensating northeastward flows have relatively large meridional components, which dictate the circulation in the deeper basin. This also helps explain the comparable magnitudes in flow speeds throughout the basin, as the along-slope currents and basin circulation are interdependent.
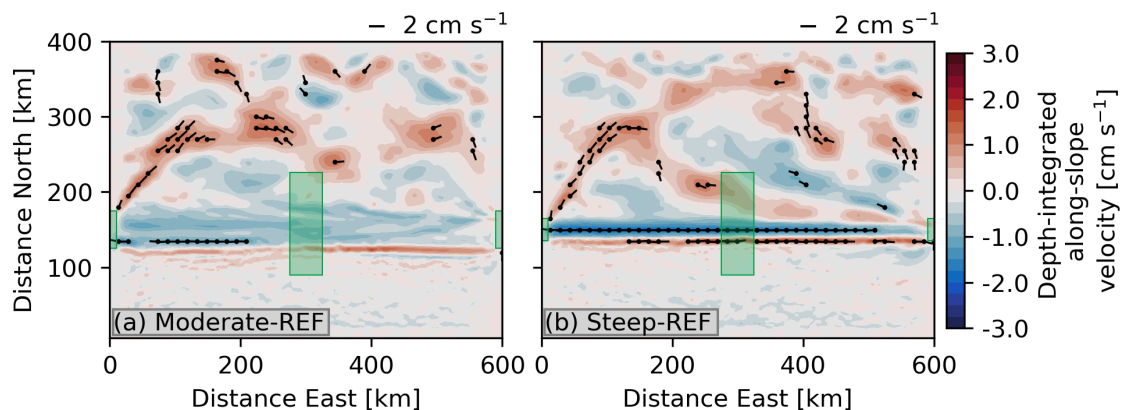

Figure 4.2: Depth-integrated along-slope velocity (shading) and depth-integrated horizontal velocities (arrows) averaged over the last six months of the simulations for the Moderate-REF (a) and Steep-REF (b) simulations. The meridional position and extent of the given slope are indicated by the green boxes on the left- and right-hand side of each panel. The green box in the center of the domain displays the location and extent of the mean section shown in (Figure 4.1). Arrows indicating depth-integrated velocities below 1 cm s^{-1} are not shown. Positive velocities are eastward.

The maximum speeds are 3.5 and 4.2 cm s^{-1} for the Moderate-REF and Steep-REF simulations, respectively. This is consistent with what is expected, as a steeper slope should produce larger internal pressure gradient (IPG) errors due to the terrain-following coordinates (Section 2.3). Due to the absence of other forcings, the REF simulations represent the numerically induced errors associated with the sloping bathymetry. I can therefore conclude that the simulated structures (Figure 4.1) demonstrate the inherent hydrographic tendencies of the model configuration. Additionally, the simulated velocities indicate the velocity range associated with these errors. Thus,

only simulations that exhibit fundamentally modified hydrographic features and are well outside the aforementioned velocity range are considered moving forward.

The fairly weak, erroneous hydrographic changes and low velocities suggest that the current model configuration is sufficient for the purposes of this study. The circulation north of Iceland primarily consists of currents with average speeds of roughly 10 cm s^{-1}, and with maximum speeds of over 20 cm s^{-1} (Semper et al., 2019a), which greatly exceeds the magnitude of these error-induced background currents.

Numerical stability

A crucial condition for a spin-up is that the model reaches a steady state, and a more fundamental stability condition is whether the model adheres to the CFL (Courant Friedrichs Lewy) condition (Section 2.2). The former condition is met in both REF simulations, as the mean kinetic energy per unit mass of the model stabilizes after about the eighth year of simulations (Figure 4.3a,b).
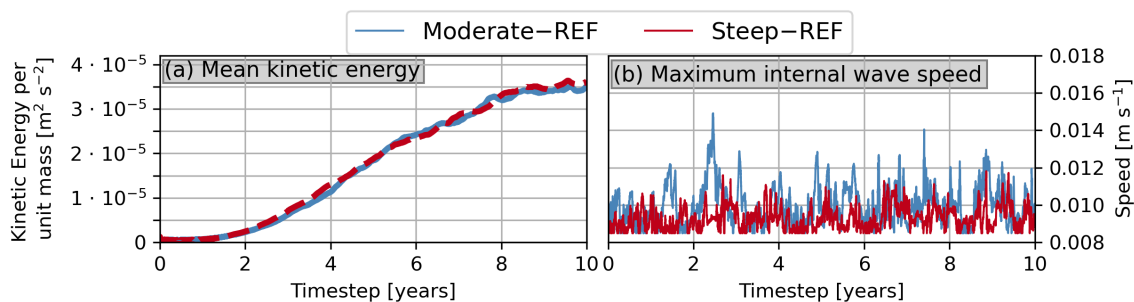

Figure 4.3: Evolution of mean kinetic energy per unit mass (a) and maximum internal wave speed (b) in the moderate- and steep-slope configurations throughout the 10-year reference simulations.

The numerical stability properties (detailed in Section 2.3), including the barotropic (fast mode) and baroclinic (slow mode) advective properties, and internal wave speeds are excessively stable. The maximum group speed of external waves, the (constant) barotropic mode, is 0.72 m s^{-1}. The internal wave speed (Figure 4.3b) has a maximum of roughly 0.015 m s^{-1} and the horizontal advection Courant numbers are consistently below 0.0012. Thus, the model configuration has an unnecessarily high computational cost, relative to what it could be when optimized for cost-effectiveness. This means that I could increase the baroclinic time-step, the horizontal resolution, or the complexity of the bathymetry considerably without compromising the stability of the model. However, the present configuration gives a considerable margin for the horizontal advection Courant numbers when later introducing less numerically stable situations. Furthermore, due to the relatively low cost of running the model as is, optimizing the configuration further can be equally time-consuming.

Prescribed North Icelandic Jet

The first experiment, also simulated with both the moderate- and steep-slope, includes a westward current prescribed on the western boundary, intended to simulate an idealized version of the NIJ, named prescribed NIJ (pNIJ, Section 3.4). This forces the model to respond to a prescribed outflow reminiscent of the downstream overflow of the NIJ through Denmark Strait. Three fundamental attributes of the NIJ are reproduced in this initial, highly idealized configuration of experiments: the mid-depth intensification of the westward current, the associated diverging isopycnals away from the slope, and the dense core and characteristic density class distribution of the volume transport of NIJ.

Vertical structure

The Moderate-pNIJ and Steep-pNIJ experiments differ substantially from the REF simulations in hydrography and the structure of the along-slope currents (Figure 4.4). While the westward current simulated in the Moderate-pNIJ experiment (Figure 4.4g) substantially exceeds the range of the numerical error seen in the REF simulations, the westward current in the Steep-pNIJ experiment (Figure 4.4h) only slightly exceeds this range. The current structure in both experiments indicates the presence of two separate cores, although this is more discernible in the moderate-slope simulation (Figure 4.4g). The outer, upper core of the westward current is to some extent reminiscent of the background flow seen in the Steep-REF simulation (Figure 4.4j).

The eastward current is present offshore of the shelf break on the upper slope in both simulations (Figure 4.4g,h), and has a slightly more mid-depth intensified core in the Steep-pNIJ simulation compared to the Moderate-pNIJ simulation. Although differing in along-slope velocity, the along-slope currents exhibit similar structures between the simulations. However, this idealized configuration of slopes might not be conducive to large structural differences when the forcing is identical.

On the lower slope, cold and dense water is pushed up-slope in both simulations (Figure 4.4a,b,e,f), associated with the up-tilted isopycnals toward the slope at depth. Simultaneously, a warming and freshening, associated with down-tilting isopycnals, occurs on the upper slope (Figure 4.4a-f). The combination of the oppositely tilted isopycnals near the slope at depth and aloft is a distinct divergence of isopycnals away from the slope. This divergence is inherently connected to the mid-depth intensification of the simulated westward current through the thermal wind balance (Section 2.1).
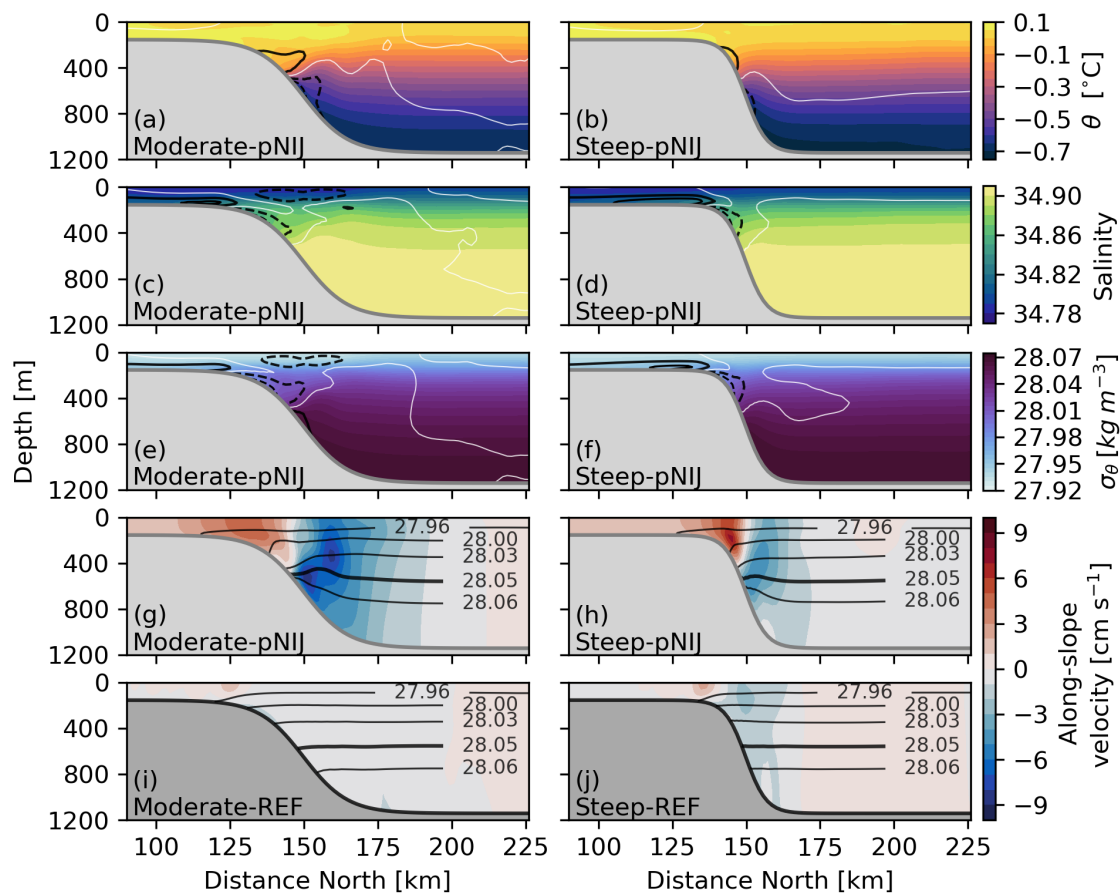
Figure 4.4: Temperature (a,b), salinity (c,d), density (e,f), and along-slope velocity (g,h) for the Moderate-pNIJ (left) and Steep-pNIJ (right) simulations. Also shown are the along-slope velocities from the two REF simulations (i,j). The contours in the upper three panels show anomalies relative to the corresponding reference simulations (pNIJ - REF), where the white contours represent the zero anomaly and the black continuous/dashed contours represent positive/negative anomalies, respectively. For temperature, the contours are given every 0.1 °C, for salinity every 0.01, and for density every 0.01 kg m^{-3}. Each panel shows zonal mean transects of 50 km (300 km east $\pm$25 km, as illustrated in Figure 4.2) from the average of the last six months of the simulations. Positive velocities are eastward.

Comparison with observations

Several features in the Moderate-pNIJ and Steep-pNIJ experiments resemble observations (Figure 4.5) at Hornbanki and Kögur (HB and KG in Figure 3.1). The structural similarities between the observations (Figure 4.5a,c) and simulations (Figure 4.5b,d) include the mid-depth-intensification of the NIJ (westward current), the divergence of isopycnals away from the slope, and the surface intensification of the NIIC (eastward current). However, the additional core (Figure 4.5b) and vertically extended core (Figure 4.5d) in the Moderate-pNIJ and Steep-pNIJ simulations, respectively, are not present in these observations (Figure 4.5a,c). Additionally, the eastward and westward currents are much weaker than those observed (Figure 4.5a,c).
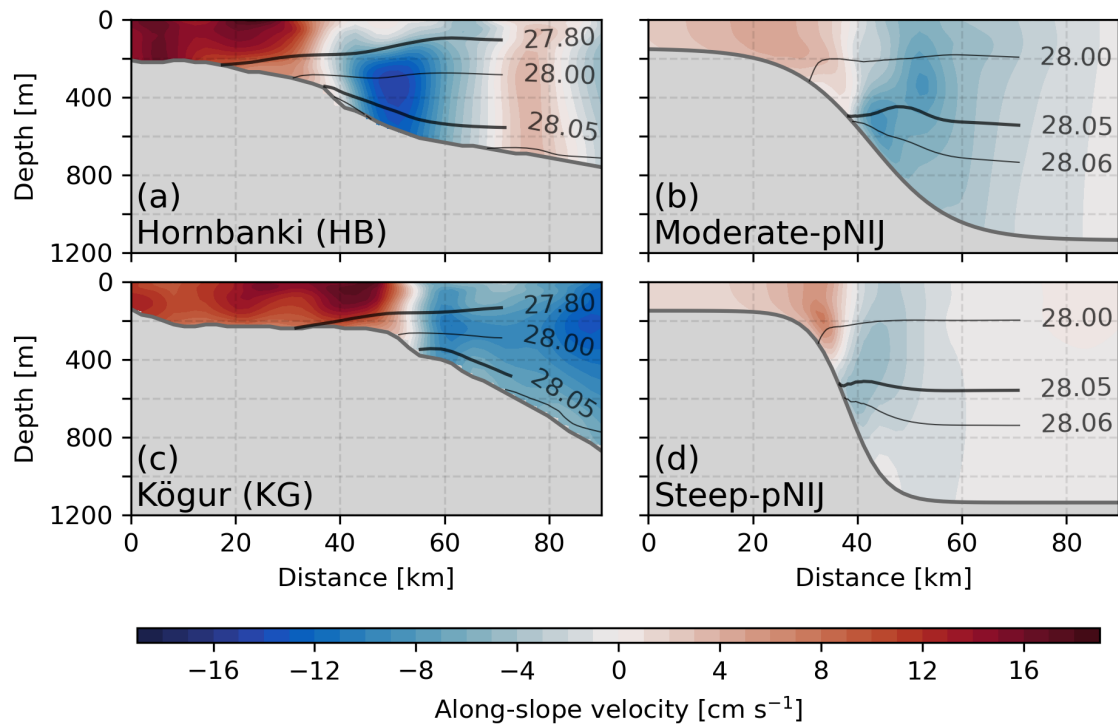
Figure 4.5: Along-slope velocity (shading) and density (contours) from observed sections, Hornbanki (a) and Kögur (c) (location shown in Figure 3.1, Semper et al., 2019a,b), and from the simulated Moderate-pNIJ (b) and Steep-pNIJ (d) experiments. The simulated fields show a zonal mean transect of 50 km (300 km east ±25 km, as illustrated in Figure 4.2) from the average of the last six months of the simulations. Positive velocities are eastward.

The structure of the eastward current is not considerably improved from the REF simulations, as the simulated eastward current was already surface intensified. However, its migration down the slope, in concert with the offshore shift of the westward current, indicates a modification by the now more realistic westward current. Since the eastward current is not yet intentionally prescribed, and is a product of either the numerical error or induced by the volume-conserving component of the western boundary, which must to some extent balance the prescribed NIJ, the current is not initially expected to be comparable to the NIIC.

Horizontal circulation

The double-core structure in the westward current is not constant along the slope, as the meridional location and strength of the westward current vary in both the moderate- and steep-slope pNIJ experiments (Figure 4.6). In the Moderate-pNIJ simulation (Figure 4.6a,c), the variable meridional location of the westward current is caused by the two westward cores co-existing in the eastern half of the domain, before they merge at approximately 300 km east. The merging of the two cores manifests as a southward shift of a single westward core in the depth-integrated fields (Figure 4.6c). Thus, both cores are persistent throughout the domain, although the inner core has a more gradual increase in strength from the eastern boundary.
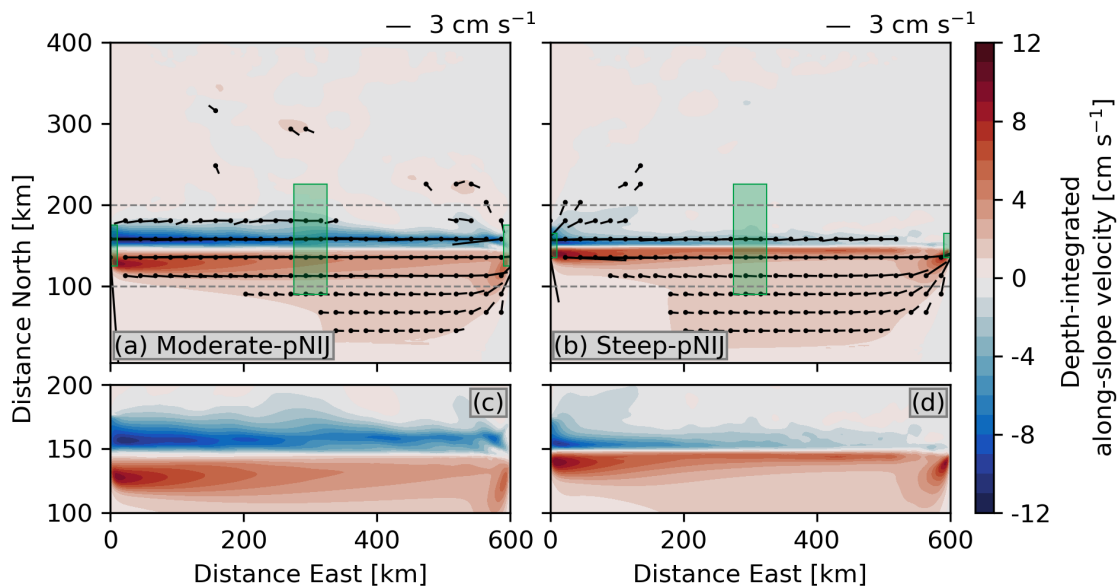
Figure 4.6: Depth-integrated zonal velocity (shading) and depth-integrated horizontal veloc-ities (arrows) averaged over the last six months of the simulations for the Moderate-pNIJ (a) and Steep-pNIJ (b) simulations. Panels c and d show a close-up of the depth-integrated zonal velocities around the slope, as indicated by the gray dashed lines in a and b. In a and b, the meridional position and extent of the slope are indicated by the green boxes on the left- and right-hand side of each panel. The green box in the center of the domain displays the location and extent of the mean section shown in Figure 4.1. Arrows indicating depth-integrated veloc-ities below 1 cm s^{-1} are not shown. Positive velocities are eastward.

In the Steep-pNIJ simulation (Figure 4.6b,d), the upper core of the current is not per-sistent upstream (east), where only a weak, mid-depth intensified, inner core is present. Downstream (west), this core is supplied with additional water masses from the north, contributing mainly to the emerging upper core. Approaching the western boundary, where the westward flow is restricted to outflow at a rate of 1.8 Sv, the westward cur-rent increases in cross-sectional area and velocity, and an additional contribution is also made by an accelerating southwestward drift.

In the Moderate-pNIJ and Steep-pNIJ simulations, the eastward current accelerates and turns northward when approaching the eastern boundary (Figure 4.5). This is pos-sibly caused by the volume conservation of the boundary not being able to compensate for the relatively large volume transport, resulting in a considerable portion of the east-ward current flowing northward along the eastern boundary (not shown).

Volume transport

The NIJ is an important contributor of dense water masses to Denmark Strait (Section 1.1). Aspects of this dense transport are captured in the simulations (Figure 4.7). While the simulated water masses are denser than the observed, the structure of the volume transport by density class near the boundary (Figure 4.7a) resembles the observations reasonably well. The general structure of the transports is quite comparable, with an exponential increase toward the respective transport modes (Section 1.1) of the cur-

rents, and a sharp decline thereafter. The general structure, and specifically the dense transport mode, is a result of the current core being mid-depth intensified and denser water masses being located on the upper slope, which is consistent with what is seen at Hornbanki (Figure 4.5 and 4.7).
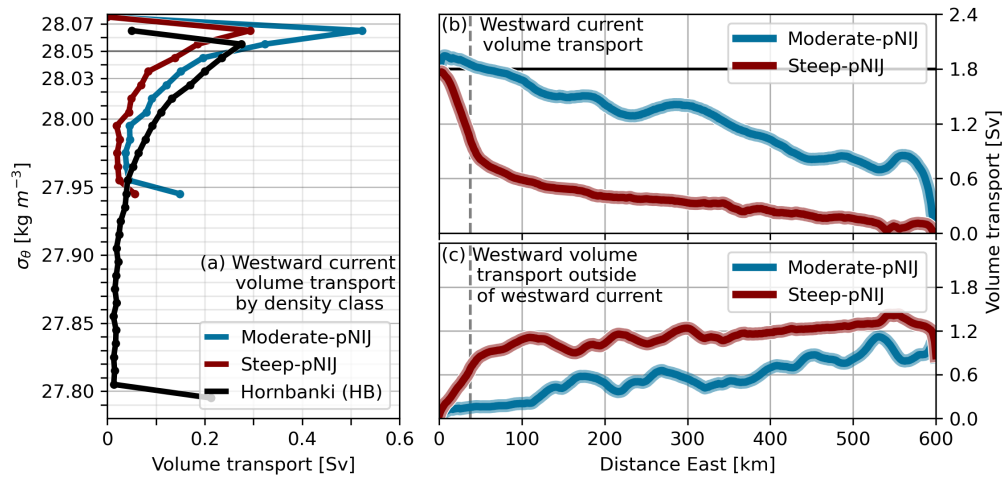

Figure 4.7: Volume transport by density class in the observed NIJ at Hornbanki (HB in Figure 3.1) and in the westward current near the western boundary (indicated by the dashed gray line in b,c) in the Moderate-pNIJ and Steep-pNIJ simulations (a), and zonal evolution of volume transport (thick line) in the westward current (b) and westward transport outside the current (c) in the Moderate-pNIJ and Steep-pNIJ simulations. The threshold between the volume transport in- and outside the westward current core is set to $2\ cm\ s^{-1}$ and the transport mode is defined by the density class with the largest volume transport at the indicated section (a).

In the Moderate-pNIJ simulation, the westward current already transports about half (∼0.9 Sv) of the prescribed transport (1.8 Sv) just outside the nudging-region of the eastern boundary. Approaching the western boundary, the volume transport slightly exceeds the prescribed transport (Figure 4.7b). In the Steep-pNIJ simulation, the volume transport of the current is close to zero initially, and only increases to about a third of the total prescribed transport throughout almost the entire zonal length, until about 100 km upstream of the boundary. The reason for the low volume transport is the generally low speed of the westward current, as only the core consistently exceeds the velocity threshold of $2\ cm\ s^{-1}$ for the volume transport calculation (Figure 4.7b).

The evolution of the westward volume transport below $2\ cm\ s^{-1}$ in the simulations (Figure 4.7c), reflects the contribution from the northern basin to the currents. In the Steep-pNIJ simulation, the transport north of the current is initially large (>1.2 Sv) relative to the current, before slowly decreasing westward until the drift drastically accelerates (Figure 4.6b) to supply the prescribed outflow. Conversely, in the Moderate-pNIJ simulation, the transport is relatively high in the eastern half of the domain, but, is considerably smaller than the westward current itself farther west.

Prescribed mid-depth North Icelandic Jet and North Icelandic Irminger Current Experiments

Through the remaining moderate- and steep-slope simulations, including the pNIIC, pNIIC&pNIJ, pNIJ-md, and pNIIC&pNIJ-md configurations (Section 3.4), the westward current is generally found to be sensitive to the slope steepness in terms of vertical structure, and the configuration of prescribed in- and out-flows on the western boundary in terms of strength. I note that neither the pNIIC nor the pNIJ-md configurations consistently simulate an NIJ-like current, emphasizing the importance of the structure (pNIJ-md) and presence (pNIIC) of the prescribed outflow. Although the strength and position of the eastward current's core are moderately sensitive to the presence and strength of the westward current, the more general structure and strength of the eastward current are not. The eastward current is instead relatively consistent between simulations with the same western boundary conditions, indicating that the most important sensitivity in these configurations is related to the strength of the inflow and not factors within the domain.

Vertical structure
In the bottom-reaching, Moderate- and Steep-pNIJ and Moderate- and Steep-pNIIC&pNIJ experiments (middle panels in Figure 4.8), a relatively similar westward, mid-depth intensified current is present, which is stronger and located slightly higher up in the water column in the Moderate-pNIJ and Moderate-pNIIC&pNIJ experiments compared with the Steep-pNIJ and Steep-pNIIC&pNIJ experiments. The structure of the eastward current is generally consistent between most simulations (Figure 4.8b,e,g,h,i,j,k), save for the REF and pNIJ-md configurations (Figure 4.8a,d,c,f), where it is nearly negligible. The offshore migration of the eastward current in the pNIIC&pNIJ experiments also modifies the westward current to be located farther offshore, which acts to merge the inner and outer core of the westward current (Figure 4.8h,k).

By contrast, the mid-depth prescribed NIJ experiments (pNIJ-md and pNIIC&pNIJ-md, right-hand panels in Figure 4.8) do not consistently exhibit either a westward or eastward current. The presence of both a westward and eastward current of considerable strength is only simulated in the Moderate-pNIIC&pNIJ-md experiment (Figure 4.8i), where the westward current is strongly surface-intensified. In the experiments with only a prescribed eastward current (pNIIC, Figure 4.8g,j), no westward, mid-depth intensified current is present.
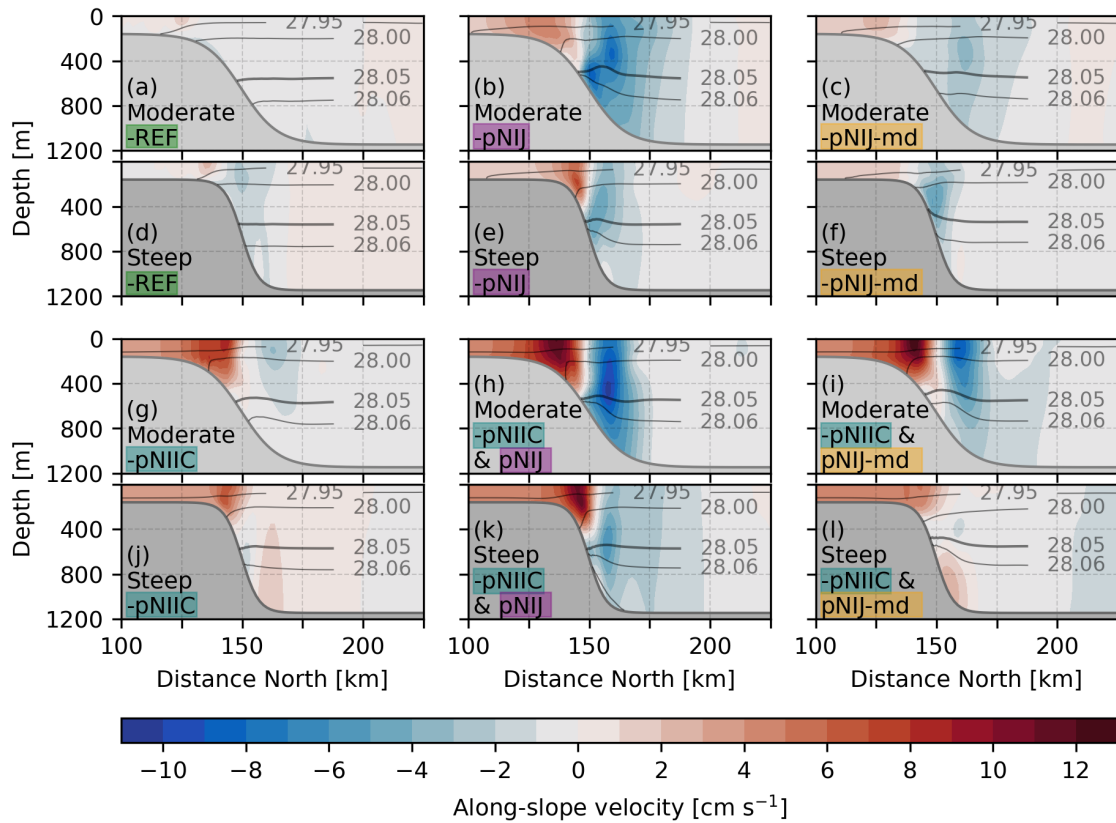
Figure 4.8: Transects of along-slope velocity in shading and density in contours for the Moderate- and Steep-REF (a,d), -pNIJ (b,e), -pNIJ-md (c,f), -pNIIC (g,j), -pNIIC&pNIJ (h,k), and -pNIIC&pNIJ-md (i,l) experiments. The fields show a zonal mean of 50 km (300 km east ±25 km), as indicated in Figure 4.9, from the average of the last six months of the simulations. The moderate- and steep-slope configurations are indicated by the light gray and dark gray slope color, respectively, and the individual prescribed currents are color-coded. Positive velocities are eastward.

Horizontal circulation

All simulations with prescribed currents at the western boundary exhibit a relatively similar eastward current (Figure 4.9). The strength of the eastward current, and especially the core located just offshore of the shelf break (Figure 4.8), is sensitive to whether it is prescribed (Figure 4.9g-l) and/or if it is adjacent to a strong westward current (Figure 4.9b,h). Moreover, the eastward evolution of the strength of the eastward current and the westward current is congruent (Figure 4.9b,h,k). The stronger core of the eastward current is generally absent east of where the westward current emerges (Figure 4.9e,k,l). The northward turning of the eastward current when approaching the eastern boundary is present in all the experiments (Figure 4.9)

The strength and presence of the westward current along the slope are less consistent in the east in the steep-slope simulations (Figure 4.9e,f,k,l), with the Steep-pNIJ and Steep-pNIJ-md experiments (Figure 4.9e,f) simply exhibiting a far weaker westward current farther east, while in the Steep-pNIIC&pNIJ (Figure 4.9k) and Steep-
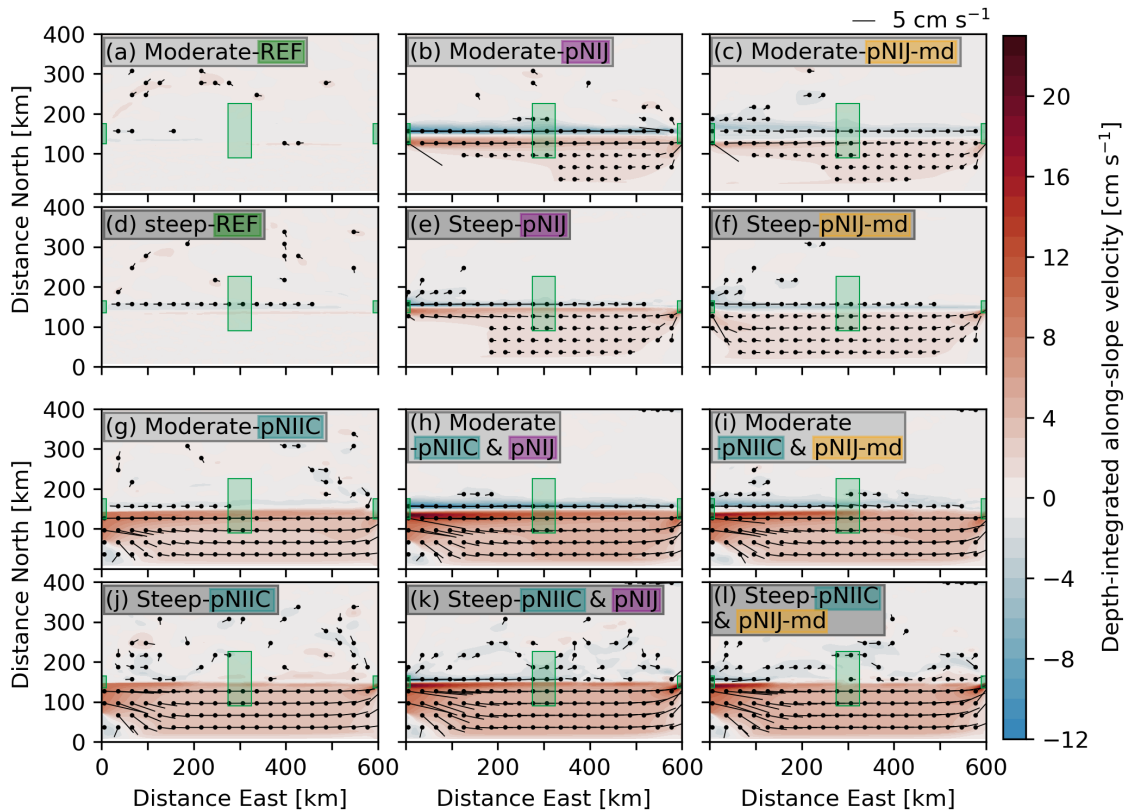
Figure 4.9: Depth-integrated along-channel velocity (shading) and depth-integrated horizontal velocity (arrows) from the last six months of the REF (a,d), pNIJ (b,e), pNIJ-md (c,f), pNIIC (g,j), pNIIC&pNIJ (h,k), and pNIIC&pNIJ-md (i,l) experiments with the moderate-slope (upper panels, a,b,c,g,h,i) and steep-slope (lower panels, d,e,f,j,k,l) configurations. The Moderate- and steep-slope configurations are indicated by the light gray and dark gray slope color, respectively, and the individual prescribed currents are color-coded. The meridional position and extent of the slope are indicated by the green boxes on the left- and right-hand sides of each panel. The green box in the center of the domain displays the location and extent of the mean section shown in Figure 4.8. Arrows indicating depth-integrated velocities below 1 cm s[1] are not shown. Positive velocities are eastward.

pNIIC&pNIJ-md (Figure 4.9l) being absent east of roughly 300 km and 100 km east, respectively. The emergence of the westward current in the Steep-pNIIC&pNIJ (Figure 4.9k) and the generally higher variability seen in the steep-slope simulations (Figure 4.9k,l) is noteworthy.

Volume transport

The volume transports of the simulated westward current are generally consistent between experiments of the same slope steepness. In contrast, the transport of the eastward current is mainly determined by whether it is prescribed. The volume transports by density class are generally consistent between simulations, although the steep-slope simulations are more sensitive to how the westward current is prescribed. In the moderate-slope experiments, the evolution of the volume transport of the westward current is roughly comparable, with similar amounts of growth in the interior domain (i.e.

outside of the boundary nudging-region). However, the mid-depth prescribed NIJ experiments (Moderate-pNIJ-md and Moderate-pNIIC&pNIJ-md) experiments have generally lower transports (Figure 4.10a).
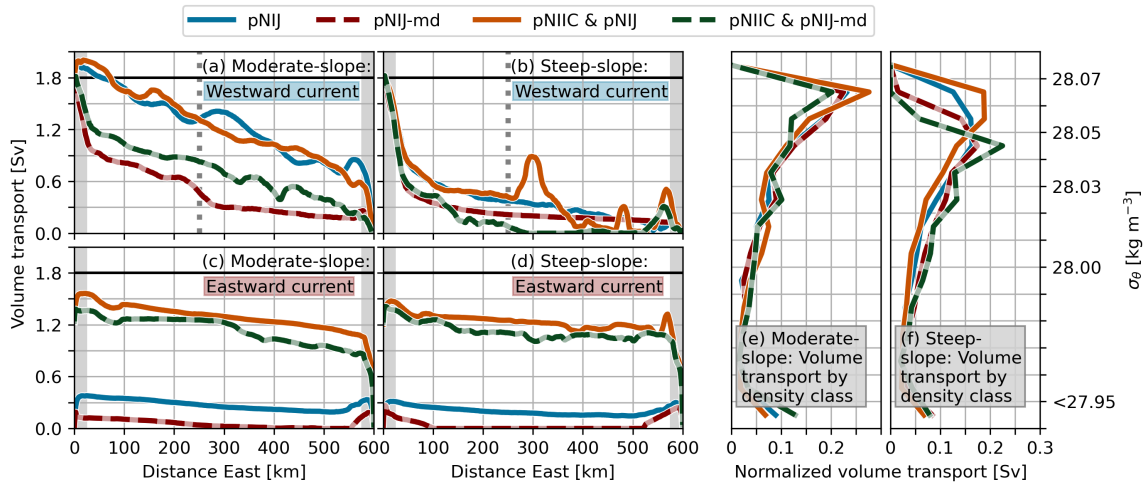

Figure 4.10: Along-channel evolution of volume transport from the last six months of simulations in the westward and eastward current in the Moderate- (a and c) and Steep- (b and d) pNIJ, pNIJ-md, pNIIC&NIJ, and pNIIC&NIJ-md experiments, and volume transport distribution by density class of the westward current at 250 km east (dashed line in a and b) in the moderate-slope (e) and steep-slope simulations, normalized by the total transport. The gray shading in a-d indicates the nudging region. The velocity threshold for including the westward and eastward current in the volume transport calculation is 2 cm s^{-1}.

In the steep-slope simulations, the volume transport of the westward current (Figure 4.10b) is more uniform, as they all only reach a transport of 0.6 Sv 100 km east of the western boundary. However, the westward current transport of the Steep-pNIIC&pNIJ experiment is more variable in the eastern half of the domain, and the westward current of the Steep-pNIIC&pNIJ-md experiment appears first in the western half. The westward volume transport peak around 300 km east in the Steep-pNIIC&pNIJ experiment (Figure 4.10b) is caused by a highly concentrated contribution from the north (Figure 4.9k). However, as evident from both the depth-integrated circulation (Figure 4.9k) and the volume transport (Figure 4.10b), only slightly more than a third of the highest transport remains within the current near the slope, while a more considerable portion flows northwestward.

The four prescribed eastward currents (Moderate- and Steep-pNIIC&pNIJ and Moderate- and Steep-pNIIC&pNIJ-md) are about 0.9-1.2 Sv higher than their un-prescribed counterparts (Figure 4.10c,d), which is consistent with the prescribed NIIC volume transport of 1.2 Sv. The transport then increases by about the same magnitude as the initial increase of their non-prescribed NIIC counterparts (Moderate- and Steep-pNIJ and Moderate- and Steep-pNIJ-md, Figure 4.10c,d), which in each experiment is consistent with the comparative strength of the westward current (Figure 4.10a,b). This indicates that the added transport is owed to similar mechanisms in all experiments, namely the volume conservation of the westward current. However, this added

transport is lost during the first 100 km, as both simulated eastward currents stabilize at roughly 1-1.2 Sv to the east.

The normalized volume transport distribution by density class of the westward current at 250 km east (Figure 4.10e) illustrates the continuity of the moderate-slope simulations, as the distribution near the middle of the domain is nearly identical between the simulations and similar to the distribution near the western boundary in the pNIJ experiment (Figure 4.7a). Conversely, the normalized volume transport distribution by density class of the westward current in the steep-slope simulations (Figure 4.10f) differ between each other and individually up- and downstream (Figure 4.7a). The Steep-pNIJ-md and Steep-pNIIC&pNIJ-md experiments, and to a lesser degree the Steep-pNIJ experiment, differ from the general structure seen in the other simulations (Figure 4.10e,f), and from the observed distribution (Figure 4.7a), as the bulk of the transport and the transport mode is less dense.

4.2 Horizontally homogeneous stratification and varying along-channel slope

In the moderate- and steep-slope configurations, a westward current emerged in all experiments with a prescribed NIJ, with some variations depending on the slope steepness. To explore the emergence of the westward current further, I now introduce a variation in the slope steepness (VarSlo, Section 3.4) within the model domain, transitioning from a steep slope in the east to a moderate slope in the west. The change in slope steepness resembles the most general features of the true bathymetry but is still strongly idealized.

The implementation of the VarSlo configuration reveals two aspects of the simulated westward current: First, the current structure and strength are to a certain degree uncoupled, with the strength of the current being highly sensitive to downstream (west) modifications, while the structure is mainly dependent on the local slope-steepness. Second, the stability of the simulated westward current is highly dependent on the steepness of the slope, with the steep-slope configuration being associated with a more unstable current. However, a more distinct emergence of the westward current is not simulated, as the westward current was strengthened in the eastern half of the domain and persisted to the boundary.

Similarly to the reference runs for the constant along-channel slope (Section 4.1), knowing the numerical errors associated with the model and interactions with the model slope, and now also associated with variations in the slope, is essential when later interpreting the experimental simulations (Section 2.2). However, as previously expressed, the general model configuration used throughout this study comfortably adheres to the fundamental stability criteria, which is also the case in the present slope configuration (not shown). The maximum group speed of external waves is identical (only dependent on depth, Section 2.3), and the internal wave speed and horizontal advection Courant numbers are of comparable magnitude to the constant slope configuration (Section 4.1).

Vertical structure

The transects from east and west of the slope variation, compared to those of the constant slope simulations, illustrate that the local slope-steepness is primarily impacting the current structure, while the downstream (west) modifications are responsible for the strength of the current. In the VarSlo-REF and VarSlo-pNIIC simulations, the velocity and hydrographic structures in the western (Figure 4.11b.ii,iv) and eastern (Figure 4.11c.ii,iv) half of the domain are nearly identical to the western (Figure 4.11a.ii,iv) and eastern (Figure 4.11d.ii,iv) half of the domain in corresponding the moderate- and steep-slope simulations, respectively. Moreover, in the western section of the Moderate-pNIJ and Moderate-pNIIC&pNIJ (Figure 4.11a.iii,v) and VarSlo-pNIJ and VarSlo-pNIIC&pNIJ (Figure 4.11b.iii,v) simulations, the westward current is only slightly stronger and more concentrated at mid-depth in the VarSlo than the moderate-slope configuration.

Conversely, in the eastern transect of the VarSlo-pNIJ and VarSlo-pNIIC&pNIJ experiments (Figure 4.11c.iii,v), the strength of the westward current is more comparable to the western transect (Figure 4.11b.iii,v) than its steep-slope simulation counterparts (Figure 4.11d.iii,v), although the current structure, with a more confined cross-sectional area, the core located closer to the slope, and less down-titled isopycnals, is more similar to the corresponding steep-slope simulations (Figure 4.11d.iii,v).

Both the relatively similar westward current in the western half of the Moderate-pNIJ and Moderate-pNIIC&pNIJ and VarSlo-pNIJ and VarSlo-pNIIC&pNIJ simulations (Figure 4.11a,b.iii,v), and the considerably different westward current in the eastern half of the Steep-pNIJ and Steep-pNIIC&pNIJ and VarSlo-pNIJ and VarSlo-pNIIC&pNIJ simulations (Figure 4.11c,d.iii,v), indicate that the strength of the simulated westward current is more sensitive to upstream modification than to downstream modifications. In contrast, the structure of the westward current is primarily sensitive to the steepness of the slope.
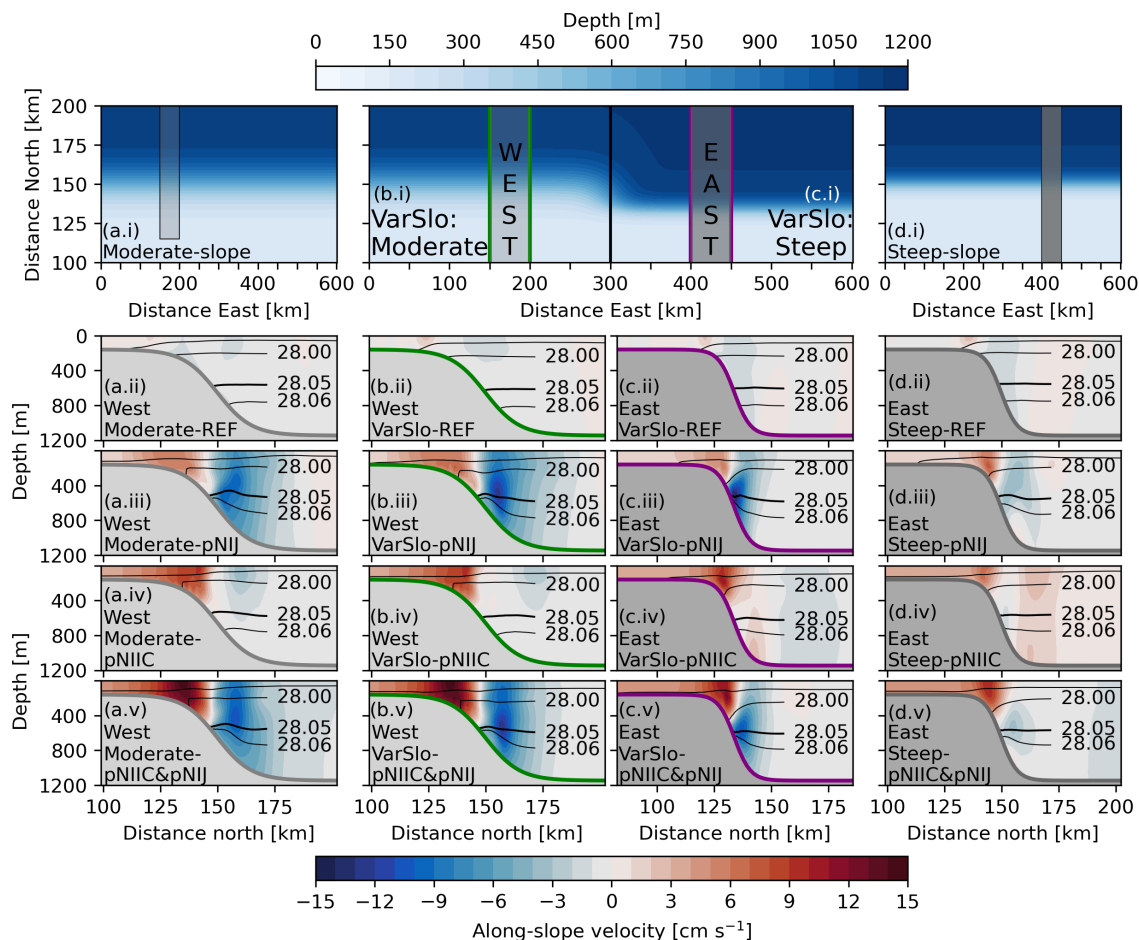
Figure 4.11: *Transects of along-slope velocity and density contours from the west of the moderate-slope (a), west of the VarSlo (b), east of the VarSlo (c), and east of the steep-slope (d) simulations of the REF (a-d.ii), pNIJ (a-d.iii), pNIIC (a-d.iv), and pNIIC&pNIJ (a-d.v) experiments. The upper panels illustrate the bathymetry and slope steepness of the constant moderate-slope (a.i), VarSlo (b.i and c.i), and steep-slope configurations. The gray rectangles in the upper panels indicate the meridional and zonal extents of the mean transects, and the color indicates the steepness of the transect. The fields show the average of the last six months of the simulations. Note that the meridional location of the steep-slope part is shifted in the VarSlo configuration relative to the steep-slope configuration. Positive velocities are eastward.*

Horizontal circulation

In the four VarSlo simulations, the general, depth-integrated circulation is relatively similar to their constant along-channel slope counterparts (Figure 4.12). The similarities include the generally low velocities in the VarSlo-REF simulation (Figure 4.12b), the zonal evolution of the eastward current in the other simulations (Figure 4.12b,c,d), with the acceleration and turning approaching the eastern boundary, and the general structure of the westward current (Figure 4.12b,c,e). The primary difference is, as one might suspect, the response of the along-slope currents to the varying slope.

The westward and eastward currents behave similarly to previous experiments in the western half of the domain in the VarSlo-pNIJ and VarSlo-pNIIC&pNIJ experi-
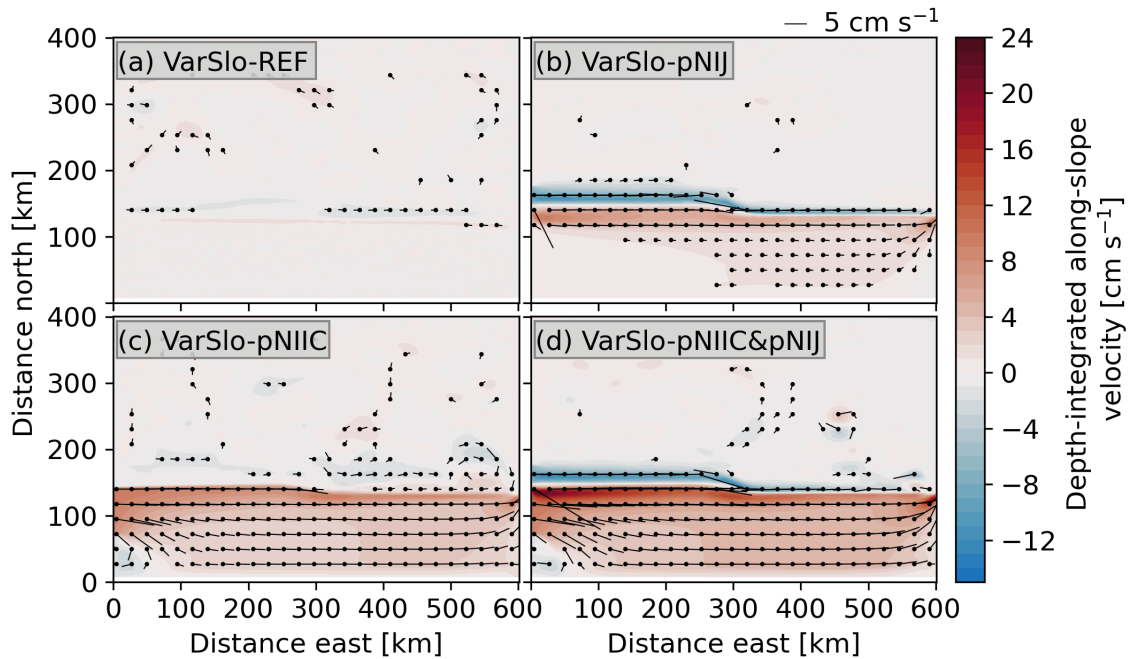
Figure 4.12: The average fields of the last six months of the simulations showing depth-integrated zonal velocity (shading) and depth-integrated horizontal velocities (arrows) within the model domain from the VarSlo-REF (a), -pNIJ (b), -pNIIC (c), and -pNIIC&pNIJ (d) simulations. Arrows indicating horizontal velocities below 1 cm s^{-1} are not shown. Positive velocities are eastward.

ments (Figure 4.12c,e), which is to be expected as the forcing is applied to the western boundary. Within the slope transition, both currents are shifted meridionally according to their respective isobaths, corresponding to the slope variation (Figure 4.12a). Furthermore, east of the variation in both simulations, the westward current is stronger than at the same longitude in the corresponding steep-slope simulation (Section 4.1). This is not the case, at least not to the same extent, for the eastward current. Additionally, in the VarSlo-pNIIC&pNIJ experiment (Figure 4.12e), a contribution from the northeast is more concentrated just downstream of the transition than in the Steep-pNIIC&pNIJ experiment (Figure 4.9).

Volume transport

The volume transport of the eastward current in the VarSlo experiments is similar to the moderate- and steep-slope simulations of corresponding forcing (Figure 4.13c,d). In the eastward current, the only sign of the varying slope is seen as a small and sharp reduction in eastward volume transport in both the VarSlo-pNIJ and -pNIIC&pNIJ experiments (Figure 4.13c,d), being otherwise very similar to the constant slope simulations. Likewise, west of the slope variation, the volume transport of the westward current in the VarSlo-pNIJ and -pNIIC&pNIJ (Figure 4.13a,b) is very similar to its moderate-slope counterpart. However, east of the variation, the westward current of the VarSlo experiments (Figure 4.13a,b) is in between the moderate- and steep-slope counterparts, with a relatively fast increase near the slope variation in the pNIJ experiment (Figure 4.13a).
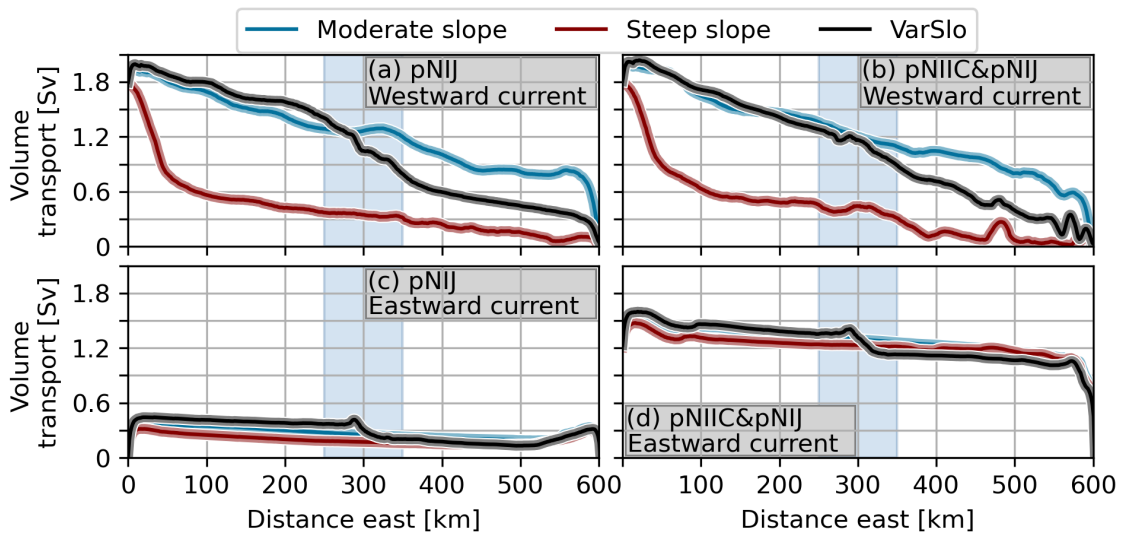
Figure 4.13: Zonal evolution of volume transport in the westward (a,b) and eastward (c,d) currents in the pNIJ (a,c) and pNIIC&pNIJ (b,d) experiments. The volume transport is calculated for the last six months of simulations, for velocities over ± 2 cm s^{-1}. The light blue box in the center indicates the zonal extent of the slope variation.

Kinetic Energy

In light of the increased variability of the westward current in the steep-slope simulations (Section 4.1 and 4.1) and the proposed connection between the emergence of the NIJ and enhanced EKE near the steepest part of the slope north of Iceland (Semper et al., 2019a, 2022), I now consider the difference in the distribution of energy (Section 3.5) between the pNIIC&pNIJ simulations for each slope (Figure 4.14). In the Moderate-pNIIC&pNIJ experiment (Figure 4.14a.i-iii), the MKE associated with the westward current is generally high ($> 10^{-2}$ m^2 s^{-2}) and increasing westward, while the EKE is more than an order of magnitude lower ($\sim 10^{-3}$ m^2 s^{-2}) and decreases westward. Additionally, the EKE immediately north of the westward current is generally low.

Conversely, the MKE and EKE associated with the westward current in the Steep-pNIIC&pNIJ simulations (Figure 4.14b.ii,iii) do not have a similarly monotonic trend. Instead, the EKE and MKE are relatively constant along the slope. However, the most apparent feature is the higher EKE ($> 10^{-3}$ m^2 s^{-2}) of the westward current and immediately north of it in the Steep-pNIIC&pNIJ simulation compared to the moderate slope. Generally, the moderate slope is associated with a relatively stable westward current, while the steep slope is associated with a more unstable westward current.

In the VarSlo-pNIIC&pNIJ simulation (Figure 4.14c.i-iii), these stability regimes are featured in their corresponding half of the domain. The relatively stable structure seen in the Moderate-pNIIC&pNIJ simulation (Figure 4.14b.ii) is represented in the western half of the VarSlo-pNIIC&pNIJ simulation. This manifests as a strong increase in MKE of the westward current toward the boundary, while the EKE decreases rapidly
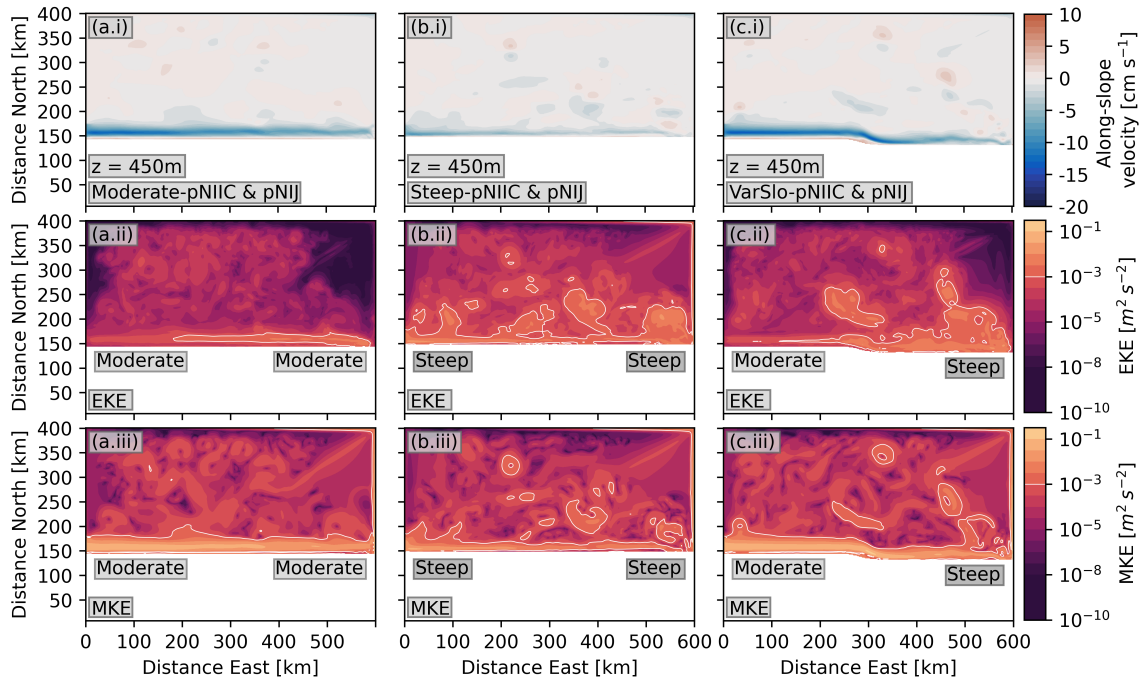
Figure 4.14: Along-slope velocity (a-c.i), EKE (a-c.ii) and MKE (a-c.iii) at a depth of 450 m from the last three months of simulations for the constant Moderate- (a) and Steep- (b), and VarSlo-pNIIC&pNIJ (c) simulations. The labels near the shelf in the EKE and MKE panels indicate the steepness of the slope in the respective half of the domain. The white contour indicates EKE and MKE exceeding $10^{-3}\ m^2\ s^{-2}$.

shortly west of the slope variation in both the westward current and the basin to the north. Similarly, the MKE associated with the current is slightly lower in the east, while the EKE of the current and the basin to the north is generally higher and the current and northern region are hardly differentiable in terms of EKE.

Moreover, although the MKE is lower in the eastern half than in the west in the VarSlo-pNIIC&pNIJ simulation (Figure 4.14c.iii), it is still generally higher than in the eastern half of the Steep-pNIIC&pNIJ simulation (Figure 4.14b.ii), which is consistent with the strengthened westward current seen in the transect comparison (Figure 4.11e). This again illustrates the considerable upstream impact of the slope variation on the westward current. The relatively high values in MKE associated with larger vortices in the domain present in all three simulations are presumably due to the relatively short time averages (three months) used for the computation.

4.3 Horizontally heterogeneous stratification and varying along-channel slope

The previous model configurations (Section 4.1 and 4.2) were simulated with highly idealized and horizontally constant hydrography from the Iceland Sea Gyre (Section

3.3). I now introduce an experiment with more realistic horizontal variations in stratification (IdealTransects, Section 3.4) but still with highly idealized smoothness and along-slope variation. Constant configurations of IT-West and IT-East, applied to the whole domain using the constant moderate- and steep-slopes, respectively, were simulated to assess the performance of the individual boundary conditions and can be found in Section B (Figure B.1). The comparison between the previous configurations and the IdealTransects illustrates that the enhanced realism of the hydrography, and velocity fields on the boundaries, has a relatively small impact on the general horizontal circulation in the model. Furthermore, the westward current at depth and the associated up-titled isopycnals are relatively unchanged, as the largest difference in density is seen near the surface. However, near the surface and the upper slope, indications of the impact of the stronger stratification are noticeable, mainly in the horizontal and, consequently, the vertical locations of the two currents.

Horizontal Circulation

The depth-integrated horizontal circulation in the VarSlo-IdealTransects simulation (Figure 4.15a) is generally very similar to the corresponding, VarSlo-pNIIC&pNIJ simulation (Figure 4.15b). Both simulations exhibit adjacent, isobath-following, comparably strong westward and eastward currents, both persistent from the eastern to the western boundaries (Figure 4.15a,b). Additionally, the strong flow south of the eastward current is present in both simulations.
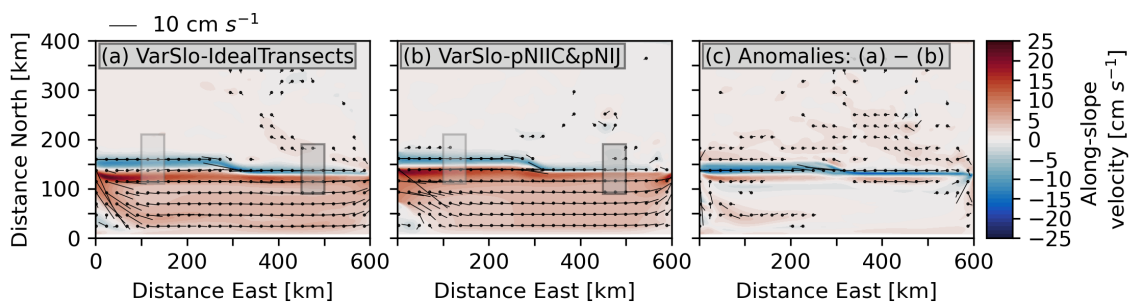

Figure 4.15: Depth-integrated along-channel velocity (shading) and depth-integrated horizontal velocity (arrows) averaged over the last six months of (a) the IdealTransects and (b) pNIIC&pNIJ VarSlo simulations, and the difference between the two (IdealTransects - pNIIC&pNIJ, c). The gray boxes indicate the horizontal location and extent of the transects in Figure 4.16. Note that the arrows in (c) illustrate the difference between (a) and (b), not actual currents. Positive velocities are eastward.

Four notable differences emerge in the VarSlo-IdealTransects simulations (Figure 4.15a,b,c). First, a relatively strong southeastward drift flows out of the domain north of the slope, which helps to feed the northernmost part of the prescribed outflow on the eastern domain. Second, the eastward current simulated in the VarSlo-IdealTransects experiment does not feature a similar northward turning and acceleration as seen in all previous experiments with a strong eastward current (Sections 4.1 and 4.2, Figure 4.15b), as the eastward current instead exits the domain on the shelf. Third, the westward current is faster and wider in the eastern half of the domain in the VarSlo-

IdealTransects simulation. Lastly, the meridional position of the eastward and west-ward currents are shifted southward (inshore) in the VarSlo-IdealTransects simulation.

Vertical structure

The reason for the southward shift of the along-slope currents of the VarSlo-IdealTransects simulations (Figure 4.15a), is that the eastward current, both west and east of the variation, is confined to the shelf and shelf break (Figure 4.16b,c.iii), instead of also occupying the upper slope (Figure 4.16a,d.iii). The westward current in the IdealTransects simulation is shifted southward and occupies the middle and upper slope.
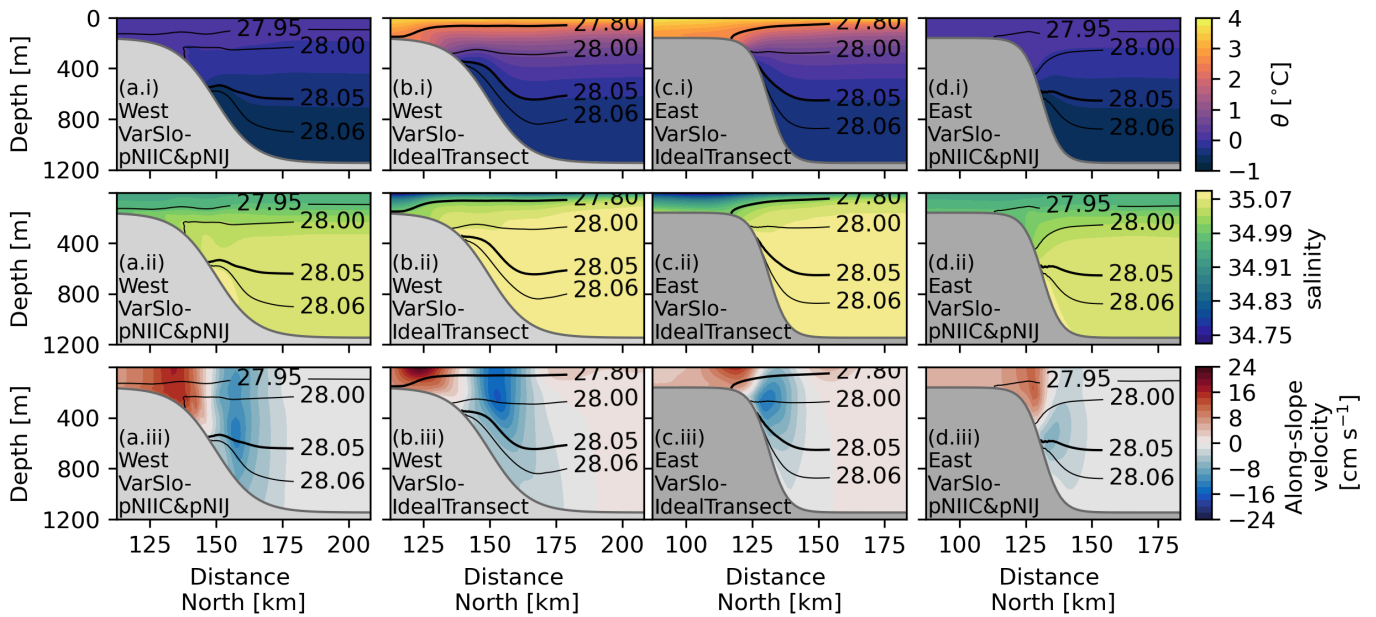

Figure 4.16: Temperature (a-d.i), salinity (a-d.ii), and along-slope velocity (a-d.iii) in shading, and density in contours for the western (left-hand side) and eastern (right-hand side) transects from the last six months of simulations for the VarSlo-IdealTransects (middle panels) and VarSlo-pNIIC&pNIJ (outer left- and right-hand side) simulations. Note that the lightest isopycnal in the IdealTransect is 27.8 kg m⁻³, not 27.95 kg m⁻³. Positive velocities are eastward.

In the VarSlo-IdealTransects simulation, the westward current at the eastern transect (Figure 4.16) is structurally very similar to previous simulations (Sections 4.1 and 4.2), despite being associated with a stronger isopycnal up-tilt at the middle of the slope and the core being positioned higher. However, its meridional position relative to the eastward current is improved, as the steep isopycnal down-tilt aloft associated with the eastward current is horizontally distinct from the more gradual down-tilt associated with the westward current. This structure resembles the previous moderate slope configurations (Section 4.1) and the observations (Figure 4.5, Semper et al., 2019a). At the western transect (Figure 4.16), the core of the westward current is located even higher, with a relatively strong surface intensified component and no discernible isopycnal down-tilt aloft.

The density at depth in the IdealTransects and horizontally homogeneous stratification simulations is comparable, due to the compensation between the higher salinity and higher temperature in the IdealTransects simulation (Figure 4.16a-h). Near the surface and on the shelf, although a large portion of the initial warm and salty water is pushed southward on the shelf (not shown), the vertical and lateral density gradients are far greater in the IdealTransects simulation. Thus, the density front between the two currents is more realistic in terms of resembling the temperature gradient between the dense overflow water and the Atlantic inflow water, as intended. This is presumably the reason for the improved cross-current structure in the eastern half, as the density gradient dynamically separates the currents.

Chapter 5

Discussion

5.1 Characteristics of the North Icelandic Jet

Mid-depth intensification and divergence of isopycnals

The vertical structure of diverging isopycnals away from the slope and the mid-depth intensified NIJ are well-documented (Jónsson & Valdimarsson, 2004; Pickart et al., 2017; Semper et al., 2019a). The isopycnal and current structure are dynamically linked through the thermal wind balance (Section 2.1, Figures 5.1 and 5.2). The idealized model captures this isopycnal divergence and mid-depth intensified current in a wide range of configurations (Sections 4.1, 4.2, and 4.3). The structure is present from the most idealized, moderate- and steep-slope prescribed NIJ (Moderate- and Steep-pNIJ) experiments (Section 4.1) to the most realistic, varying slope idealized transects (VarSlo-IdealTransect) experiment (Section 4.3). The presence of the diverging isopycnals and mid-depth intensified westward current is thus not found to be sensitive to the steepness, changes in the slope steepness, or stratification changes.

In the experiments with a westward current prescribed strictly mid-depth (pNIJ-md and pNIIC&pNIJ-md, Section 4.1), the mid-depth intensified current is more variable along the slope or entirely absent. This could support the notion that the friction between the bottom and the westward current (i.e., the bottom Ekman layer) acts to push dense water masses up-slope (90° left of the current direction on the northern hemisphere), which would maintain the up-tilted isopycnals toward the slope at depth (Jónsson & Valdimarsson, 2004; Semper et al., 2019a). Additionally, several floats deployed east of the Kolbeinsey Ridge, aimed at studying the pathway of the NIJ across the ridge, experienced considerable upward motion and thus stranded on the slope (de Jong et al., 2018). This up-slope motion is consistent with a relatively strong Ekman transport associated with a correspondingly strong, bottom-reaching NIJ.

Conversely, up-tilted isopycnals at depth persist both where the NIJ is weak (northeast of Iceland, Semper et al., 2019a) and east of its emergence, where the isopycnal

Baroclinic component:
Zonal relative
geostrophic velocity
profile

Barotropic component:
Sea surface elevation
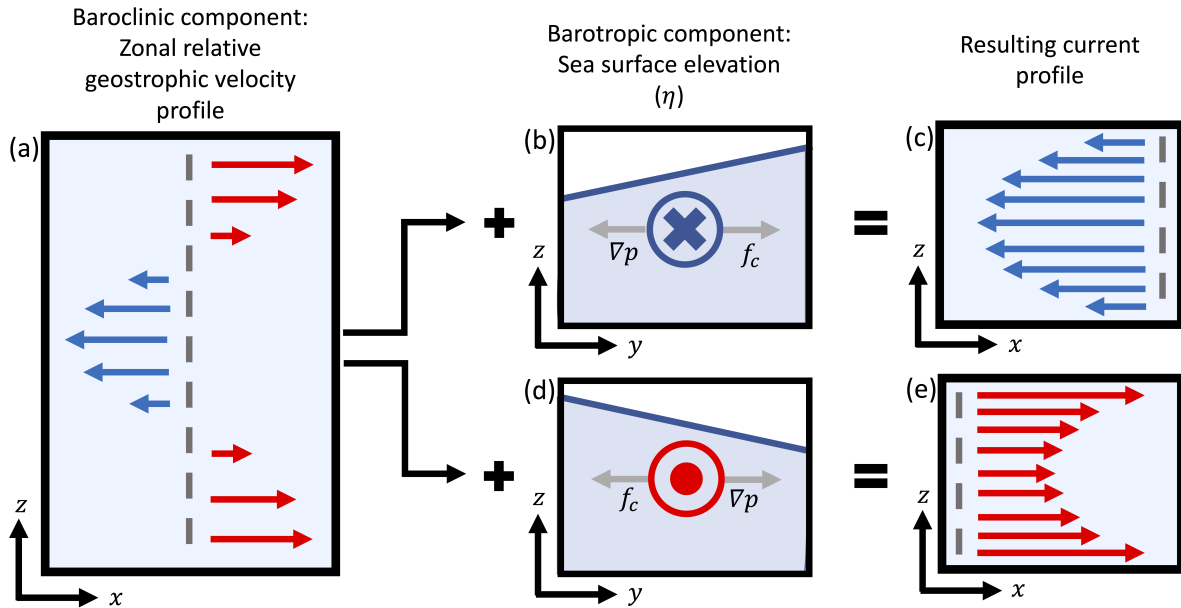(η)

Resulting current
profile

Figure 5.1: Schematic of the combined effect of the thermal wind balance (a) and sea surface elevation (b,d), which results in different vertical profiles (c,e) depending on the sea surface elevation (upper and lower panels). The relation between the vertical isopycnal structure and the relative geostrophic velocity profile is detailed in Section 2.1. The dashed gray line in the left-hand panel indicates a reference level for the relative velocities, the arrows in the right-hand panels show the change in the arrows relative to this reference level. Blue and red arrows indicate westward and eastward directions, respectively. The blue X and red colored O in the middle panels indicate movement into and out of the z-y plane, respectively. The gray arrows in the middle panels indicate the geostrophic balance. The coordinate system of each figure is indicated in the bottom-left corner; note that the middle panels (b,d) are rotated 90° relative to the other panels.
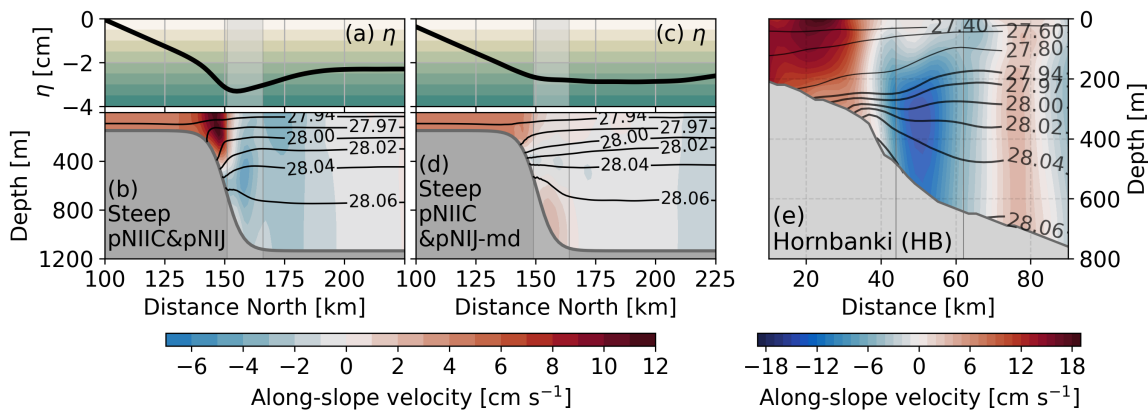
Figure 5.2: Sea surface elevation (a,c) and along-slope velocity (b,d,e) for the steep-slope pNIIC&pNIJ (a,b) and steep-slope pNIIC&pNIJ-md (c,d) experiments (Section 4.1), and observations at the Hornbanki section (e, HB in Figure 3.1). The left-hand (a,b) and right-hand (e) panels correspond to the scenario in the upper panels of Figure 5.1, while the middle panels (c,d) correspond to a weak version of the scenario in the lower panels of Figure 5.1.

tilt instead is associated with an eastward bottom-intensified current (the IFSJ, Semper et al., 2020). In these cases, the bottom Ekman transport would either be too weak

or orientated northward, such that it could not account for the isopycnal up-tilt. Moreover, in a number of my simulations where the mid-depth intensified westward current is absent, namely, the steep-slope prescribed NIIC (Steep-pNIIC) and prescribed NIIC & prescribed NIJ at mid-depth (Steep-pNIIC&pNIJ-md) simulations (Section 4.1, Figure 4.9j,l), and the eastern half of the VarSlo-pNIIC simulations (Section 4.2, Figure 4.11c.iv), the diverging isopycnals remain. Consequently, the bottom Ekman layer transport is unlikely to be responsible for the up-tilted isopycnals (Jónsson & Valdimarsson, 2004). However, as evident from the stranded floats of de Jong et al. (2018), if the relatively strong up-slope motion is indeed caused by the NIJ, the Ekman transport associated with the NIJ might act to enhance the up-tilt of the isopycnals further.

In the Steep-pNIIC and Steep-pNIIC&pNIJ-md simulations (Section 4.1, Figure 4.9j,l), and the eastern half of the VarSlo-pNIIC simulations (Section 4.2, Figure 4.11c.iv), the isopycnal divergence is instead associated with a set of surface- and bottom-intensified eastward currents, and a velocity minimum at mid-depth (Figure 4.9). This is consistent with the observed structure east of the emergence of the NIJ (then associated with the IFSJ, Semper et al., 2020) and consistent with the thermal wind balance (Figures 5.1 and 5.2).

The difference between the NIJ configuration (Figures 5.1b,c and 5.2a,b,e) and IFSJ configuration (Figures 5.1d,e and 5.2c,d) is consistent for the thermal wind theory (Figure 5.1) and the idealized simulations (Figure 5.2). In the configuration with an NIJ, the isopycnal divergence is accompanied by a sea surface tilt toward the slope (Figures 5.1b and 5.2a). This results in a westward, mid-depth ($\sim$600m) intensified current offshore of the shelf break (Figures 5.1c and 5.2b). In the configuration without an NIJ (or with an IFSJ-like current), the isopycnal divergence is accompanied instead by a sea surface tilt away from the slope (Figures 5.1d and 5.2c), which results in a bottom-intensified current on the lower slope (Figure 5.1e and 5.2d).

Since observations (Semper et al., 2019a, 2020) and my simulations demonstrate that the bottom-reaching component of the NIJ is not a necessity for the isopycnal up-tilt at depth, another explanation must account for the failure of the mid-depth prescribed NIJ (pNIJ-md and pNIIC&pNIJ-md) experiment to consistently simulate a mid-depth intensified westward current (Section 4.1). The most obvious explanation would be that the combination of boundary conditions and prescribed mid-depth current are incompatible. This is supported by the almost immediate reduction in volume transport upstream of the boundary in the pNIJ-md and pNIIC&pNIJ-md simulations (Section 4.1, Figure 4.10).

The boundary condition for density in the pNIJ-md and pNIIC&pNIJ-md configuration does not feature an isopycnal divergence which should support the mid-depth prescribed current. This could have deteriorated the structure of the current considerably before the signal could escape the boundary nudging region (Section 3.2). Although the same could be argued for the conventional pNIJ forcing, the density structure needed to maintain this current through the nudging region would not have been as drastically different from the structure of the prescribed current, especially consid-

ering the distortion of the σ-coordinates in the upper part (Section 3.4). In addition, the mid-depth prescribed current of the IdealTransect simulations persisted through the boundary nudging zone (Section 4.3, Figure 4.16). The difference between the Ideal-Transect configuration and the more idealized pNIJ-md configuration is that the density structure at the boundary in the IdealTransect simulation is consistent with the current (Figure 3.7), as the current structure consists of absolute geostrophic velocity fields calculated from the hydrography.

The NIJ's sensitivity to steepness

In the experiments where an NIJ-like current occured, the vertical structure still varied considerably between the configurations. This is consistent with observations, as the NIJ's structure is observed to vary depending on local differences in steepness and circulation (Pickart et al., 2017; Semper et al., 2019a). In the moderate-slope simulations (Sections 4.1 and 4.2), the isopycnal down-tilt aloft in the westward current is weak, in some cases nearly absent, and the westward current's core is less vertically restricted, nearly reaching the surface in several simulations (e.g., the Moderate-pNIJ and -pNIIC&pNIJ simulations, Figure 4.9). Moreover, there is a greater cross-slope distance between the two along-slope currents, and the eastward current is associated with a spatially separate down-tilt toward the slope. This last point is particularly evident in the IdealTransect simulation, where the eastward current is inshore of the shelf break (Figure 4.16).

Conversely, in the majority of the steep-slope simulations (Sections 4.1 and 4.2, Figures 4.5 and 4.11), the isopycnal down-tilt aloft is relatively strong, and the westward current's core is strictly confined to mid-depth. This is also perhaps associated with the vertical extension of the surface-intensified eastward shelf break current, which by its proximity to the westward current contributes to the down-tilt of isopycnals toward the slope. In a number of these simulations, the eastward current is located directly above the westward current (Sections 4.1, 4.1, and 4.2). In these cases, the velocity of the westward current is lower. However, there might not be a direct causality between the velocity of the westward current and the location of the eastward current.

The modeled differences in the structure of the adjacent along-slope currents are congruent with the observed impacts of slope steepness (Pickart et al., 2017), where steep regions of the north Icelandic slope bring the NIIC and NIJ together. When the currents are adjacent, they become dynamically linked, and the stronger density gradient between them, perhaps in addition to the slope steepness itself (Spall, 2004; Isachsen et al., 2012; Semper et al., 2022), acts to induce baroclinic instabilities in the currents. The combined impact of these factors: the location of the eastward current relative to the westward current, the density-gradient induced instabilities (Pickart et al., 2017), and the steepness induced instabilities (Spall, 2004; Isachsen et al., 2012; Semper et al., 2022), may provide a more complete picture of why the westward current is weaker in the steep slope simulation (Sections 4.1 and 4.2).

The proposed instabilities of the along-slope currents in the steep-slope configuration and steep part of the VarSlo configuration are supported by the enhanced EKE in the steep-slope configurations (Figure 4.14). This result is consistent with observa-

tions, as the steep northeastern slope of Iceland features enhanced EKE levels, although this is also attributed to faster eastward surface currents (Semper et al., 2022). In my simulations, the eastward shelf break current is generally of comparable speeds in the moderate- and steep-slope and VarSlo simulations when the same western boundary forcing is applied (Sections 4.1, 4.1 and 4.2), which suggests that a combination of the steepness of the slope and the associated enhanced density gradient is the determining factor for the enhanced EKE.

According to quasigeostrophic linear stability theory, a sloping bottom should suppress the growth of baroclinic instabilities (Blumsack & Gierarsch, 1972; Mechoso, 1980; Qu & Hetland, 2020). However, as illustrated for marginal seas with topographically steered boundary currents (Spall, 2004, 2011), and more specifically in the Norwegian Atlantic Current in the eastern Nordic Seas and West Greenland Current in the eastern Labrador Sea (Bracco et al., 2008; Isachsen et al., 2012), a sufficiently steep slope will counteract the suppression of instabilities by sloping bathymetry. In Isachsen et al. (2012), this is conceptually interpreted as the steep slope acting as a wall, and not as a sloping bottom, if the extent of the slope is comparable to the current. Spall (2004) explained the same effect theoretically through the ratio between the topographic and isopycnal slope steepness.

The conceptual interpretation of Isachsen et al. (2012) is consistent with the structure of the steep-slope simulation (Sections 4.1, 4.1 and 4.2), as the slope and current widths are comparable. However, this would also be the case for the moderate-slope simulations, as the ratio between current and slope width is generally comparable to the steep-slope simulations (Sections 4.1, 4.1 and 4.2). Thus, I could not relate the enhanced EKE of the steep-slope simulation with the theory or conceptual interpretation of baroclinic instability suppression. Further work, feasibly using the present model with a specialized set of configurations, is needed to study these mechanisms further (Section 5.4)

The double-core structure of the NIJ

The outer core of the NIJ is a well-documented, inconsistent feature (Pickart et al., 2017), and its nature is uncertain (Semper et al., 2019a). Nevertheless, three hypotheses have been proposed, the outer core could either be: (1) an intermittent, separate branch of the NIJ (Pickart et al., 2017; Semper et al., 2019a); (2) related to eddies or waves (Pickart et al., 2017; Semper et al., 2019a); or (3) the result of the observations not resolving the meandering of the NIJ (Semper, personal communication). As the three proposed hypotheses would generally involve complex, non-linear processes and interactions with features not included in the model, ascertaining the nature of this feature was not envisioned in this study.

However, a number of the idealized simulations exhibited an outer, weakly surface-intensified secondary core of the westward current, which to varying extents manifested as a completely separate or partly merged core (Sections 4.1, 4.1, and 4.2). This core could in many cases closely resemble the observed outer core, as its position in relation to the westward current was comparable to the observed second core of the NIJ (Semper et al., 2019a). Nevertheless, a similarly positioned current, not associated with the

stronger westward current, was first simulated in the REF simulation (Section 4.1), and later in the pNIIC experiments (Sections 4.1 and 4.2), attributed to truncation errors of the calculation of internal pressure gradients with terrain-following coordinates (Section 2.3). Thus, we cannot distinguish the persistent, outer core of the westward current in the model simulations from the currents associated with numerical errors (Section 4.1).

Impact of stratification

The simulation with a more realistic stratification (IdealTransects) exhibited subtle contrasts to those with horizontally homogeneous stratification (Section 4.3). The most considerable difference was the stronger density gradient between the modeled AW of the NIIC and the Arctic-origin water of the NIJ, which created a more pronounced meridional separation between the two currents (Figures 4.15 and 4.16). In the eastern (steep) transect of the IdealTransects simulation (Figure 4.16c.iii), the NIJ- and NIIC-like currents were still supported by the same isopycnal down-tilt aloft, indicating a stronger dynamical link, consistent with the observed NIJ and NIIC in steep regions (Pickart et al., 2017; Semper et al., 2022). Moreover, in the western (moderate) transect, the NIJ- and NIIC-like currents were separated even farther and not associated with the same isopycnal down-tilt, which is also consistent with the observed NIJ and NIIC in more moderate regions (Pickart et al., 2017). Thus, the dynamical link between the modeled NIJ and NIIC was more accurately represented than in previous simulations, where the strong density gradient was not represented.

I generally found the circulation more sensitive to the steepness than the added realism of the stratification. However, one aspect that could have contributed to this was the tendency for the AW of the NIIC-like current to be diluted and spread across the shelf (Figure 4.15), which was already noted in the simulated eastward currents of the more idealized configurations (Sections 4.1 and 4.2). This behavior could be mitigated by including a dynamical or topographic boundary in the south, such as a configuration with the fresh Icelandic Coastal Current or a more realistic bathymetry on the shelf. Moreover, other features, such as the increasing density of the NIIC as it flows eastward (Våge et al., 2011; Pickart et al., 2017; Semper et al., 2022) could have been better represented in the configuration. The time constraints did not allow for further analysis of the impact of the density gradient on stability. Further work should be done on how this impacts the stability of the currents (Section 5.4), as it is proposed as a destabilizing mechanism (Pickart et al., 2017; Semper et al., 2022).

The emergence of the North Icelandic Jet

The emergence of the NIJ is hypothesized to be associated with the enhanced instabilities of the NIIC on the northeastern Icelandic slope (Våge et al., 2011; Pickart et al., 2017; Semper et al., 2019a, 2022). The unstable NIIC generates a meridional eddy flux toward the deep basin, which must in some way be dynamically balanced. Previously, this balance has been proposed to be associated with the thermal wind balance in the along-slope currents (the NIIC and NIJ) and the lateral density gradient between the NIIC and the interior of the Iceland Sea (Våge et al., 2011). In the idealized simulations of Våge et al. (2011), the density in the interior of the Iceland Sea is approximately

uniform eastward, while the density in the NIIC increases (Semper et al., 2022). This along-slope decrease in the lateral density gradient must, by thermal wind, be balanced by a reduction in the vertical shear eastward (i.e., between the NIJ and NIIC), which would occur by a net re-organization of mass between the upper (NIIC) and lower (NIJ) current. This is consistent with the observed congruence in where the NIIC deteriorates and where the NIJ emerges (Semper et al., 2019a, 2022).

Despite the simulations presented in this study not exhibiting a similar along-slope evolution in the lateral density gradient (except for the IdealTransects simulations, Section 4.3), I replicate the enhanced instabilities, diagnosed through enhanced EKE, on the steeper part of the slope (resembling the northeastern slope north of Iceland). However, my simulations do not consistently replicate the emergence of the NIJ. This indicates that I might have omitted a central part of the emergence of the NIJ, namely the along-slope modification of the NIIC. Further work with the IdealTransects configurations might elucidate aspects of these mechanisms, as it could better represent the along-slope modifications to the simulated NIIC and the meridional density gradient between the simulated NIIC and NIJ, while still including the steeper northeast region (Section 5.4).

Nonetheless, the steep-pNIIC&pNIJ (Figure 4.9) simulation was able to reproduce the emergence of an NIJ-like current associated with enhanced EKE, which indicates that the idealized model can resolve some central processes in the region north of Iceland. This corroborates the notion of the steep northeastern Icelandic slope potentially being a critical region for the emergence of the NIJ (Våge et al., 2011; Semper et al., 2019a).

The evolution of the North Icelandic Jet

As the NIJ flows along the northern slope of Iceland, it is continuously supplied from the north by dense water masses with comparable properties to the NIJ (Semper et al., 2019a). It has been noted that the continuity of this supply of dense water to the NIJ, along with the accordance between the sill depth at Denmark Strait and the isobath the NIJ follows, might indicate that hydraulic control at the Denmark Strait sill (Nikolopoulos et al., 2003) is of importance for the NIJ upstream (Semper, 2020). Studies of hydraulic control at sea straits, such as the Denmark Strait sill, have found that the dynamics at shallow sills could act to determine the volume transport across these straits, through rotation, sill structure, flow properties, and upstream stratification (Nikolopoulos et al., 2003; Pratt, 2004; Girton et al., 2006). This has been hypothesized to impact the upstream volume transport of the NIJ, as the NIJ would, by continuity, be forced to adhere to the volume transport of Denmark Strait determined by hydraulic control (Semper, 2020). A similar notion has been proposed for the IFSJ and the FBC (Pratt, 2004; Girton et al., 2006; Semper, 2020). In this thesis, I did not focus on the theory of hydraulic control at Denmark Strait, but my simulations are consistent with the continuity aspect of the hypothesized hydraulic influence.

The evolution of the NIJ-like current in my model is consistent with observations (Semper et al., 2019a), as it features a relatively continuous increase in volume transport throughout the zonal domain (Figures 4.7, 4.10, and 4.13). However, the evolu-

tion of the current within the moderate- and steep-slope configurations differ, with the moderate-slope simulations being more consistent with observations. This added consistency comes in the form of a more continuous increase in transport, which reaches the prescribed volume transport of about 1.8 Sv near the western boundary, but still outside the boundary nudging region. This is to some extent consistent with observations, as a larger portion of the north Icelandic slope, except for the northeastern region, is moderate in terms of steepness (Semper et al., 2022).

5.2   Model configuration

Several major and minor advantages and limitations of the idealized model were evident in the simulations. The most evident strength is the deliberate low or absent complexity in all aspects, including coastlines, bathymetry, water masses, atmospheric forcing, seasonal variability, diurnal variability, and tides. By omitting these impacts, I isolated the mechanisms hypothesized to be associated with the NIJ. However, the most evident limitation was the problematic circulation associated with the boundary conditions and volume conservation.

Boundary conditions

An inherent problem with non-global ocean models are the impacts of boundary conditions (Section 2.2). In the idealized model, the most problematic example of this was the downstream pathway of the outgoing eastward current in many simulations (Sections 4.1 and 4.2). Instead of simply flowing out of the eastern boundary, the current was reflected northwards, seen as an acceleration and northward turning of the current, as it approached the eastern boundary in nearly all of the prescribed current experiments (Figures 4.6, 4.9, and 4.11). The radiating and nudging lateral boundary condition (Section 2.2, wiki ROMS, 2019) used for momentum on the eastern and western boundary (Section 3.2) should ideally allow for the current to be radiated out at a locally calculated phase speed. However, due to the restriction of volume conservation, there is a somewhat limited capacity for this current to radiate out without an equally strong current entering the domain. Although this poor treatment of the eastward current did not directly impact the westward current, as the northward flow was generally restricted to the surface layer within the nudging region, it does illustrate that a different boundary configuration could perhaps have been better equipped at treating the relatively strong along-slope currents of interest.

The IdealTransect simulation indicated instead that this could be solved with more realistic boundary forcings (i.e., currents prescribed on the boundary), as the problems with the outflowing eastward current were to some extent mitigated by the prescribed eastward current on the eastern boundary (Figure 4.15). This improvement was not replicated in the horizontally constant stratification configuration with a similarly prescribed outflow in the east, and thus not included in the study. The reason for this discrepancy is not self-evident but is presumably related to the increased realism of the boundary condition.

Another influence of the boundary conditions is the consistent emergence of an eastward current on the shelf break. The NIJ is consistently accompanied by an eastward shelf break current, even when the NIIC is located farther inshore, which is also an observed feature (Pickart et al., 2017). However, the current simulated here emerges within the nudging region, which indicates that it does not emerge from dynamical necessity (i.e., the NIJ always being accompanied by an inshore eastward current), but instead as an artifact of the volume conservation. It does show that the preferred location for an eastward compensation is just inshore of the westward current, as the volume conservation is initially meant no compensate the outflow evenly at the boundary unless a preferred pathway is found. Possible solutions to the poor treatment of out-flowing signals could be to employ a different volume-conserving regime or perhaps completely different boundary conditions. However, for the purposes of this study, they were found to be sufficient.

The deterioration of the prescribed NIJ at mid-depth (pNIJ-md and pNIIC&pNIJ-md, Section 4.1) configurations within the boundary nudging region, as well as the strongly reduced steep-slope prescribed NIJ (Steep-pNIJ and -pNIIC&pNIJ, Section 4.1), indicate that certain configurations of prescribed outflows and the boundary condition were not compatible. This could have been mitigated by applying physically consistent hydrography in the nudging-region or reducing the strength of the nudging parameters within the area where the outflow was prescribed. However, the former option would have prescribed the NIJ in a more explicit way than I initially wanted, while the latter option might have disrupted other aspects near the boundary in these exact simulations. Thus, the prescribed in- and outflow configurations (Sections 4.1 and 4.2) was adequate as a preliminary basis configuration.

5.3   Concluding remarks

Throughout this study, I have shown that this idealized model can simulate the most fundamental aspects of the NIJ and that the set-up is appropriate for the research questions posed in the introduction (Chapter 1). It is important to note that a fully realistic representation of the NIJ was not envisioned, but rather a westward current that displayed the most elementary aspects of the NIJ, such as its mid-depth intensified core and associated isopycnal divergence. The purpose of simulating such an idealized NIJ-like current was to assess the impact of features on the north Icelandic slope and test relevant hypotheses relating to the currents' emergence, evolution, and driving mechanisms. The absence of complex bathymetry, stratification, and other currents observed near the north Icelandic slope (e.g., the IFSJ, EIC, sepEGC, and the Icelandic Coastal Current) provided an opportunity to isolate the governing mechanisms, which is the very reason the idealized model was constructed for this purpose.

My first research question concerns whether the model could convincingly simulate an NIJ-like current by withdrawing dense water at the western boundary. The simulations presented throughout this thesis would advocate this, as central aspects of the NIJ were adequately captured. These aspects include the mid-depth intensification,

divergent isopycnal structure, volume transport distribution, and response to regional modifications in steepness and circulation. Specifically, using the western boundary as a prescribed downstream outflow, intended to simulate the Denmark Strait overflow plume, succeeded in introducing an NIJ-like current along the north Iceland slope. As the simulated NIJ largely emerged at the eastern boundary, additional configurations of the slope and the simulated NIIC were constructed to study the NIJ's emergence. I thus demonstrated that this can be a valuable tool to study the NIJ, associated processes, and the NIJ's emergence.

My second research question concerns how changes in the steepness of the north Icelandic slope impact the NIJ. Through my simulations, the simulated NIJ was found to be highly sensitive to the general steepness of the slope (moderate- and steep-slope) and to along-channel variations in the slope (VarSlo). The simulated NIJ and NIIC were more prone to instability, generally weaker, and more closely located when the slope was steeper. These simulated responses to changes in steepness were consistent with observed features of the circulation north of Iceland.

My third scientific question concerns how the stratification near the north Icelandic slope impacts the NIJ. Although my simulations showed an impact of the increased density gradient between the AW of the NIIC and the Arctic-origin water of the NIJ, which acted to make a more realistic front between the two currents, the general structure of the current was relatively similar to the less realistic stratification simulations. Thus, I found that the NIJ is more sensitive to the steepness of the slope than the stratification north of Iceland. However, more work is needed to study the impact of stratification on the circulation north of Iceland.

My fourth scientific question was whether the emergence of the NIJ is associated with enhanced EKE attributed to the steeper northeastern part of the Icelandic slope. My simulations showed congruence between the steeper northeastern Iceland slope and increased EKE, consistent with observations. However, the simulations and analysis could not conclusively demonstrate that this is the mechanism responsible for the emergence of the NIJ. While this is to be expected, as plenty of other processes likely contribute to the emergence of the NIJ, the simulations indicate that this mechanism is worth exploring further.

5.4 Outlook

The idealized model employed in this study shows great potential for studying the NIJ and circulation north of Iceland. With improved treatment of in- and outflowing currents by the boundary, the presented and additional configurations of the in- and outflow through the western boundary can further elucidate how the flow north of Iceland responds to modifications at Danmark Strait. Additional configurations of the in- and outflow, such as a full-depth prescribed NIJ or a revised prescribed NIJ at mid-depth, or even moved closer to the slope, might reveal how sensitive the isopycnal structure north of Iceland, the interplay between the simulated NIJ and NIIC, upstream variabil-

ity, and the emergence of the NIJ is to the prescribed flow at the simulated Denmark Strait.

Moreover, additional modifications to the bathymetry, with a broader spectrum of steepness in the constant and varying slope configurations or more realistic along-slope changes, might also be advantageous to study the evolution and emergence of the NIJ. With the present model, a theoretical study or a sensitivity study on the instabilities caused by different levels of steepness might be conducive to a better understanding of the mechanisms needed for these instabilities to impact the deterioration of the NIIC and the emergence of the NIJ. Moreover, adding idealized components of the north Icelandic slope, such as a more gradual along-slope steepening, might be interesting in studying the evolution of the NIJ along a more realistic Icelandic slope.

Furthermore, the IdealTransects simulation showed promise in studying the aforementioned mechanisms in a more realistic configuration. The IdealTransect experiment could mainly be modified to retain AW near the slope, by a topographic or dynamical barrier, and to represent the along-slope changes in water masses in a more realistic way, by including a more drastic along-slope gradient in the initial fields or applying idealized atmospheric forcing. Such an adjusted configuration might be used specifically to study the impact of the density gradient between the NIJ and the NIIC on the stability of the currents, relative to the impact of the slope steepness. It could also shed light on the proposed impact of the along-slope evolution of the lateral density gradient between the NIIC and the domain, as this is one of the leading hypotheses for how the NIJ emerges. This could then be used to test the relative sensitivity of instabilities on the northeastern slope of Iceland between slope steepness (Isachsen et al., 2012), the thermal wind mechanism (Våge et al., 2011), and the density gradient between the NIJ and NIIC (Pickart et al., 2017).

It could also be interesting to expand the model to include the IFSJ through an idealized representation of the IFR and FBCO. This could be done in a similarly idealized configuration which would extend the domain eastward ($\sim$600 km) to also include the FBC in the east, with similarly prescribed outflows on this boundary, and in a similar way iteratively adding complexity. The hydrographic structure associated with the IFSJ is similar to the one associated with the NIJ and the one repeatedly simulated in this model. The model already simulated a current that could be reminiscent of the IFSJ in several simulations, which is intriguing. This could enhance the understanding of the interactions and similarities between the emergence of the two major pathways of Arctic-origin overflow water out of the Nordic Seas.

Bibliography

Amante, C. & Eakins, B. (2009). *ETOPO1 1 Arc-Minute Global Relief Model: Procedures, Data Sources and Analysis*. https://doi.org/doi:10.7289/V5C8276M

Behrens, E., Våge, K., Harden, B. E., Biastoch, A., & Böning, C. W. (2017). Composition and variability of the Denmark Strait Overflow Water in a high-resolution numerical model hindcast simulation. *Journal of Geophysical Research: Oceans*, 122(5423), 2647–2651. https://doi.org/10.1002/2016JC012158

Berntsen, J. & Thiem, O. (2007). Estimating the internal pressure gradient errors in a σ-coordinate ocean model for the Nordic Seas. *Ocean Dynamics*, 57(4-5), 417–429. https://doi.org/10.1007/s10236-007-0118-1

Beszczynska-Möller, A., Fahrbach, E., Schauer, U., & Hansen, E. (2012). Variability in Atlantic water temperature and transport at the entrance to the Arctic Ocean, 19972010. *ICES Journal of Marine Science*, 69(5), 852–863. https://doi.org/10.1093/icesjms/fss056

Blumsack, S. L. & Gierarsch, P. J. (1972). Mars: The Effects of Topography on Baroclinic Instability. *Journal of atmospheric sciences*, 29(6), 1081–1089. https://doi.org/https://doi.org/10.1175/1520-0469(1972)029<1081:MTEOTO>2.0.CO;2

Bracco, A., Pedlosky, J., & Pickart, R. S. (2008). Eddy formation near the west coast of Greenland. *Journal of Physical Oceanography*, 38(9), 1992–2002. https://doi.org/10.1175/2008JPO3669.1

Brakstad, A., Gebbie, G., Våge, K., Jeansson, E., & Ólafsdóttir, S. R. (2023a). Formation and pathways of dense water in the Nordic Seas based on a regional inversion. *Progress in Oceanography*, 212, 102981. https://doi.org/10.1016/j.pocean.2023.102981

Brakstad, A., Våge, K., Håvik, L., & Moore, G. W. K. (2019). Water Mass Transformation in the Greenland Sea during the Period 19862016. *Journal of Physical Oceanography*, 49(1), 121–140. https://doi.org/10.1175/JPO-D-17-0273.1

Brakstad, A., Våge, K., Ólafsdóttir, S. R., Jeansson, E., & Gebbie, G. (2023b). Hydrographic and geochemical observations in the Nordic Seas between 1950 and 2019. *NMDC*. https://doi.org/https://doi.org/10.21335/NMDC-1271328906

Buckley, M. W. & Marshall, J. (2016). Observations, inferences, and mechanisms of the Atlantic Meridional Overturning Circulation: A review. *Reviews of Geophysics*, 54(1), 5–63. https://doi.org/10.1002/2015RG000493

Casanova-Masjoan, M., Pérez-Hernández, M. D., Pickart, R. S., Valdimarsson, H., Ólafsdóttir, S. R., Macrander, A., Grisolía-Santos, D., Torres, D. J., Jónsson, S., Våge, K., Lin, P., & Hernández-Guerra, A. (2020). Along-Stream, Seasonal, and Interannual Variability of the North Icelandic Irminger Current and East Icelandic Current Around Iceland. *Journal of Geophysical Research: Oceans*, 125(9), e2020JC016283. https://doi.org/https://doi.org/10.1029/2020JC016283

Chafik, L., Hátún, H., Kjellsson, J., Larsen, K. M. H., Rossby, T., & Berx, B. (2020). Discovery of an unrecognized pathway carrying overflow waters toward the Faroe Bank Channel. *Nature Communications*, 11(1), 1–10. https://doi.org/10.1038/s41467-020-17426-8

Chafik, L., Nilsson, J., Rossby, T., & Kondetharayil Soman, A. (2023). The Faroe-Shetland Channel Jet: Structure, Variability, and Driving Mechanisms. *Journal of Geophysical Research: Oceans*, 128(4), e2022JC019083. https://doi.org/10.1029/2022JC019083

Chafik, L. & Rossby, T. (2019). Volume, Heat, and Freshwater Divergences in the Subpolar North Atlantic Suggest the Nordic Seas as Key to the State of the Meridional Overturning Circulation. *Geophysical Research Letters*, 46(9), 4799–4808. https://doi.org/10.1029/2019GL082110

Chassignet, E. P., Smith, L. T., Halliwell, G. R., & Bleck, R. (2003). North Atlantic Simulations with the Hybrid Coordinate Ocean Model (HYCOM): Impact of the Vertical Coordinate Choice, Reference Pressure, and Thermobaricity. *Journal of Physical Oceanography*, 33(12), 2504–2526. https://doi.org/https://doi.org/10.1175/1520-0485(2003)033<2504:NASWTH>2.0.CO;2

Cheng, W., Chiang, J. C., & Zhang, D. (2013). Atlantic Meridional Overturning Circulation (AMOC) in CMIP5 Models: RCP and Historical Simulations. *Journal of Climate*, 26(18), 7187–7197. https://doi.org/10.1175/JCLI-D-12-00496.1

Chung, T. (2010). *Computational Fluid Dynamics* (second ed.). Cambridge University Press. www.cambridge.org/9781107425255

Cooper, L. (1955). Deep water movements in the North Atlantic as a link between climatic changes around Iceland and biological productivity of the English Channel and Celtic Sea. *Journal of marine research*, 14, 347–362. https://images.peabody.yale.edu/publications/jmr/jmr14-04-10.pdf

Cushman-Roisin, B. & Beckers, J.-M. (2011). *Introduction to Geophysical Fluid Dynamics* (second ed.). Academic Press.

de Jong, M. F., Søiland, H., Bower, A. S., & Furey, H. H. (2018). The subsurface circulation of the Iceland Sea observed with RAFOS floats. *Deep-Sea Research Part*

I: Oceanographic Research Papers, 141(July), 1–10. https://doi.org/10.1016/j.dsr.2018.07.008

Dickson, R. R. & Brown, J. (1994). The production of North Atlantic Deep Water: Sources, rates, and pathways. *Journal of Geophysical Research: Oceans*, 99(C6), 12319–12341. https://doi.org/https://doi.org/10.1029/94JC00530

Drange, H., Dokken, T., Furevik, T., Gerdes, R., Berger, W., Nesje, A., Orvik, K. A., Skagseth, Ø., Skjelvan, I., & Østerhus, S. (2013). The Nordic Seas: An Overview. *The Nordic Seas: An Integrated Perspective: Oceanography, Climatology, Biogeochemistry, and Modeling*, 1–10. https://doi.org/10.1029/158GM02

Elvidge, A. D., Renfrew, I. A., Brooks, I. M., Srivastava, P., Yelland, M. J., & Prytherch, J. (2021). Surface Heat and Moisture Exchange in the Marginal Ice Zone: Observations and a New Parameterization Scheme for Weather and Climate Models. *Journal of Geophysical Research: Atmospheres*, 126(17), e2021JD034827. https://doi.org/10.1029/2021JD034827

Fahrbach, E., Rohardt, G., Shauer, U., Meincke, J., Osterhus, S., & Verduin, J. (2001). Direct measurements of heat and mass transport through Fram Strait. *Polar Research*, 20, 217–224. https://doi.org/https://doi.org/10.3402/polar.v20i2.6520

Fu, Y., Feili, L., Karstensen, J., & Wang, C. (2020). A stable Atlantic Meridional Overturning Circulation in a changing North Atlantic Ocean since the 1990s. *Science Advances*, 6(48), 7836–7863. https://doi.org/10.1126/SCIADV.ABC7836/SUPPL_FILE/ABC7836_SM.PDF

Girton, J. B., Pratt, L. J., Sutherland, D. A., & Price, J. F. (2006). Is the Faroe Bank Channel Overflow Hydraulically Controlled? *Journal of Physical Oceanography*, 36(12), 2340–2349. https://doi.org/10.1175/JPO2969.1

Gregory, J. M., Dixon, K. W., Stouffer, R. J., Weaver, A. J., Driesschaert, E., Eby, M., Fichefet, T., Hasumi, H., Hu, A., Jungclaus, J. H., Kamenkovich, I. V., Levermann, A., Montoya, M., Murakami, S., Nawrath, S., Oka, A., Sokolov, A. P., & Thorpe, R. B. (2005). A model intercomparison of changes in the Atlantic thermohaline circulation in response to increasing atmospheric CO2 concentration. *Geophysical Research Letters*, 32(12), 1–5. https://doi.org/10.1029/2005GL023209

Haidvogel, D. B. & Beckmann, A. (1999). *Numerical Ocean Circulation Modeling* (third ed.). Imperial College Press.

Harden, B. E. & Pickart, R. S. (2018). High-Frequency Variability in the North Icelandic Jet. *JOURNAL OF MARINE RESEARCH*, 76(2), 47–62. https://doi.org/10.1357/002224018824845910

Harden, B. E., Pickart, R. S., Valdimarsson, H., Våge, K., de Steur, L., Richards, C., Bahr, F., Torres, D., Børve, E., Jónsson, S., Macrander, A., Østerhus, S., Håvik, L., & Hattermann, T. (2016). Upstream sources of the Denmark Strait Overflow: Observations from a high-resolution mooring array. *Deep-Sea Research Part I:*

Oceanographic Research Papers, 112, 94–112. https://doi.org/10.1016/j.dsr.2016.02.007

Håvik, L., Almansi, M., Våge, K., & Haine, T. W. N. (2019). Atlantic-Origin Overflow Water in the East Greenland Current. *Journal of Physical Oceanography*, 49(9), 2255–2269. https://doi.org/https://doi.org/10.1175/JPO-D-18-0216.1

Huang, J., Pickart, R. S., Huang, R. X., Lin, P., Brakstad, A., & Xu, F. (2020). Sources and upstream pathways of the densest overflow water in the Nordic Seas. *Nature Communications*, 11(1), 1–9. https://doi.org/10.1038/s41467-020-19050-y

Huang, J., Pickart, R. S., Valdimarsson, H., Lin, P., Spall, M. A., & Xu, F. (2019). Structure and Variability of the North Icelandic Jet From Two Years of Mooring Data. *Journal of Geophysical Research: Oceans*, 124(6), 3987–4002. https://doi.org/10.1029/2019JC015134

Ingvaldsen, R., Loeng, H., & Asplin, L. (2002). Variability in the Atlantic inflow to the Barents Sea based on a one-year time series from moored current meters. *Continental Shelf Research*, 22(3), 505–519. https://doi.org/https://doi.org/10.1016/S0278-4343(01)00070-X

Isachsen, P. E., Koszalka, I., & Lacasce, J. H. (2012). Observed and modeled surface eddy heat fluxes in the eastern Nordic Seas. *Journal of Geophysical Research: Oceans*, 117(8), 1–10. https://doi.org/10.1029/2012JC007935

Jónsson, S. (1999). The circulation in the northern part of the Denmark Strait and its variability. Technical report, CM.

Jónsson, S. & Valdimarsson, H. (2012). Hydrography and circulation over the southern part of the Kolbeinsey Ridge. *ICES Journal of Marine Science*, 69(7), 1255–1262. https://doi.org/10.1093/ICESJMS/FSS101

Jónsson, S. & Valdimarsson, H. (2004). A new path for the Denmark Strait overflow water from the Iceland Sea to Denmark Strait. *Geophysical Research Letters*, 31(3), 2–5. https://doi.org/10.1029/2003GL019214

Kawasaki, T. & Hasumi, H. (2016). The inflow of Atlantic water at the Fram Strait and its interannual variability. *Journal of Geophysical Research: Oceans*, 121(1), 502–519. https://doi.org/10.1002/2015JC011375

Kuhlbrodt, T., Griesel, A., Montoya, M., Levermann, A., Hofmann, M., & Rahmstorf, S. (2007). On the driving processes of the Atlantic meridional overturning circulation. *Reviews of Geophysics*, 45(2). https://doi.org/10.1029/2004RG000166

Lin, P., Pickart, R. S., Jochumsen, K., Moore, G. W., Valdimarsson, H., Fristedt, T., & Pratt, L. J. (2020). Kinematic Structure and Dynamics of the Denmark Strait Overflow from Ship-Based Observations. *Journal of Physical Oceanography*, 50(11), 3235–3251. https://doi.org/10.1175/JPO-D-20-0095.1

Livingston, H. D., Swift, J. H., & Ostlund, H. G. (1985). Artificial radionuclide tracer supply to the Denmark Strait overflow between 1972 and 1981. *Journal of Geophysical Research*, 90(C4), 6971–6982. https://doi.org/10.1029/jc090ic04p06971

Macrander, A., Valdimarsson, H., & Jõnsson, S. (2014). Improved transport estimate of the East Icelandic Current 2002-2012. *Journal of Geophysical Research: Oceans*, 119(6), 3407–3424. https://doi.org/10.1002/2013JC009517

Marchesiello, P., McWilliams, J. C., & Shchepetkin, A. (2001). Open boundary conditions for long-term integration of regional oceanic models. *Ocean Modelling*, 3(1), 1–20. https://doi.org/https://doi.org/10.1016/S1463-5003(00)00013-5

Marshall, J. & Speer, K. (2012). Closure of the meridional overturning circulation through Southern Ocean upwelling. *Nature Geoscience 2012 5:3*, 5(3), 171–180. https://doi.org/10.1038/ngeo1391

Mastropole, D., Pickart, R. S., Valdimarsson, H., Våge, K., Jochumsen, K., & Girton, J. (2016). On the hydrography of Denmark Strait. *Journal of Geophysical Research: Oceans*, 122(1), 306–321. https://doi.org/10.1002/2016JC012007

Mauritzen, C. (1996). Production of dense overflow waters feeding the North Atlantic across the Greenland-Scotland Ridge. Part 1: Evidence for a revised circulation scheme. *Deep-Sea Research Part I: Oceanographic Research Papers*, 43(6), 769–806. https://doi.org/10.1016/0967-0637(96)00037-4

Mechoso, C. R. (1980). Baroclinic Instability of Flows Along Sloping Boundaries. *Journal of atmospheric sciences*, 37(6), 1393–1399. https://doi.org/https://doi.org/10.1175/1520-0469(1980)037<1393:BIOFAS>2.0.CO;2

Moore, G. W., Vage, K., Pickart, R. S., & Renfrew, I. A. (2015). Decreasing intensity of open-ocean convection in the Greenland and Iceland seas. *Nature Climate Change*, 5(9), 877–882. https://doi.org/10.1038/NCLIMATE2688

Munk, W. & Wunsch, C. (1998). Abyssal recipes II: energetics of tidal and wind mixing. *Deep Sea Research Part I: Oceanographic Research Papers*, 45(12), 1977–2010. https://doi.org/10.1016/S0967-0637(98)00070-3

Neill, S. P. & Hashemi, M. R. (2018). Ocean Modelling for Resource Characterization. *Fundamentals of Ocean Renewable Energy*, 193–235. Academic Press. https://doi.org/10.1016/B978-0-12-810448-4.00008-2

Nikolopoulos, A., Borenäs, K., Hietala, R., & Lundberg, P. (2003). Hydraulic estimates of Denmark strait overflow. *Journal of Geophysical Research: Oceans*, 108(3). https://doi.org/10.1029/2001JC001283

Østerhus, S., Woodgate, R., Valdimarsson, H., Turrell, B., de Steur, L., Quadfasel, D., Olsen, S. M., Moritz, M., Lee, C. M., Larsen, K. M. H., Jónsson, S., Johnson, C., Jochumsen, K., Hansen, B., Curry, B., Cunningham, S., & Berx, B. (2019). Arctic Mediterranean exchanges: a consistent volume budget and trends in transports from

two decades of observations. *Ocean Science*, 15(2), 379–399. https://doi.org/10.5194/os-15-379-2019

Pickart, R. S., Spall, M. A., Torres, D. J., Våge, K., Valdimarsson, H., Nobre, C., Moore, G. W., Jonsson, S., & Mastropole, D. (2017). The north icelandic jet and its relationship to the north icelandic irminger current. *Journal of Marine Research*, 75(5), 605–639. https://doi.org/10.1357/002224017822109505

Pratt, L. J. (2004). Recent progress on understanding the effects of rotation in models of sea straits. *Deep Sea Research Part II: Topical Studies in Oceanography*, 51(4-5), 351–369. https://doi.org/10.1016/J.DSR2.2003.06.005

Qu, L. & Hetland, R. (2020). Nongeostrophic baroclinic instability over sloping bathymetry: Buoyant flow regime. *Journal of Physical Oceanography*, 50(7), 1937–1956. https://doi.org/10.1175/JPO-D-19-0145.1

Rosenblum, E. & Eisenman, I. (2017). Sea Ice Trends in Climate Models Only Accurate in Runs with Biased Global Warming. *Journal of Climate*, 30(16), 6265–6278. https://doi.org/10.1175/JCLI-D-16-0455.1

Rudels, B., Fahrbach, E., Meincke, J., Budéus, G., & Eriksson, P. (2002). The East Greenland Current and its contribution to the Denmark Strait overflow. *ICES Journal of Marine Science*, 59(6), 1133–1154. https://doi.org/10.1006/jmsc.2002.1284

Semper, S. (2020). *Circulation along the northern slope of the Greenland-Scotland Ridge (PhD Thesis, University of Bergen)*. University of Bergen. https://bora.uib.no/bora-xmlui/handle/11250/2712005

Semper, S., Pickart, R. S., Våge, K., Larsen, K. M. H., Hátún, H., & Hansen, B. (2020). The Iceland-Faroe Slope Jet: a conduit for dense water toward the Faroe Bank Channel overflow. *Nature Communications*, 11(1), 1–10. https://doi.org/10.1038/s41467-020-19049-5

Semper, S., Våge, K., Pickart, R. S., Jónsson, S., & Valdimarsson, H. (2022). Evolution and Transformation of the North Icelandic Irminger Current Along the North Iceland Shelf. *Journal of Geophysical Research: Oceans*, 127(3), 1–23. https://doi.org/10.1029/2021JC017700

Semper, S., Våge, K., Pickart, R. S., Valdimarsson, H., Torres, D. J., & Jónsson, S. (2019a). The emergence of the north icelandic jet and its evolution from northeast Iceland to Denmark strait. *Journal of Physical Oceanography*, 49(10), 2499–2521. https://doi.org/10.1175/JPO-D-19-0088.1

Semper, S., Våge, K., Pickart, R. S., Valdimarsson, H., Torres, D. J., Jõnsson, S., Søiland, H., & Danielsen, M. (2019b). Temperature, salinity and velocities on seven transects along the continental slope north of Iceland. *PANGEA*. https://doi.org/https://doi.org/10.1594/PANGAEA.903535

Shchepetkin, A. F. & McWilliams, J. C. (2003). A method for computing horizontal pressure-gradient force in an oceanic model with a nonaligned vertical coordinate. *Journal of Geophysical Research: Oceans*, 108(C3), 3090. https://doi.org/10.1029/2001JC001047

Shchepetkin, A. F. & McWilliams, J. C. (2005). The regional oceanic modeling system (ROMS): a split-explicit, free-surface, topography-following-coordinate oceanic model. *Ocean Modelling*, 9(4), 347–404. https://doi.org/10.1016/J.OCEMOD.2004.08.002

Shchepetkin, A. F. & McWilliams, J. C. (2009). Computational Kernel Algorithms for Fine-Scale, Multiprocess, Longtime Oceanic Simulations. *Computational Methods for the Atmosphere and the Oceans*, 14(08), 121–183. https://doi.org/10.1016/S1570-8659(08)01202-0

Song, Y. & Haidvogel, D. (1994). A Semi-implicit Ocean Circulation Model Using a Generalized Topography-Following Coordinate System. *Journal of Computational Physics*, 115(1), 228–244. https://doi.org/10.1006/JCPH.1994.1189

Spall, M. A. (2004). Boundary currents and watermass transformation in marginal seas. *Journal of Physical Oceanography*, 34(5), 1197–1213. https://doi.org/10.1175/1520-0485(2004)034<1197:BCAWTI>2.0.CO;2

Spall, M. A. (2011). On the role of eddies and surface forcing in the heat transport and overturning circulation in marginal seas. *Journal of Climate*, 24(18), 4844–4858. https://doi.org/10.1175/2011JCLI4130.1

Swift, J. H. & Aagaard, K. (1981). Seasonal transitions and water mass formation in the Iceland and Greenland seas. *Journal of Deep-Sea Research*, 28(10), 1107–1129.

Swift, J. H., Aagaard, K., & Malmberg, S. A. (1980). The contribution of the Denmark strait overflow to the deep North Atlantic. *Deep Sea Research Part A, Oceanographic Research Papers*, 27(1), 29–42. https://doi.org/10.1016/0198-0149(80)90070-9

Swift, J. H. & Smethie, W. M. J. (1989). The Tritium'Krypton-85 Age of Denmark Strait Overflow Water and Gibbs Fracture Zone Water Just South of Denmark Strait. *Journal of Geophysical Research*, 94(C6), 8265–8275.

Turrell, W. R., Slesser, G., Adams, R. D., Payne, R., & Gillibrand, P. A. (1999). Decadal variability in the composition of Faroe Shetland Channel bottom water. *Deep-Sea Research Part I: Oceanographic Research Papers*, 46(1), 1–25. https://doi.org/10.1016/S0967-0637(98)00067-3

Våge, K., Papritz, L., Håvik, L., Spall, M. A., & Moore, G. W. (2018). Ocean convection linked to the recent ice edge retreat along east Greenland. *Nature Communications*, 9(1). https://doi.org/10.1038/s41467-018-03468-6

Våge, K., Pickart, R. S., Spall, M. A., Moore, G. W., Valdimarsson, H., Torres, D. J., Erofeeva, S. Y., & Nilsen, J. E. Ø. (2013). Revised circulation scheme north of the

Denmark Strait. *Deep-Sea Research Part I: Oceanographic Research Papers*, 79, 20–39. https://doi.org/10.1016/j.dsr.2013.05.007

Våge, K., Pickart, R. S., Spall, M. A., Valdimarsson, H., Jónsson, S., Torres, D. J., Østerhus, S., & Eldevik, T. (2011). Significant role of the North Icelandic Jet in the formation of Denmark Strait overflow water. *Nature Geoscience*, 4(10), 723–727. https://doi.org/10.1038/ngeo1234

Våge, K., Semper, S., Valdimarsson, H., Jónsson, S., Pickart, R. S., & Moore, G. W. (2022). Water mass transformation in the Iceland Sea: Contrasting two winters separated by four decades. *Deep-Sea Research Part I: Oceanographic Research Papers*, 186(August 2021), 103824. https://doi.org/10.1016/j.dsr.2022.103824

wiki ROMS (2016). *Numerical Solution Technique*. https://www.myroms.org/wiki/Numerical_Solution_Technique

wiki ROMS (2019). *Boundary Conditions*. https://www.myroms.org/wiki/Boundary_Conditions

Winton, M., Hallberg, R., & Gnanadesikan, A. (1998). Simulation of Density-Driven Frictional Downslope Flow in Z-Coordinate Ocean Models. *Journal of Physical Oceanography*, 28(11), 2163–2174. https://doi.org/10.1175/1520-0485(1998)028

Yang, J. & Pratt, L. J. (2014). Some dynamical constraints on upstream pathways of the denmark strait overflow. *Journal of Physical Oceanography*, 44(12), 3033–3053. https://doi.org/10.1175/JPO-D-13-0227.1

Ypma, S. L., Brüggemann, N., Georgiou, S., Spence, P., Dijkstra, H. A., Pietrzak, J. D., & Katsman, C. A. (2019). Pathways and watermass transformation of Atlantic Water entering the Nordic Seas through Denmark Strait in two high resolution ocean models. *Deep-Sea Research Part I: Oceanographic Research Papers*, 145(February), 59–72. https://doi.org/10.1016/j.dsr.2019.02.002

Årthun, M., Asbjørnsen, H., Chafik, L., Johnson, H. L., & Våge, K. (2023). Future strengthening of the Nordic Seas overturning circulation. *Nature Communications 2023 14:1*, 14(1), 1–12. https://doi.org/10.1038/s41467-023-37846-6

Appendix A

Derivation of the Thermal Wind Balance

Starting with the Boussinesq, hydrostatic primitive momentum equations for a frictionless, stratified, rotating fluid (Cushman-Roisin & Beckers, 2011),

$$\frac{\partial u}{\partial t} + u\frac{\partial u}{\partial x} + v\frac{\partial u}{\partial y} + w\frac{\partial u}{\partial z} - fv = -\frac{1}{\rho_0}\frac{\partial P}{\partial x} \tag{A.1}$$

$$\frac{\partial v}{\partial t} + u\frac{\partial v}{\partial x} + v\frac{\partial v}{\partial y} + w\frac{\partial v}{\partial z} + fu = -\frac{1}{\rho_0}\frac{\partial P}{\partial y} \tag{A.2}$$

$$\rho g = -\frac{\partial P}{\partial z} \tag{A.3}$$

where u, v, and w are the zonal, meridional, and vertical velocity components, f is the Coriolis parameter ($f = 2\Omega sin\phi$), ρ_0 is the reference density, ρ is the density (retained due to the association to gravity), P is pressure and g is the gravitational constant. If we additionally assume the flow to be steady and linearize we arrive at the geostrophic equations:

$$fv_g = \frac{1}{\rho_0}\frac{\partial P}{\partial x} \tag{A.4}$$

$$fu_g = -\frac{1}{\rho_0}\frac{\partial P}{\partial y} \tag{A.5}$$

$$\rho g = -\frac{\partial P}{\partial z} \tag{A.6}$$

where the subscript u_g/v_g indicates that the flow is in geostrophic balance. Then taking the vertical derivative of Equations A.1 and A.2 and substitute the pressure term for Equation A.3,

$$f\frac{\partial v_g}{\partial z} = \frac{1}{\rho_0}\frac{\partial}{\partial x}\left(\frac{\partial P}{\partial z}\right) \rightarrow \frac{\partial v_g}{\partial z} = -\frac{g}{f\rho_0}\frac{\partial\rho}{\partial x} \tag{A.7}$$

$$f\frac{\partial u_g}{\partial z} = -\frac{1}{\rho_0}\frac{\partial}{\partial y}\left(\frac{\partial P}{\partial z}\right) \rightarrow \frac{\partial u_g}{\partial z} = \frac{g}{f\rho_0}\frac{\partial\rho}{\partial y} \tag{A.8}$$

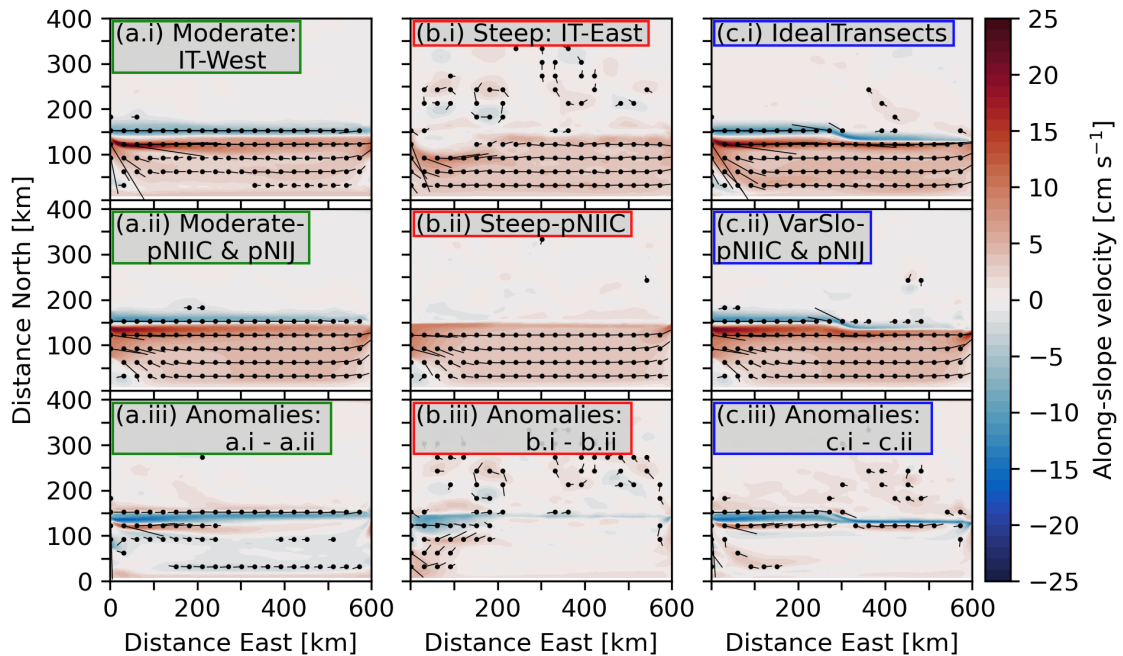# Appendix B

IdealTransect simulations

Figure B.1: Depth-integrated zonal velocity (shading) and depth-integrated horizontal velocities (arrows) averaged over the last six months of the simulations for the IT-West (a.i), IT-East (b.i), and IdealTransects (c.i), the Moderate-pNIIC&pNIJ (a.ii), Steep-pNIIC (b.ii), and VarSlo-pNIIC&pNIJ (c.ii) simulations, and the anomalies between the corresponding simulations, IT-West − Moderate-pNIIC&pNIJ (a.iii), IT-East − Steep-pNIIC (b.iii), and IdealTransects − VarSlo-pNIIC&pNIJ (c.iii). Arrows indicating depth-integrated velocities below 1.5 cm s^{-1} are not shown.